MOUNTAIN-PLAINS CONSORTIUM

MPC 17-320 | C.P. Pantelides, M.J. Ameli and L.D. Reaveley

Evaluation of Grouted Splice Sleeve Connections for Precast Reinforced Concrete Bridge Piers

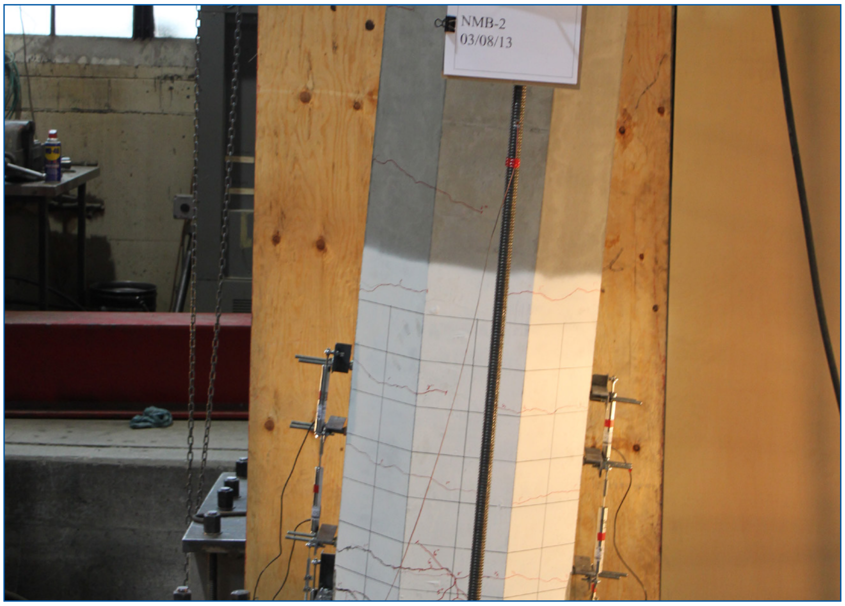

A University Transportation Center sponsored by the U.S. Department of Transportation serving the Mountain-Plains Region. Consortium members:

Colorado State University
North Dakota State University
South Dakota State University
University of Colorado Denver
University of Denver
University of Utah
Utah State University
University of Wyoming

Evaluation of Grouted Splice Sleeve Connections for Precast Reinforced Concrete Bridge Piers

Chris P. Pantelides
Professor
Department of Civil and Environmental Engineering
University of Utah
Salt Lake City, Utah, 84112
Phone: (801) 585-3991
Email: c.pantelides@utah.edu

M.J. Ameli
Graduate Student
Department of Civil and Environmental Engineering
University of Utah
Salt Lake City, Utah, 84112
Phone: (801) 585-3991
Email: m.ameli@utah.edu

Lawrence D. Reaveley
Professor
Department of Civil and Environmental Engineering
University of Utah
Salt Lake City, Utah, 84112
Phone: (801) 581-6118
Email: reaveley@civil.utah.edu

April 2017

Acknowlegments

The authors acknowledge the financial support provided by the Mountain Plain Consortium (MPC) through project MPC-392, the Utah Department of Transportation, the New York State Department of Transportation and the Texas Department of Transportation through the Pooled Fund Study Program.

The authors acknowledge Carmen Swanwick and Joshua Sletten, who served on UDOT's Technical Advisory Committee for helping to guide the research. In addition, they appreciate the advice of Harry White, New York State Department of Transportation.

The authors would also like to acknowledge the assistance of Dylan Brown and Joel Parks, MSc students at the University of Utah. Furthermore, they acknowledge the assistance of Mark Bryant, Zant Doty, Trevor Nye, and Wade Stinson of the University of Utah for their assistance in the experiments.

The following companies made in-kind donations for this project and the authors are grateful to them: Splice Sleeve North America, Inc., ERICO, and Hanson Structural Precast.

Disclaimer

ABSTRACT

Connections between precast concrete elements must be able to withstand significant stresses and deformations in earthquakes. The grouted splice sleeve (GSS) connector is being considered for connecting footing, column, and cap beam elements in accelerated bridge construction (ABC). There are limited data for use of this connector in bridges located in moderate-to-high seismic regions. This report describes a research program conducted to evaluate bridge joints using two types of GSS connectors experimentally. Cyclic quasi-static loading was used to test column-to-footing and column-to-cap beam half-scale specimens. One control specimen and two precast specimens were constructed for each category for a total of six specimens. The precast column-to-footing joint incorporated one type of GSS connector for which the bars were grouted at both ends (GGSS); the precast column-to-cap beam joint used a different GSS connector type for which one bar was threaded into one end and the other bar was grouted into the opposite end (FGSS). Experimental results showed that the performance of all test specimens was satisfactory compared to current codes. Compared to control specimens, a reduced displacement ductility capacity was obtained for the precast specimens in both categories.

TABLE OF CONTENTS

LIST OF TABLES

LIST OF FIGURES

LIST OF ACRONYMS

AASHTO	American Association of State Highway and Transportation Officials
ACI	American Concrete Institute
GSS	Grouted Splice Sleeve
LVDT	Linear Variable Differential Transformer
MPC	Mountain-Plains Consortium
PBES	Prefabricated Bridge Elements and Systems
SDC	Seismic Design Category
SDC	Seismic Design Criteria
UDOT	Utah Department of Transportation

EXECUTIVE SUMMARY

In recent years, accelerated bridge construction (ABC) has gained attention within regions of moderate-to-high seismicity. Prefabrication of bridge structural components is a highly effective method in this process and is one of the ABC methods under the category of Prefabricated Bridge Elements and Systems (PBES) promoted by the Federal Highway Administration. Connections between such precast components play an important role in the overall seismic performance of bridges. This report describes a research study developed to investigate a potential ABC connector type for joints of bridges located in high-seismic regions. This connector, referred to as a grouted splice sleeve (GSS), is studied for column-to-footing and column-to-cap beam joints. Half-scale test models were designed and constructed based on typical reinforced concrete bridges built in the state of Utah. Cyclic quasi-static loading was applied to three column-to-footing and three column-to-cap beam half-scale specimens. The precast column-to-footing joints incorporated one type of GSS connector where the bars were grouted at both ends (GGSS); the precast column-to-cap beam joints used a different GSS connector where one bar was threaded into one end and the other bar was grouted into the opposite end (FGSS). The GSS connectors were placed in the column base for the first test alternative in both categories; whereas, they were located in the footing or cap beam for the second test alternative. A cast-in-place specimen was tested for each category to provide a control test for comparative studies. Experimental results showed that the performance of the precast specimens was satisfactory. The report compares the performance of the precast to monolithic joints for both the GGSS and FGSS categories. The presence of the GSS connectors in the column base of the precast test models caused a disruption in the natural stress transfer between the connecting components; hence, a different cyclic performance was observed compared with the control tests. A slight improvement was observed when the GSS connectors were incorporated outside the column base. A reduced displacement ductility capacity was achieved for the precast specimens compared with the cast-in-place ones.

1. INTRODUCTION

Accelerated bridge construction (ABC) refers to a bridge construction method that incorporates innovative techniques, methodologies, and materials to efficiently reduce construction time and traffic disruption. It also provides a higher level of work-zone safety for workers and commuters and improves environmental-friendly activities. Prefabrication of bridge structural components is a highly effective method in this process and is one of the ABC methods under the category of Prefabricated Bridge Elements and Systems (PBES) promoted by the Federal Highway Administration.

Many bridges have been built or rehabilitated following ABC standards. Local examples in the state of Utah include the I-15 CORE Provo Center Street Interchange, the Riverdale Road over I-84 Bridge, and the I-15 South Layton Interchange. Precast concrete deck panels, substructures, and superstructures have been frequently utilized as effective ABC methods. The connections or joints between such precast elements are among the most critical components in the whole structure. Researchers are in the process of investigating the suitability of various connection configurations, especially in moderate-to-high seismic regions. These connections not only have to conform to ABC standards in terms of the overall construction delivery time, but must also resist moderate to high levels of earthquake-induced deformations and stresses. Lateral load capacity, ductility level, and reparability are three significant acceptance criteria for any connection method considered in earthquake-prone regions.

The *grouted duct connection* has been introduced as a viable ABC technique for both column-to-footing and column-to-cap beam joints [1, 2]. In this method, corrugated steel ducts are accommodated in a footing or cap beam, and column reinforcement dowels are inserted and grouted inside the ducts.

The *pocket connection* was studied and implemented to connect bridge columns to cap beams [3]. It is constructed by placing a circular corrugated steel duct inside the cap beam. Projected column bars are inserted into the pocket that is filled with concrete at the end.

The *socket connection* is another type of ABC connection that has recently become more popular. A socket foundation was studied at the University of Washington and later used to connect columns to spread footings in a bridge constructed in the state of Washington over I-5 [4]. In this method, the bottom end of the precast column is roughened and embedded in the footing, which is commonly cast-in-place. The gap is then filled with grout or concrete.

Prestressing has been incorporated in many bridge columns to improve their seismic performance by providing self-centering characteristics. This connection type is identified as a *hybrid connection* because both prestressing and mild steel are utilized. Research studies show that residual displacements and overall damage are reduced compared with non-prestressed connections [5].

Innovative techniques have been studied in order to achieve superior performance during a seismic event. One of the most recent studies investigated the application of *shape memory alloys* (SMA) for connecting bridge sub-assemblies [6]. Headed SMA bars were used in a bridge column-to-footing joint together with a grouted duct connection that was incorporated in the footing to facilitate the application of such a system in ABC.

The *grouted splice sleeve connector* and other types of rebar splicing devices are considered as another effective connection type for ABC. Such connectors have been frequently used, specifically in non-seismic regions, because they offer ease of construction and speed up construction time. In this joint type, each individual rebar is spliced by means of a mechanical coupler, which is readily located within one of the components, normally the precast component built at the precast plant. The response of joints utilizing such connectors to a seismic event was recently studied to investigate their performance in high seismic areas [7]. Among all ABC connection methods, grouted splice sleeve connectors require more profound investigation and research as there have been very few comprehensive experimental or analytical studies in the United States, especially with detailing typical of bridge structural elements. There is a need for more technical documentation on the performance of grouted splice sleeve connectors before they can be used in joints of bridges located in moderate-to-high seismic regions.

1.1 Previous Research

An evaluation of several ABC connections in moderate-to-high seismic regions was conducted and summarized in NCHRP Report 698 [3]. Verified connection types include bar couplers, grouted ducts, pocket connections, socket connections, hybrid connections, integral connections, and emerging technologies, such as shape memory alloys and elastomeric bearings. These connections were either utilized in actual practice, or were being developed in research studies. The aforementioned ABC connections were then ranked according to technology readiness, performance, and time savings potential, relative to cast-in-place construction for the same connection type. One of the significant outcomes of this synthesis study was the prioritization of more research studies essential for each connection type in order to fully understand their behavior under seismic actions.

A bar coupler was defined as a mechanical coupler used to splice two bars together. This synthesis report addressed several types of couplers, such as threaded sleeves, headed bars with separate sleeves, external clamping screws, and grouted sleeves. Application of the grouted sleeve, which is typically used in bridges, provides the benefit of larger tolerances in comparison with other types of couplers, as shown in Figure 1.1 [3].

Despite extensive use of such connectors in regions of moderate seismicity, in-depth knowledge of their inelastic behavior has not been achieved, necessitating more research and experimental verification. The need for further studies discussed in NCHRP Report 698 was based on the urgency level of the unknown aspects of this connector. First priority was given to the cyclic performance of the couplers with the bars in their plastic range of stress, and strain distribution for the bars being spliced; second priority studies included the investigation of the strength details, such as magnitude of stress that each bar can develop, together with verification of bar coupler placement. The latter refers to the proper location of the coupler (e.g., in the column or footing), so it does not affect the overall response to earthquake loads, but could still be a constructible detail. The effect of surrounding concrete and level of provided confinement on the coupler is the third category of priorities, as the last necessary study to be conducted on this type of ABC connector.

As part of a comprehensive research study on the seismic performance of next generation bridge components for ABC, the University of Nevada, Reno, has been investigating the behavior of four column-to-footing connections under cyclic lateral loading, utilizing two different proprietary couplers [7]. The research program also considered a cast-in-place specimen as the control test. HRC 500 Up-Set Headed Couplers (HC) and NMB Splice Sleeves (GC) were used to connect the longitudinal bars in the column and footing, as shown in Figure 1.2. For each coupler, two test specimens were constructed and tested under cyclic quasi-static loading. A precast pedestal was incorporated in one specimen for each category to reduce the moment demand over the coupler region. Considering the hysteretic behavior of all specimens, it was noted that the connection with HC couplers showed a similar response to the cast-in-place detail and withstood a relatively large amount of drift. In spite of the ease of construction achieved by incorporating the grouted couplers, their ductility capacity was found to be less than both the cast-in-place and the HC connection specimens. Comparing the results of the cyclic tests, it was noted that all specimens exhibited similar performance in terms of ultimate load capacity and energy dissipation, but the ductility capacity was different.

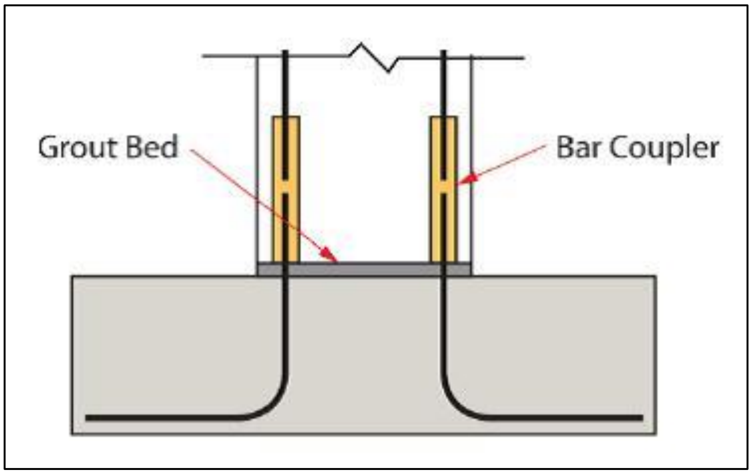

Figure 1.1 Typical application of a bar coupler [3].

Haber et al. (2013) described a series of air tests on the two aforementioned splicing systems [8]. These tests were conducted to obtain results necessary for numerical modeling focusing on the coupler region. To study the stress-strain behavior of that region, strain gauges were used on the spliced bars, mid-section of the coupler, and within the coupler (on the rebar inside the coupler). Results from these tests showed that the imposed displacement rate made a slight difference in the overall performance of the systems. Results also showed that the bar fractured away from the coupler region.

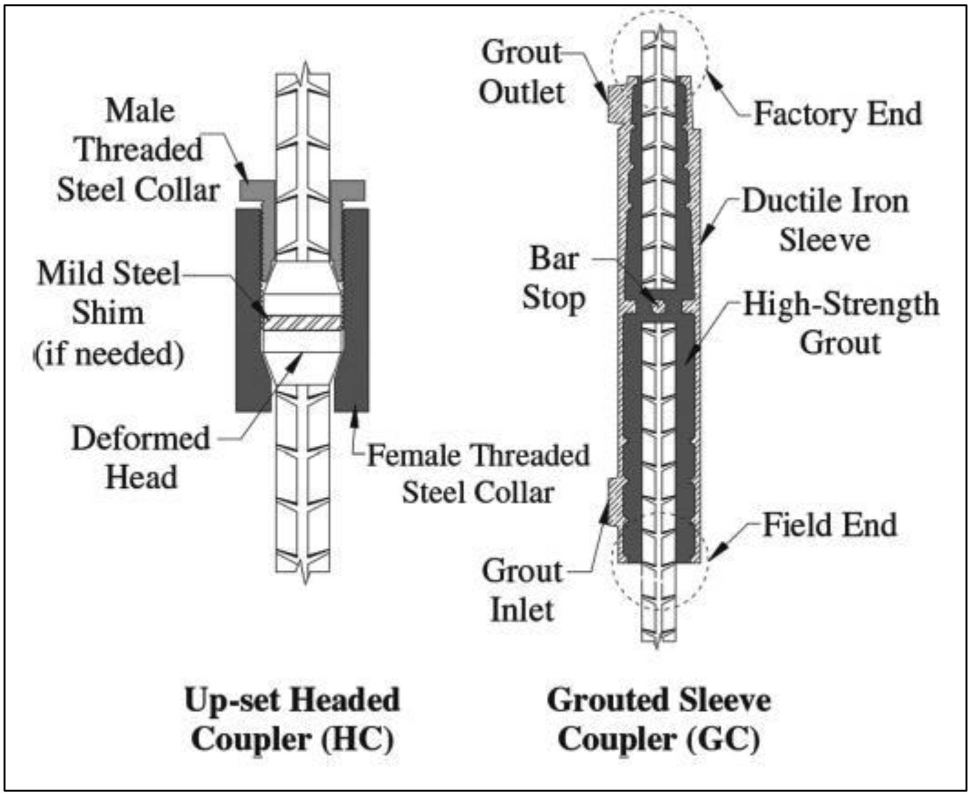

Figure 1.2 Two types of coupler used in previous research [7].

An experimental study was carried out on grout-filled sleeves in air, as opposed to a grout-filled sleeve inside a concrete member [9]. One such study is a comprehensive investigation of two commercially available grout-filled sleeves (NMB Splice Sleeve and Lenton Interlok) under slip, fatigue, ultimate load, and creep. As a result of this study, both sleeves were approved for bridge applications in the state of Michigan, as they met the requirements set by the AASHTO LRFD Bridge Design Specifications [10]. Also, results showed that they both conformed to Type 2 connection requirements of the ACI-550 Code, enabling their application even in the plastic hinge regions of building elements in Michigan [11].

Aida et al. (2005) reported on experimental testing of three ¾-scale specimens in Japan, two of which used NMB Splice Sleeves to connect columns to footings [12]. The specimens, representing railroad bridge column to footing joints, were heavily reinforced and tested under cyclic load to investigate their inelastic performance. Specimens with NMB Splice Sleeves showed acceptable inelastic behavior under cyclic loads compared with cast-in-place specimens. The maximum load resisted by the two specimens with the NMB Splice Sleeves was 7% to 11% greater than that for the cast-in-place specimen.

Yoshino et al. (1996) proposed an innovative shear reinforcing configuration called the Intensive Shear Reinforcing (ISR) method, for precast concrete elements connected by means of NMB Splice Sleeves [13]. Transverse reinforcement in this configuration was concentrated at both ends of the sleeves, compared with the conventional method in which hoops are placed at a particular spacing everywhere along the member. The ISR method offers the advantage of better constructability, as shown in Figure 1.3. According to results from the experiments, including monotonic and cyclic loading of both systems, the ISR method is comparable with the conventional detail. A strut-and-tie model was also developed in the analytical phase of the study, depicting the load transfer in the sleeve zone. This patented technique is used for building construction in Japan.

The Splice Sleeve Company carried out cyclic tests on building column specimens that incorporated NMB Splice Sleeves to connect the longitudinal column bars [14]. Different levels of axial load, shear reinforcement, existence of shear keys, and ultimately the location of Splice Sleeves were considered as test variables and investigated in this experimental study that included a total of nine test specimens. A comparison between the results of the monolithic specimen with the specimens incorporating NMB Splice Sleeves indicated acceptable performance of the splice sleeves in terms of both strength and ductility. However, it was observed that both the test setup and test specimens were not typical of bridges.

Matsuzaki et al. (1987) conducted research studies on individual NMB Splice Sleeves as well as test specimens connected by means of such devices [15]. The results of monotonic and cyclic tests on various sleeve sizes connecting different size steel bars were presented. A significant contribution of this investigation was the characterization of slip and pull-out properties of the system, in addition to illustration of the stress transfer between bars and the cast iron sleeve. The results of this study were then utilized in an analytical effort to replicate the response of precast components connected by means of such devices under reversed cyclic loads. Figure 1.4 shows the results of the aforementioned tests for a spliced sleeve connection (NO2) compared with a specimen with typical connection details (NO1).

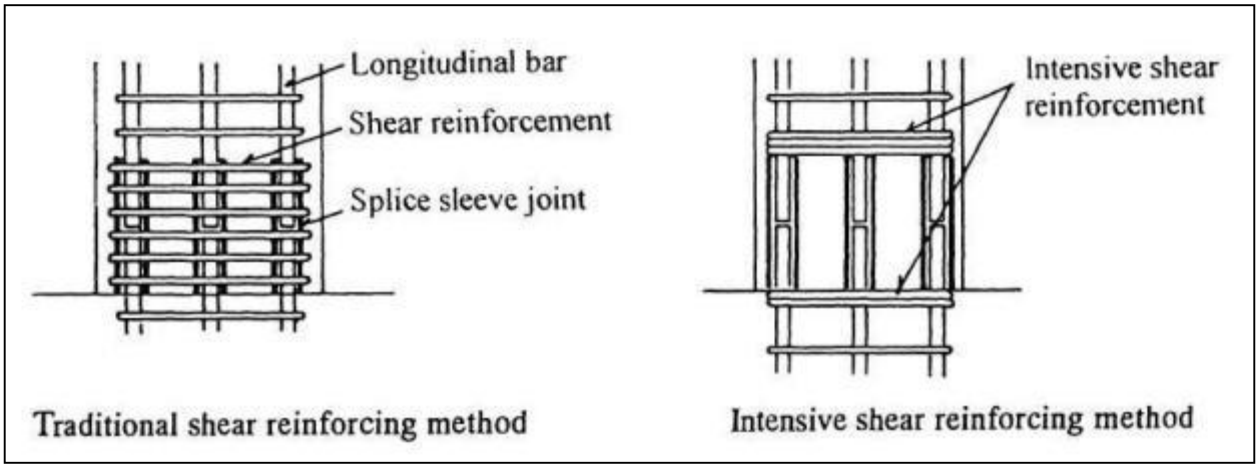

Figure 1.3 ISR method for precast reinforced concrete members [13].

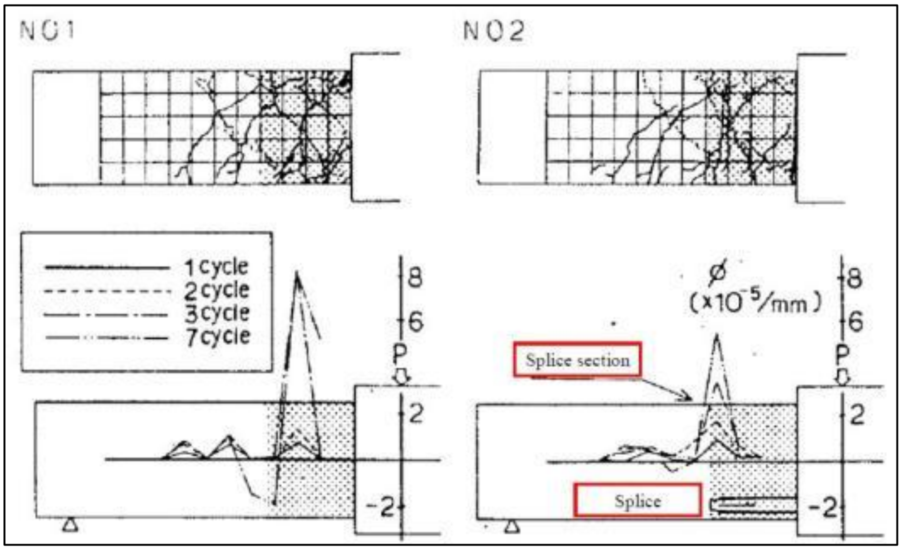

Figure 1.4 Damage state for two test specimens at failure [15].

The overall performance of all test specimens implies a similar response under the applied loading protocol in terms of strength and displacement capacity; however, these results may not apply to precast reinforced concrete bridge columns, as there was no axial load exerted on these specimens.

1.2 Research Objectives

This report describes a research program conducted to evaluate bridge joint subassemblies utilizing grouted splice sleeve (GSS) connectors.

GSS connectors, alternatively called mechanical rebar splices or grout-filled steel sleeves, are hollow steel cylinders made of ductile iron. Figure 1.5 shows the two types of GSS connectors utilized in this research project. Steel bars from two reinforced concrete components that are to be connected to each other are grouted at both sleeve ends for the longer GSS, or threaded into one end and grouted at the opposite end in the other type, as shown in Figure 1.6.

The shorter GSS is referred to as FGSS, in which the threaded factory dowel is fastened to one end while the field dowel is grouted inside the other end of the sleeve. This GSS is a product of Erico®, commercially available under the name Lenton® Interlok.

The longer alternative is referred to as GGSS, indicating that rebar is grouted at both ends of the sleeve. This GSS is a product of Splice Sleeve North America and commercially available under the name NMB Splice-Sleeve®.

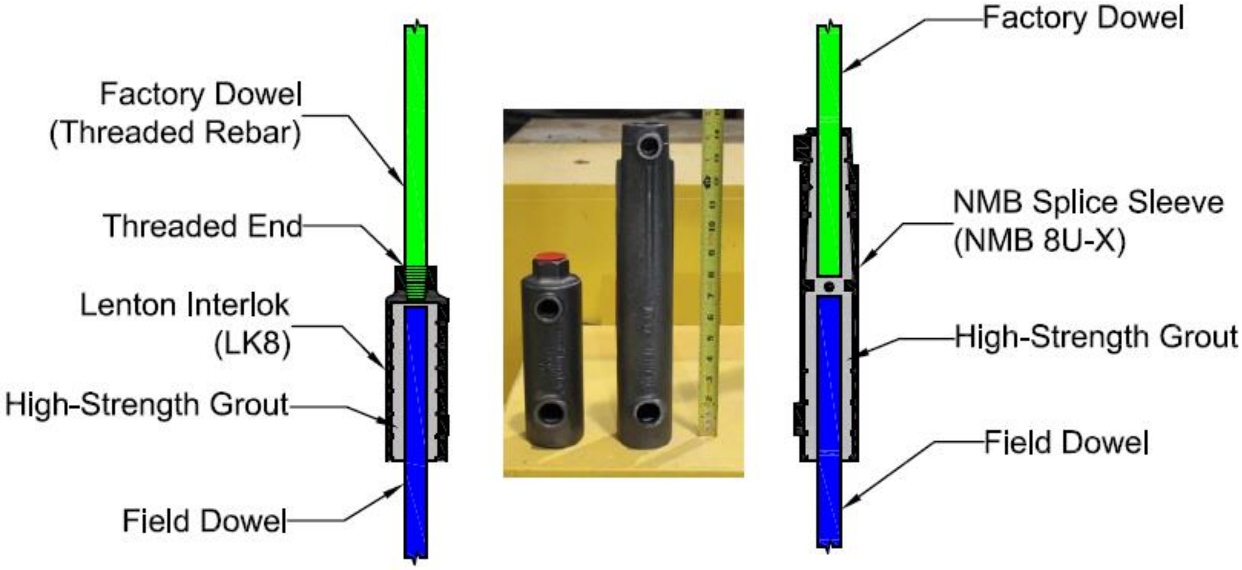

Figure 1.4 Two types of GSS incorporated in this research.

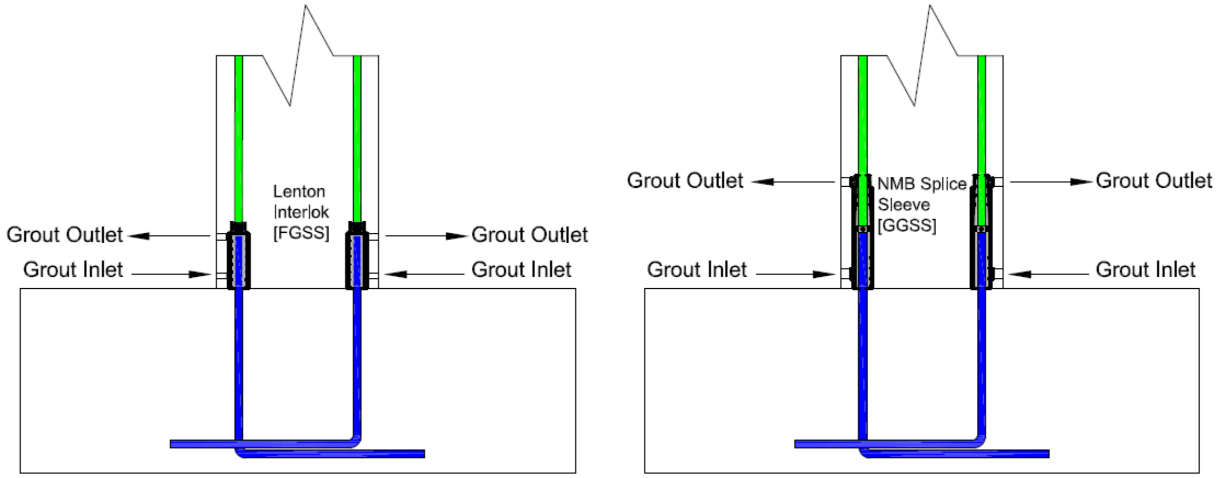

Figure 1.6 FGSS vs GGSS connections.

This research was geared toward conducting reversed cyclic tests on half-scale joint specimens connected by two different GSS connectors to investigate their seismic performance in comparison with conventional cast-in-place bridge construction.

Two main categories were specified for this experimental program based on the type of precast reinforced concrete components and sleeve type. Category-I specimens were column-to-footing joints in which GGSS connectors were incorporated in the column base or in the footing. Category-II specimens were column-to-cap beam joints by means of FGSS connectors in the column base or in the cap beam. A control specimen was constructed in each category representing a cast-in-place design of reinforced concrete components. The performance of the precast specimens is compared to that of the control specimens. The test matrix is shown in Table 1.1; Figure 1.7 presents the configuration alternatives in both categories for the tested specimens.

Table 1.1 Test matrix

	Test ID	**Connection Type**	**Designation**	**Sleeve Type**	**Sleeve Location**	**Other**
Category I	1	Column-Footing	GGSS-1	NMB-8UX	Column	
	2	Column-Footing	GGSS-2	NMB-8UX	Footing	
	3	Column-Footing	GGSS-CIP	NA	NA	Cast-In-Place
Category II	4	Column-Cap Beam	FGSS-1	LK-8	Column	
	5	Column-Cap Beam	FGSS-2	LK-8	Cap Beam	
	6	Column-Cap Beam	FGSS-CIP	NA	NA	Cast-In-Place

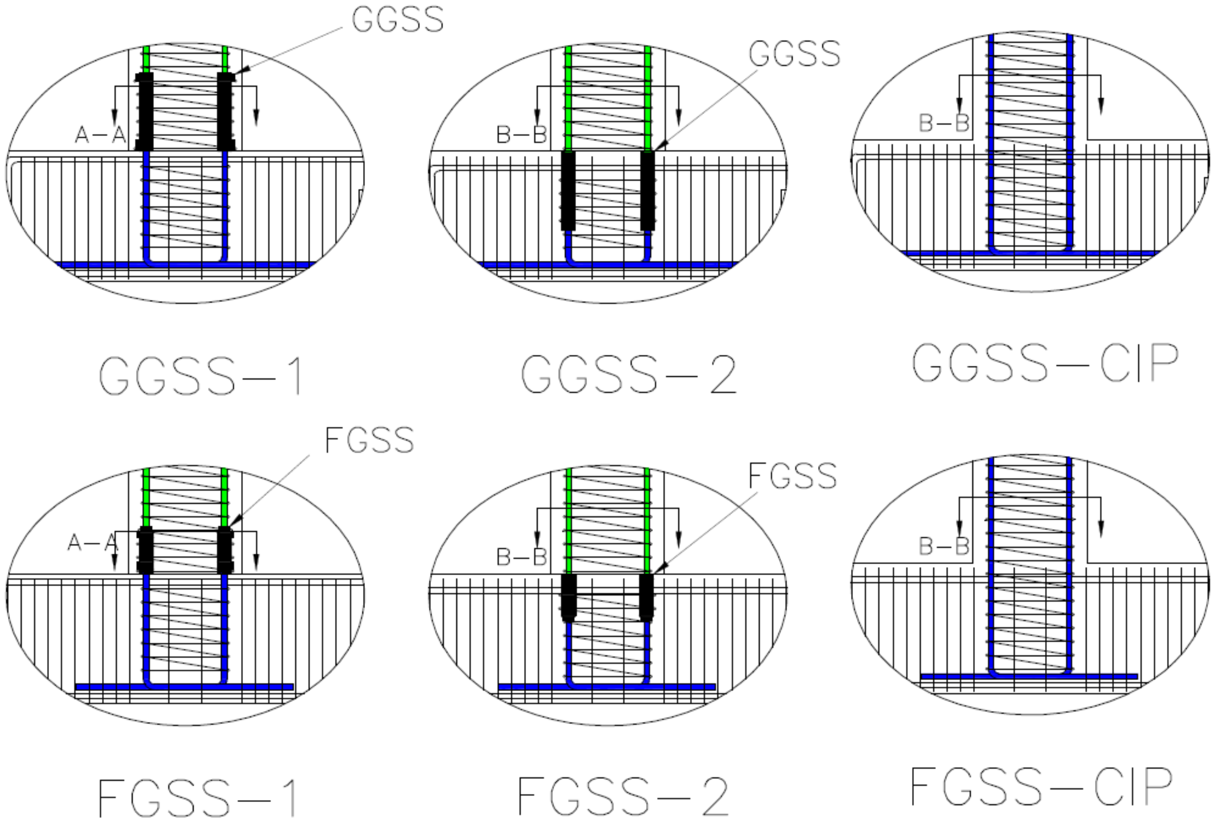

Figure 1.7 Configuration of test specimen alternatives.

The main objective of conducting this research was to gain more knowledge about GSS connectors and their properties, understand their seismic performance, and compare the performance of such connectors in precast joints to the performance of monolithic joints. The ultimate goal was to translate the findings of this research into design recommendations.

1.3 Outline of Report

This report was compiled in such a way as to clearly describe the sequence of tasks accomplished for carrying out the research. Section 2 provides background information on the design, detailing, and construction of the test specimens. Step-by-step construction procedures undertaken for each specimen are shown at the end of the section.

Section 3 is focused on the test procedure, including instrumentation and test setup. Various types of instrumentation used to collect data are described together with the quantity and location of each device. The test fixtures, data acquisition system, and loading protocol are discussed in depth before proceeding to the test results in Section 4. Test results are presented in depth for each test, accompanied by pertinent discussions on the specific criteria. Furthermore, characteristic results are presented in a comparative fashion within each category to offer a better understanding. Section 5 includes the summary of the report together with the most significant findings.

2. DESIGN AND CONSTRUCTION OF TEST SPECIMENS

2.1 Design of Test Specimens

The specimens were designed and detailed to simulate typical prototype bridges constructed in the state of Utah, following the AASHTO LRFD Bridge Design Specifications (2012) and the AASHTO Guide Specifications for LRFD Seismic Bridge Design (2011), in accordance with capacity-based design procedures [10, 16]. A circular configuration of column longitudinal bars and an octagonal column cross section were adopted to facilitate the process of pre-casting the columns, since this is the method of choice in Utah. Currently, the aforementioned design codes in addition to the Caltrans Seismic Design Criteria (SDC) inhibit the splicing of rebar, including mechanical anchorage devices, in the plastic hinge region of ductile members, for bridges located in moderate-to-high seismic regions [17]. In the AASHTO Guide Specifications for LRFD Seismic Bridge Design (2011), this would apply to Seismic Design Categories (SDCs) C and D. Thus, the preliminary design and detailing was developed for test specimens without any type of GSS, i.e., cast-in-place specimens for each category. The design was then adjusted to accommodate the GSS within the precast specimens as needed, and essential modifications were considered accordingly.

The test specimens were half-scale models of common prototype highway bridges in Utah. In order to achieve an acceptable test model, many multi-column bent cap systems were studied, including the Riverdale Road Bridge over I-84. The column dimensions, main longitudinal bars and configuration, and footing or cap beam dimensions were acquired by considering approximately 50% of the actual properties. Figure 2.1 depicts a sample prototype bent system in which areas of interest for this research are shown.

The column height for all specimens was selected to be 8 ft.-6 in. with a 21-in. square column head in the top 1 ft.-6 in. portion. The lateral load, however, was intended to be applied at a height of 8 ft. from the column end. The cross section changed to an octagon along the remainder of column height to facilitate casting of concrete. Six No. 8 bars in a circular arrangement, in addition to a No. 4 spiral with a pitch of 2½ in., made up the column steel cage. The longitudinal and volumetric transverse reinforcement ratios were 1.3% and 1.9%, respectively.

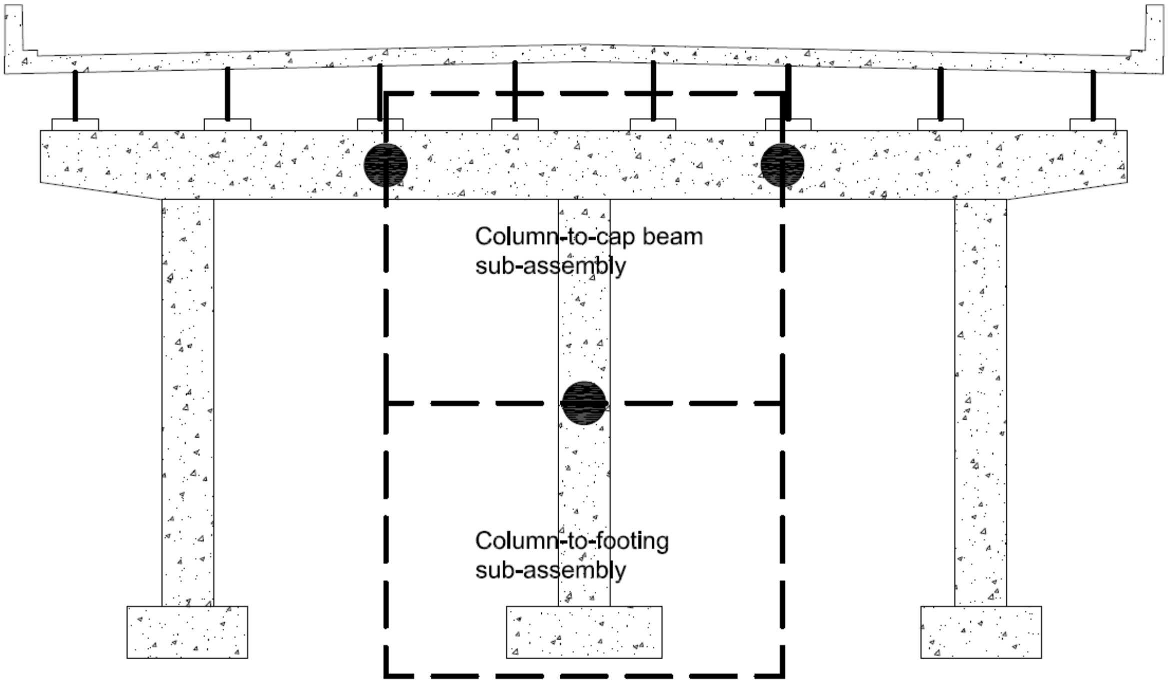

Figure 2.1 Prototype bridge with highlighted portions representing specimen design.

A series of sectional analyses was carried out to design the footing and cap beam. The results from such analyses were also used in the determination of proper instrumentation devices. For instance, the ultimate curvature values, obtained from a moment-curvature analysis, were used to select linear variable differential transformers (LVDT), with a desirable maximum stroke. A preliminary nonlinear static analysis was performed to predict the maximum lateral load and displacement. The footing and cap beam were designed so as not to be severely damaged under that maximum predicted load. Probable material properties for a grade 60 steel and concrete were assumed in this preliminary study. Figure 2.2 presents one such analysis with concrete having a 28-day compressive strength of 6 ksi, steel with a yield strength of 68 ksi, and an axial load corresponding to 9% of the axial compression capacity of the column.

The footing was designed as a 6-ft. long x 3-ft. wide x 2-ft. deep precast concrete element and consisted of No. 8 longitudinal bars enclosed by No. 4 double hoops. The cap beam was designed as a 9-ft. long x 2-ft. wide x 2-ft. deep precast beam; it had the same rebar size and arrangement as the footing. The footing and cap beam were designed to remain linearly elastic and not undergo plastic deformation. The design inhibits shear failure from occurring in the column; the desirable column failure mode is set to either be flexural or splice failure.

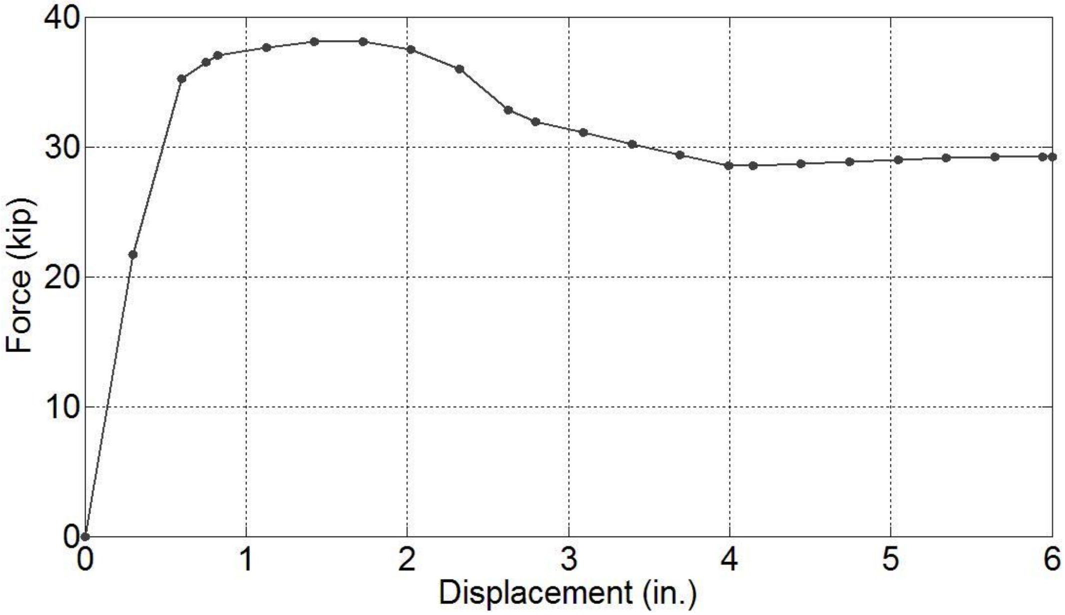

Figure 2.2 Preliminary pushover analysis on monolithic specimen (prediction).

Figure 2.3 shows the dimensions and details of the reinforcement, with a focus on the joint region, for both categories of specimens without the presence of the GSS connectors. This could be considered as the monolithic construction commonly used in cast-in-place construction. The design details for each test specimen are summarized in the next section. Dowel bar tails were bent inward to achieve better performance under lateral cyclic loads. This is a required provision for SDC D in accordance with the AASHTO specifications for LRFD seismic bridge design [16].

2.1.1 AASHTO-Seismic Provisions

A summary of AASHTO-Seismic provisions pertinent to the design and detailing of the test specimens is provided in Table 2.1. All provisions stated herein are associated with reinforced concrete components, which are addressed in Chapter 8 of the seismic code [16]. Article number, equation, and comments on each particular item are presented in a table format including the definition of relevant parameters.

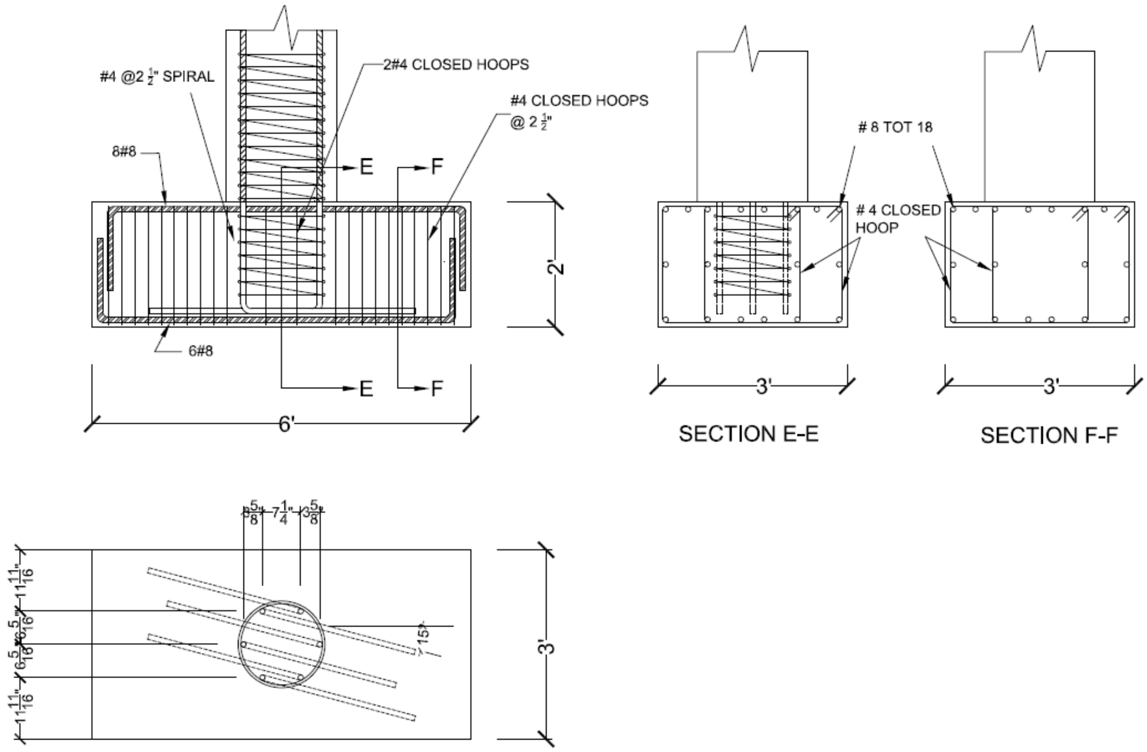

(a) Column-to-footing joint detailing.

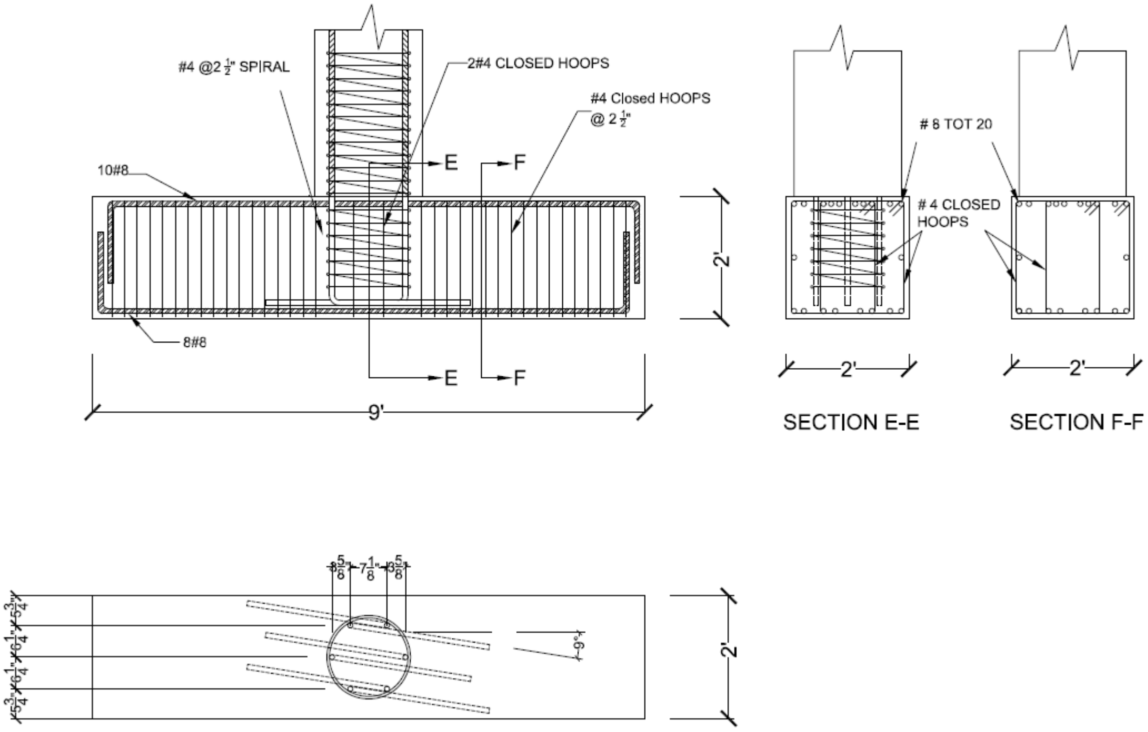

(b) Column-to-Cap beam joint detailing.

Figure 2.3 General design and detailing of joint region for both categories of specimens.

Table 2.1 AASHTO-Seismic provisions pertinent to design and detailing of specimens.

Article Number	Subject	Equation	Parameters	Remarks
8.4.1	Rebar type	NA	NA	ASTM A 706 rebar was used
8.4.2	Stress properties of rebar	NA	NA	Proper rebar properties used in design process
8.4.4	Concrete properties	$f'_{ce} \geq 1.3 f'_c$ $\varepsilon_{cu} = 0.005$	f'_c = 28-day concrete compressive strength f'_{ce} = Expected concrete compressive strength ε_{cu} = Ultimate compressive strain	Used in modeling confined and unconfined concrete
8.5	Column moment capacity	$M_{po} = \lambda_{mo} M_p$ $\lambda_{mo} = 1.2$	M_p = Plastic moment capacity M_{po} = Overstrength plastic moment capacity	For ASTM A 706 rebar

Article Number	Subject	Equation	Parameters	Remarks
			λ_{mo} = Overstrength magnifier	
8.6.2	Concrete shear capacity	$v_c = \alpha'(1+\frac{P_u}{2A_g})\sqrt{f'_c}$ $\alpha' = \frac{0.03}{\mu_D}\rho_s f_{yh}$ $\rho_s = \frac{4A_{sp}}{sD'}$	v_c = Concrete shear capacity P_u = Ultimate compressive force A_g = Gross area of member μ_D = Maximum local displacement ductility f_{yh} = nominal yield strength of transverse rebar A_{sp} = area of transverse rebar s = Transverse rebar spacing or pitch D' = Diameter of hoop or spiral	Used to compute shear capacity of column

Article Number	Subject	Equation	Parameters	Remarks
8.6.3	Rebar shear capacity	$V_s = \frac{\pi}{2}(\frac{nA_{sp} f_{yh} D'}{s})$	n = Number of spiral or hoop core sections	Used to compute shear capacity of column
C8.6.3	Longitudinal rebar spacing	NA	NA	Maximum spacing of column longitudinal bars limited to 8 in.
8.6.5	Minimum shear reinforcement	$\rho_s \geq 0.005$		Holds true for test specimens
8.7.1	Minimum lateral strength	$M_{ne} \geq 0.1P_{trib}(\frac{H_h + 0.5D_s}{\Lambda})$	M_{ne} = Nominal moment capacity P_{trib} = Greater of dead load or force associated with tributary seismic mass H_h = Column height D_s = Depth of superstructure Λ = Fixity factor per 4.8.1 [16]	

Article Number	**Subject**	**Equation**	**Parameters**	**Remarks**
8.7.2	Maximum axial load	$P_u \le 0.2 f'_c A_g$		Axial load level kept below this value for all test models
8.8.1	Maximum column longitudinal rebar	$A_l \le 0.04 A_g$	A_l = Area of longitudinal reinforcement	Actual rebar ratio provided is 0.013
8.8.2	Minimum column longitudinal rebar	$A_l \ge 0.01 A_g$		Actual rebar ratio provided is 0.013
8.8.3	No splicing of rebar in plastic hinge zone of ductile members	NA	NA	No splicing of column bar in monolithic specimens
8.8.4	Anchorage length	$l_{ac} \ge \frac{0.79 d_{bl} f_{ye}}{\sqrt{f'_c}}$	l_{ac} =Anchorage length d_{bl} = diameter of longitudinal column bar f_{ye} = Expected yield strength of longitudinal column bar	Accommodated in monolithic specimens. Tails should be pointed inward for SDC D.

Article Number	Subject	Equation	Parameters	Remarks
8.8.6	Maximum bar diameter	$d_{bl} \le \frac{0.79\sqrt{f'_c}(L - D_c)}{f_{ye}}$	D_c = Column depth	
8.8.7	Lateral reinforcement inside plastic hinge region	NA	NA	At spiral discontinuities, spiral shall terminate with one extra turn plus a tail equal to the cage diameter. For all precast test specimens, two extra turns were provided.
8.8.8	Lateral reinforcement outside plastic hinge region	NA	NA	Provide 50% of required lateral reinforcement in plastic hinge region. The same lateral rebar ratio (1.9%) in plastic hinge region was provided for all specimens.
8.8.9	Lateral reinforcement detailing	NA	NA	Seismic hooks consist of a 135° bend, plus an extension of not less than the larger of 6 bar diameters or 3 in.

Article Number	Subject	Equation	Parameters	Remarks
8.13.2	Joint proportioning	$p_c \leq 0.25 f'_c$ $p_t \leq 0.38\sqrt{f'_c}$	p_c = Principal compressive stress p_t = Principal tensile stress	All test specimens conformed to this provision.
8.13.3	Minimum joint shear reinforcement	$\rho_s = \frac{0.4A_{st}}{l_{ac}^2}$	A_{st} = Total area of column reinforcement anchored in the joint	Actual value for test specimens exceeded this limit.
8.13.4.1.2a	Vertical stirrups	$A_s^{jv} \geq 0.2A_{st}$	A_s^{jv} = Vertical stirrup area	Vertical stirrups distributed over Dc/2 on each side of joint region.
8.13.4.1.2b	Horizontal stirrups	$A_s^{jh} \geq 0.1A_{st}$	A_s^{jh} = Horizontal stirrup area	Maximum vertical spacing of these bars shall be 18 in.
8.13.4.1.2b	Horizontal side reinforcement	$A_s^{sf} \geq Max\{0.1A_{Cap}^{Top}, 0.1A_{Cap}^{Bot}\}$	A_s^{sf} = Horizontal side reinforcement A_{Cap}^{Top} = Area of cap beam top flexural rebar A_{Cap}^{Bot} = Area of cap beam bottom flexural rebar	Side bars were provided to conform to this article.

2.2 Footing Joints

Three column-to-footing joints are described in this section: the precast test specimens GGSS-1 and GGSS-2, and the cast-in-place specimen GGSS-CIP. The geometric properties of the test models along with the reinforcement configuration were identical. The GGSS connectors were incorporated in the column base of the GGSS-1 and in the footing of the GGSS-2 to splice the reinforcing bars.

2.2.1 GGSS-1

Precast specimen GGSS-1 was composed of a precast column with six GGSS connectors embedded in the column end, and a precast footing with projected dowel bars for a length of 7 in. Rebar cages were constructed in the Structures Laboratory at the Department of Civil and Environmental Engineering of the University of Utah. The precast column was first built by fastening the GGSS connectors to a wooden template by means of pin setters. Column longitudinal bars were then inserted inside the GGSS connectors, which were confined by a closely-spaced steel spiral. The spiral used over the GGSS region had a 1¾-in. larger diameter than the spiral for the remaining portion of the column, due to the larger diameter of the GGSS connectors compared with column longitudinal bars. This resulted in an overlapping spiral region right above the GGSS region. Beginning with dowel bars, the precast footing was then constructed by arranging the footing core rebar cage in a circular configuration along with staggering inward angled tails. The dowel bar tails measured 2 ft.-6 in. to extend out from the core and provide a stable base for the dowel rebar cage. Figure 2.4 shows the precast components under construction.

(a) Column end GGSS and overlapping spiral. (b) Footing dowel bars with inward tails.

Figure 2.4 GGSS-1 precast components under construction.

Longitudinal and transverse bars were tied at every bar intersection to achieve a robust rebar cage. This was significant because cages had to be transported to the precast plant for casting concrete. Figure 2.5 shows the details of specimen GGSS-1 and the rebar cages that formed the test model. Wooden templates, as shown, were utilized in the construction process to prevent mismatch of the precast components. Figure 2.6 shows the GGSS-1 column and footing reinforcement inside the forms at the precast plant. Concrete casting was performed with great care to avoid damage to instrumentation wires.

According to ASTM C39 [18], 4 in. x 8 in. cylinders were made to perform compression tests before removing the specimens from the forms, at 28 days after casting, and on test day. One-and-one-half-inch-diameter PVC pipes were inserted inside the footing cage to provide room for anchors that would clamp the specimen down to the testing frame. The average concrete compressive strength at 28 days for this specimen was 5.3 ksi.

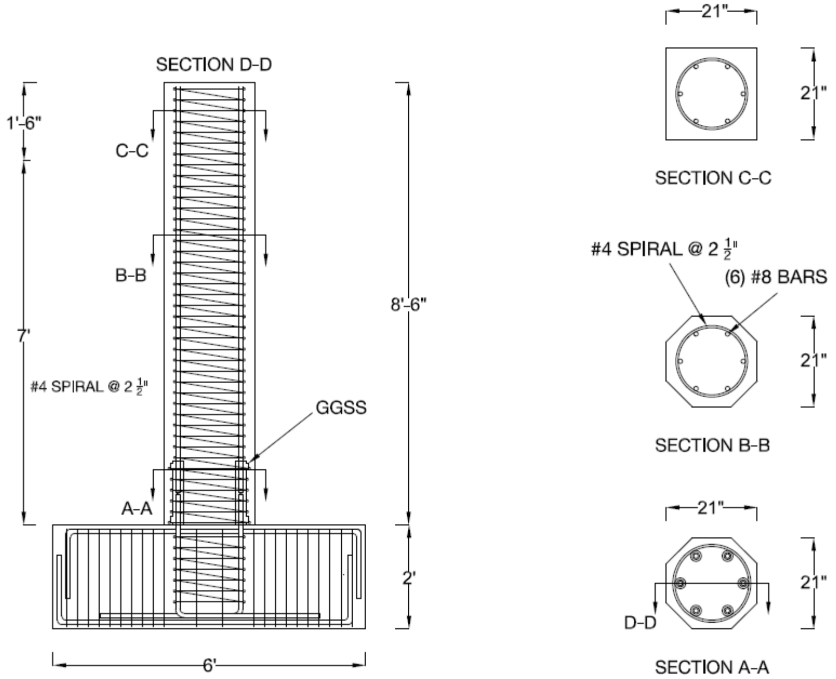

(a) Details of GGSS-1.

(b) Column and footing rebar cages.

Figure 2.5 GGSS-1 specimen details and rebar cages.

Figure 2.6 GGSS-1 precast components inside forms.

The precast components were taken out of the forms when concrete strength had reached 3 ksi. A step-by-step procedure was carried out for the grouting operation, in which the grout was pumped into the sleeves, when connecting the precast components. A proprietary non-metallic, non-shrink, early high strength grout, particularly developed for this type of GSS connector, was used in accordance with manufacturer instructions. One 55-lb. bag of grout gradually mixed with 0.98 gallons of water was sufficient to fill all six GGSS connectors and cast the bed grout at the interface of the two components. An electric mixer with a Jiffler paddle was used to continuously mix the grout with water for 2½ minutes. A grout flow test indicated that the grout was in satisfactory condition with an acceptable puddle diameter of 6.5 in. A Kenrich GP-2HD hand pump was utilized to pump the grout into the GGSS connectors by inserting the nozzle into the bottom port. Following the ASTM C109 instructions, several 2-in. cubes were made to obtain the 28-day and test-day compressive strength of the grout [19].

A ¼-in. bed grout was incorporated at the column-to-footing interface by placing proper size spacers at the interface of the column and footing. A square wooden frame was made to pour the bed grout, as demonstrated in Figure 2.7. The column was lowered slowly, making sure that it rested plumb and level on the footing.

The specimen remained attached to the testing frame for a minimum of 28 days before testing for the grout to cure completely. In the meantime, test preparation and external instrumentation were carried out. The average compressive strength of the grout at 28 days was found to be 14.4 ksi. Figure 2.8 displays specimen GGSS-1 in the final testing position at the end of the grouting operation.

Figure 2.7 Grouting operation for GGSS-1.

Figure 2.8 GGSS-1 in the final position.

2.2.2 GGSS-2

The second alternative in the column-to-footing joint category was to change the location of the GGSS connectors from the column end to the top of the footing. In other words, dowels protruded 7 in. from the column end. This option was investigated primarily because the AASHTO-Seismic Code [16] does not currently prohibit such an application, as the GGSS connectors would be outside the column plastic hinge region; however, the response of such a joint under simulated ground motions has not been well documented. This particular configuration was implemented in the Provo to Salt Lake Frontrunner rail bridge project in which both column-to-footing and column-to-cap beam joints incorporated GGSS connectors outside the piers. On the other hand, a less severe disruption of the commonly adopted column plastic hinge region, located at the column end, was anticipated by shifting the location of the GGSS connectors from the column to the footing.

In the construction phase, the column was built first because there was no special consideration, due to the GGSS connectors not being in the column. Therefore, six No. 8 bars were arranged in a circular configuration using a wooden template. Next, a No. 4 spiral was wrapped around the column main bars. The GGSS connectors were fastened to a wooden template by means of pin setters to be placed in the top portion of the footing. Figure 2.9 shows the precast components under construction. Figure 2.10 displays the footing core rebar cage placed on the footing main bottom bars and tied firmly to the rest of the reinforcement; the core was level in all directions. Construction of the precast footing was carried out with some level of practical difficulty because of a highly congested rebar zone within the joint area. This issue made other phases relatively more complicated, too, such as instrumentation and casting of concrete. The tails shown in Figure 2.10 had a length of 2 ft.-4 in. and were oriented inward parallel to other rebar tails, in a plane intersecting the plane of the main footing bars.

The rebar cages became sturdy by tying the longitudinal bars to the transverse bars at all corners in order for the cages not to get distorted while transporting them to the precast plant, where concrete would be cast. The details of specimen GGSS-2 are presented in Figure 2.11 and the rebar cages for the test model are presented in Figure 2.12.

Concrete was cast under a highly supervised condition to avoid damage to instrumentation wires. 4 in. x 8 in. concrete cylinders were taken for compression tests before removing the specimens from the forms, at 28 days after casting, and on the test day. One-and-one-half-inch diameter PVC pipes were placed inside the footing where the support bolts would be inserted to attach the specimen to the test frame. Figure 2.13 shows the GGSS-2 precast components in the forms right before concrete was cast. The average compressive strength of the concrete for specimen GGSS-2 was 3.9 ksi at 28 days.

(a) Column cage with projecting bars. (b) GGSS fastened to template for the footing.

Figure 2.9 GGSS-2 precast components under construction.

Figure 2.10 GGSS-2 precast footing core rebar cage.

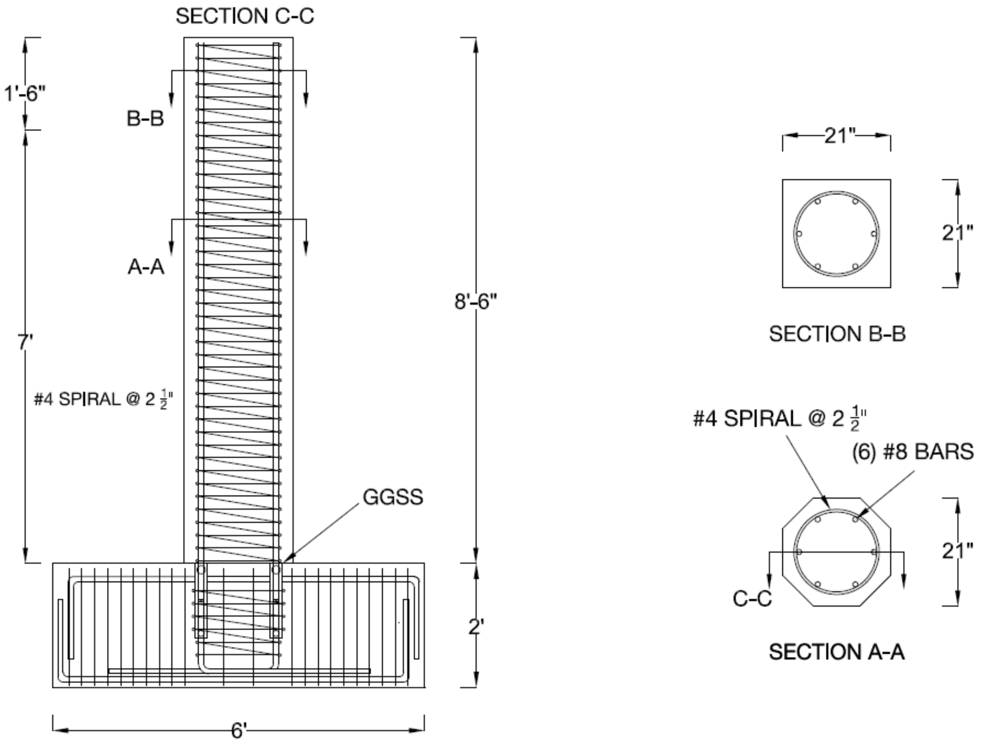

Figure 2.11 Details of GGSS-2.

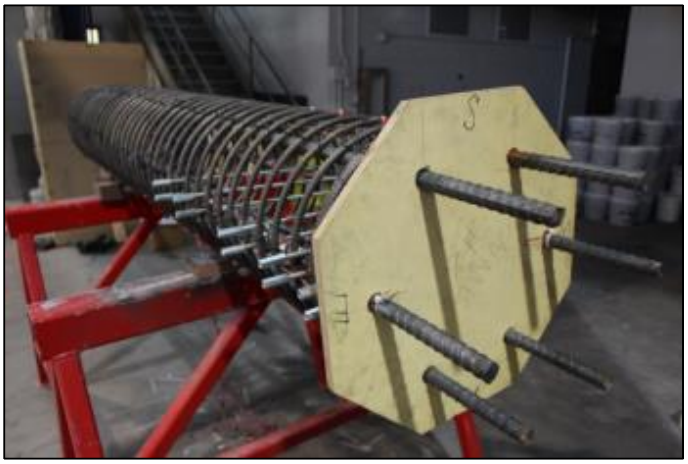

(a) Column rebar cage.

(b) Footing rebar cage.

Figure 2.12 GGSS-2 rebar cages.

Figure 2.13 GGSS-2 precast components inside forms.

The precast pieces were removed from the forms when concrete had reached a compressive strength of 3 ksi. A step-by-step grouting operation was followed in accordance with the manufacturer instructions as described in Section 2.2.1 for GGSS-1. In contrast to the grouting operation for GGSS-1, a pre-grout installation technique was adopted to facilitate the erection process. In this process, plastic plugs were used to seal the GGSS connector inlet and outlet before casting concrete. During the installation, all the GGSS connectors were first filled with grout from the wide end opening. A Kenrich GP-2HD hand pump was utilized to pump the grout into the GGSS connectors by inserting the nozzle into the wide end opening.

A ¼-in. bed grout was incorporated at the column-to-footing interface by placing proper size spacers at the interface between the column and footing. A square wooden dam was made to pour the bed grout, as demonstrated in Figure 2.14. The column was lowered into position gradually and slowly, making sure that it rested plumb and level on the footing.

Figure 2.14 Grouting operation for GGSS-2.

Temporary wood bracing was used to prevent movement of the GGSS-2 column until the grout developed sufficient strength. This specimen remained attached to the test frame for a minimum of 28 days before testing for the grout to cure completely. In the meantime, test preparation and external instrumentation were carried out. The average compressive strength of the grout at 28 days was found to be 11.1 ksi. Figure 2.15 displays specimen GGSS-2 in the final testing position, at the end of the grouting operation.

Figure 2.15 GGSS-2 in final position.

2.2.3 GGSS-CIP

GGSS-CIP was the control specimen in this connection category; i.e., column-to-footing joints. It represents monolithic construction without any GGSS connectors to splice the reinforcement. The results from experimental tests on the precast column-to-footing specimens will be compared to the test results for the GGSS-CIP. The spiral reinforcement did not have any splice either, confining the core concrete from the top of the column monolithically down to the bottom of the footing as a single long helical reinforcement around the longitudinal bars. The diameter of the spiral was kept the same as for the spiral around the column bars for the precast GGSS-1 and GGSS-2 specimens, implying an identical moment arm for column longitudinal bars in both test specimens.

Construction of specimen GGSS-CIP began by building the column rebar cage with the same wooden template as the precast test models. Supported by a forklift, the column longitudinal bars were tied to the spiral at every corner from the bottom toward the column top, as shown in Figure 2.16.

Tails of the column hooked bars were 2 ft.-6 in. long and oriented into the joint core to conform to the AASHTO-Seismic Code and also to provide a stable base for the column rebar cage during construction. Figure 2.17 shows the details of the GGSS-CIP specimen in addition to the final rebar cage.

The constructed rebar cage was transported to the precast plant to cast the concrete. Figure 2.18 shows this monolithic component sitting in the form prior to casting. Several 4 in. x 8 in. cylinders were made to obtain the concrete compressive strength at different ages, including before removal of the specimen from the form, at 28 days, and on the test day. As presented in Figure 2.18, 1½" diameter PVC tubes were embedded inside the footing cage in order to fasten the specimen to the test frame. The average concrete compressive strength of this specimen was 5.2 ksi at 28 days.

Specimen GGSS-CIP was taken out of the form and transported back to the Structures Laboratory when the concrete strength had reached 3 ksi; it was fastened to the test frame while test preparation procedures were implemented. Figure 2.19 displays the test specimen in the final testing position.

Figure 2.16 Construction of GGSS-CIP.

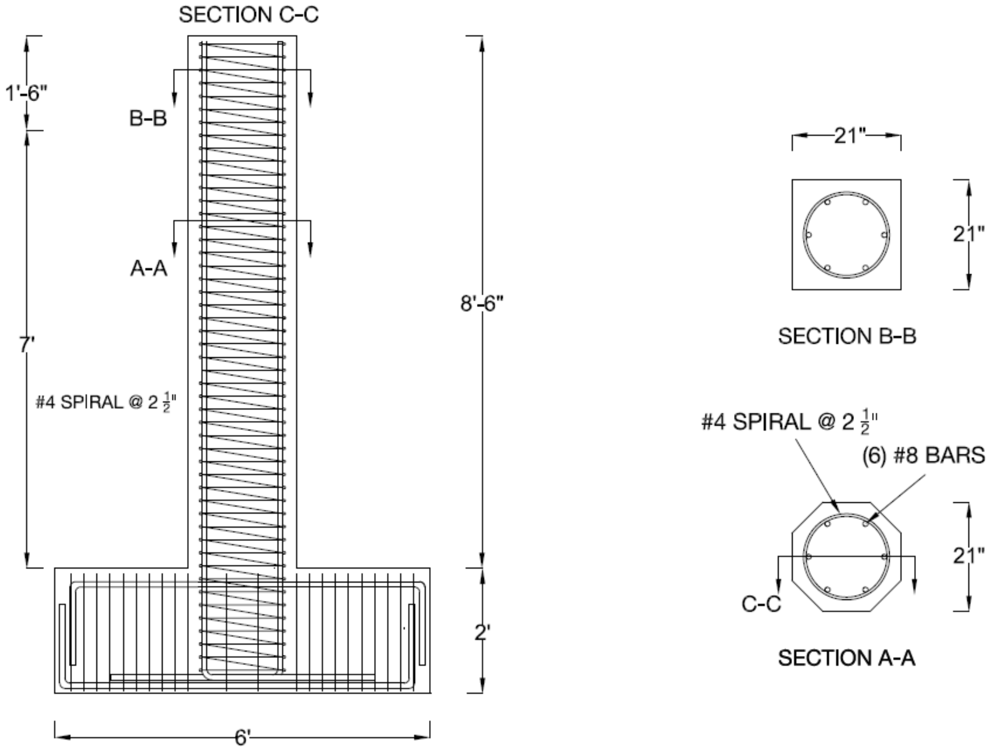

(a) Details of GGSS-CIP.

(b) Rebar cage ready to cast concrete.

Figure 2.17 GGSS-CIP specimen details and rebar cage.

Figure 2.18 GGSS-CIP rebar cage inside form.

Figure 2.19 GGSS-CIP in final position.

2.3 Column-to-Cap Beam Joints

Three column-to-cap beam joints are described in this section, precast specimens FGSS-1 and FGSS-2, and cast-in-place specimen FGSS-CIP. The geometric properties of the test models in addition to the reinforcement configuration were identical for all test models.

The GSS connector used to build the precast models in this category was referred to as the FGSS connector earlier in this report, denoting the existence of a fastened rebar to the factory end of the FGSS. In other words, the column rebar was threaded to the top end during the construction of rebar cages, and the dowel bar protruding from the cap beam was grouted at the bottom end while installing the test specimen for the FGSS-1 test, and vice versa for the FGSS-2 test.

2.3.1 FGSS-1

The first specimen studied in this category was composed of a precast column with FGSS connectors embedded in the column end and a precast cap beam with 7-in. projected dowel bars.

Column longitudinal bars were fastened to the threaded end of the FGSS connectors in the first step of the construction phase. All bars were initially hand-tightened, which took about four turns, then tightened up with a pipe wrench. A form mounting fixture was implemented to fasten the FGSS connectors to a wooden template to arrange column bars in the desired configuration. A No. 4 spiral with a pitch of 2.5 in. was used to confine the column longitudinal bars. The spiral over the FGSS region had a 1 5/8-in. larger diameter than the spiral for the rest of the column due to the larger diameter of the FGSS connector compared with the column longitudinal rebar. This resulted in an overlapping spiral region right above the FGSS connectors.

The cap beam was built similar to the footing, in which the circular joint core was first constructed by tying the hooked dowel bars to a spiral of equal diameter as the column spiral. The tails of these bars were 2 ft.-4 in. long, pointed inward to comply with the design code and to provide a stable joint core. **Figure**Figure 2.20 shows the precast components under construction.

Tie wires were used extensively to achieve a sturdy rebar cage in order for the cages not to become distorted during transportation to the precast plant for casting concrete. Details of specimen FGSS-1 are presented in Figure 2.21, and the final rebar cages making up the test model are shown in Figure 2.22.

(a) Column end FGSS and overlapping spiral. (b) Cap beam dowel bars with inward tails.

Figure 2.20 FGSS-1 precast components under construction.

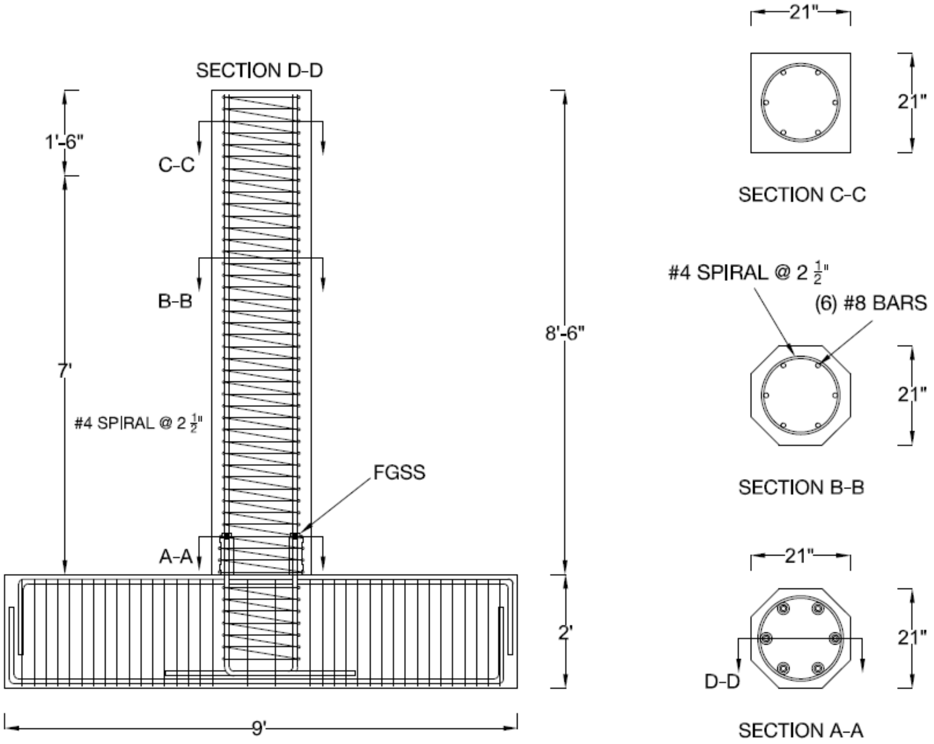

Figure 2.21 Details of FGSS-1.

The dowel bars protruding from the cap beam in Figure 2.22 were left considerably longer than required before casting the concrete. This was mainly done to keep the joint core plumb and sturdy using two wooden templates on the dowel bars. These bars were cut to the required length of 7 in. right before assembling the precast components.

(a) Column rebar cage.

(c) Cap beam rebar cage.

Figure 2.22 FGSS-1 rebar cage.

Concrete was cast in a highly supervised condition to avoid introducing damage to the instrumentation. PVC pipes, 1½” in diameter, were positioned inside the cap beam form to accommodate the interior support rods that were going to be used in fastening the specimen to the test frame. Several 4 in. x 8 in. concrete cylinders were prepared to obtain the compressive strength of concrete at specified time intervals before the experiment. Figure 2.23 displays the FGSS-1 precast components inside the formwork before concrete testing. The 28-day compressive strength of this concrete was 5.3 ksi.

The precast concrete components were removed from the forms once the compressive strength of the concrete reached 3 ksi and were transported back to the Structures Laboratory where the experiments were conducted. The last step before conducting the tests was to install the precast components and grout the FGSS connectors and interface. A proprietary high strength and ready-to-mix grout, exclusively formulated to be used with this particular type of GSS, was used in accordance with the instructions in the FGSS manual. A single 50-lb bag of grout mixed with 0.7 gallons of water was sufficient to fill up all six FGSS connectors and cast the bed grout. The grouting operation was very similar to the procedure undertaken for the column-to-footing connections. An electric mixer with a Jiffler paddle was utilized to continuously mix the grout with water for five minutes. The flow test carried out after mixing indicated that the grout had a good consistency with an acceptable spread diameter of 5 in. In general, this grout had less fluidity than the one used for the GGSS specimens, therefore the grouting operation was relatively more cumbersome. Figure 2.24 shows the precast components during the grouting operation, where a wooden dam was built on the cap beam to facilitate casting of the ¼-in. bed grout.

The column was lowered slowly and dowel bars were inserted into the corresponding FGSS connectors. As described earlier, a hand pump was utilized to pump the grout into the FGSS connector's bottom port. Both inlet and outlet ports were plugged when the FGSS connectors were completely filled with grout. Several 2-in. grout cubes were made to obtain the compressive strength of the grout at desirable time intervals.

Figure 2.23 FGSS-1 precast components inside concrete forms.

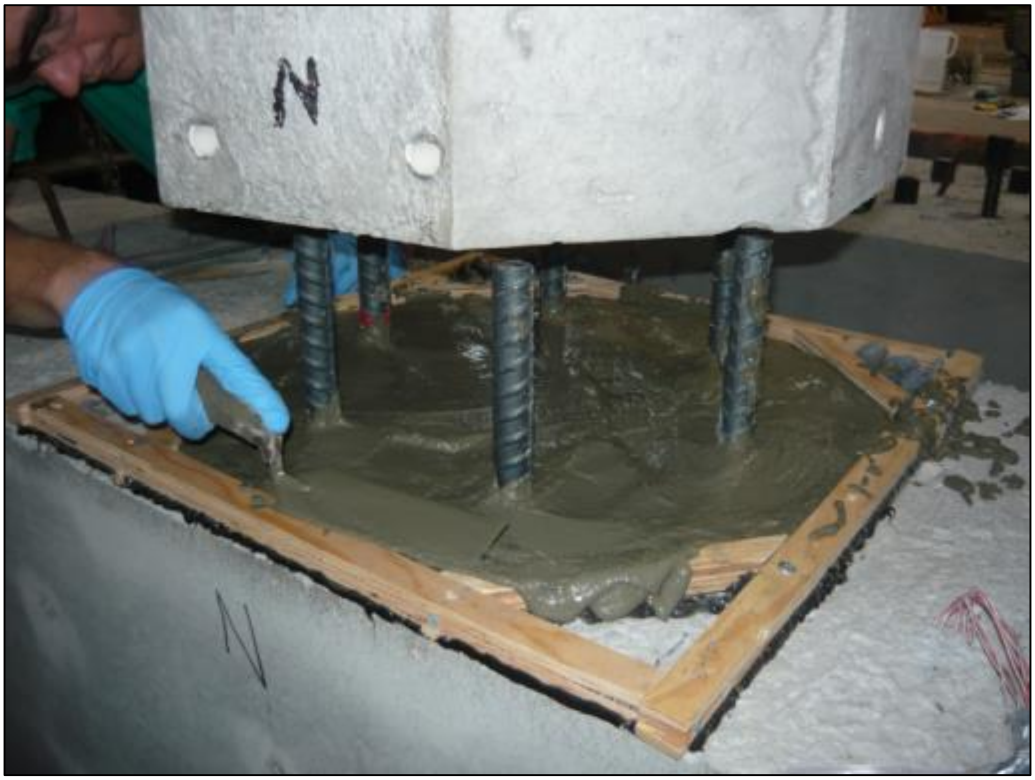

Figure 2.24 Grouting operation for FGSS-1

Specimen FGSS-1 remained connected to the test frame until the grout developed sufficient strength. In the meantime, test preparations were performed. This specimen is displayed in Figure 2.25 in the final position after the grouting operation; note that this configuration was tested with the cap beam in the inverted position for ease of testing. The average compressive strength of the grout at 28 days was 12.5 ksi.

Figure 2.25 FGSS-1 (back) in final position.

2.3.2 FGSS-2

The location of the FGSS connectors was changed from the column end to the cap beam for this specimen. This was equivalent to the second alternative described in the previous section for the column-to-footing specimen GGSS-2. Such a change in the connection of the two precast components would make it conform to the design code because the FGSS connectors would not be in the plastic hinge zone of the column. Another significant reason for examining this alternative was to investigate the performance of this specimen in which the disruption to the plastic hinge region of the column was reduced with respect to specimen FGSS-1.

The precast column rebar cage was built first. Six No. 8 bars in a circular arrangement were confined by a No. 4 spiral with a pitch of 2.5-in. dowel bars, 7-in.-long protruded from the column end, as shown in Figure 2.26(a). The joint core was built and centered in the cap beam. Threaded hooked bars were previously tightened on the FGSS connectors by means of a pipe wrench and arranged in a circular fashion using a template. Horizontal joint reinforcement consisting of a closely spaced spiral was tied to both the vertical hooked bars and the FGSS connectors, as shown in Figure 2.26(b). Tails of the hooked bars were oriented into the joint core and had a 2 ft.-4 in. length.


(a) Column rebar cage with projecting bars. (b) FGSS placed within cap beam.

Figure 2.26 FGSS-2 precast components under construction.

Tie wires were used extensively to secure the joint core and, thus, minimize the likelihood of a mismatch between the column and cap beam. FGSS-2, like all other specimens, was transported to the precast plant for casting the concrete. General details of the test specimen are provided in Figure 2.27, which depicts the dimensions, arrangement of reinforcing bars, and sectional properties.

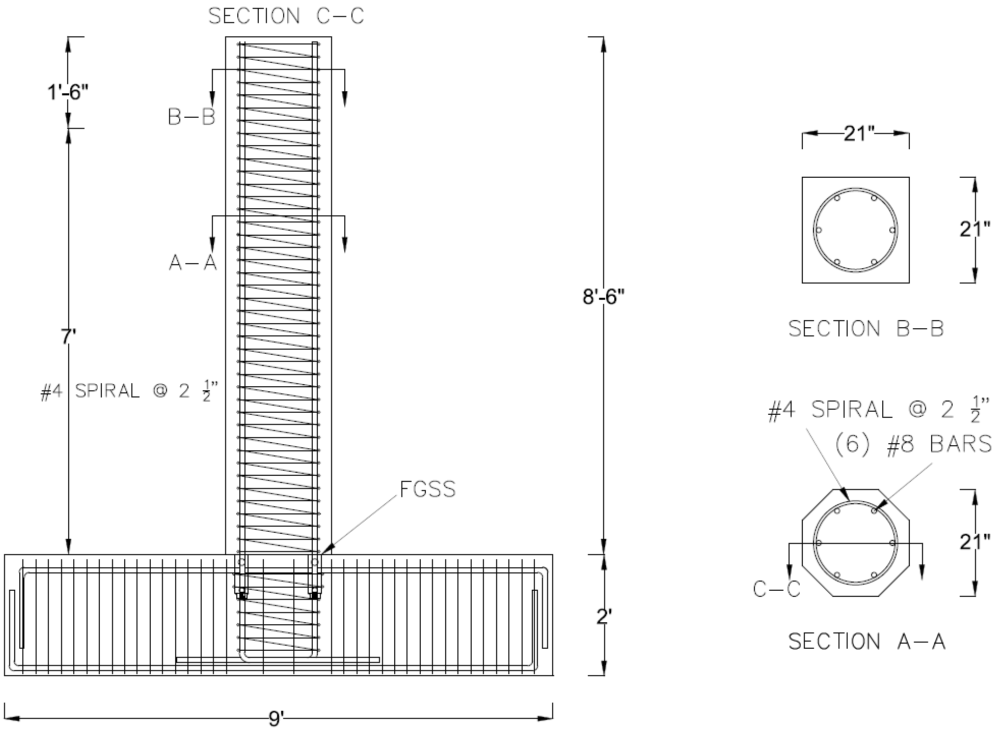

Figure 2.27 Details of FGSS-2.

The rebar cages that formed this specimen are shown in Figure 2.28. Double hoops used in the cap beam were uniformly distributed along the beam, and top and bottom layers of rebar were tied to double hoops. The entire shear reinforcement in the cap beam had seismic detailing in accordance with the seismic design code [16].

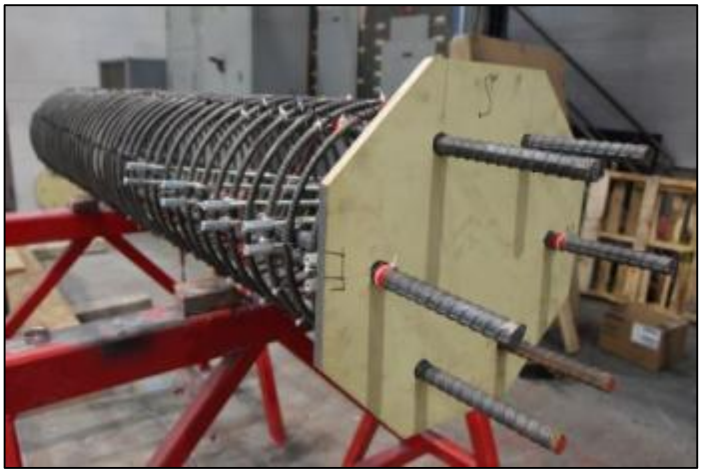

(a) Column rebar cage.

(b) Cap beam rebar cage.

Figure 2.28 FGSS-2 rebar cages.

Concrete was cast and several 4-in. x 8-in. cylinders were made from the same batch. These cylinders were used to obtain the concrete compressive strength at several times, such as lifting of the components from the concrete forms, 28-day strength, and on the test day. PVC pipes, 1½ in. diameter, were located in designated locations for support rods that would be used to secure the test specimen in the test frame. **Figure**Figure 2.29 shows the FGSS-2 precast components in the formwork. The average compressive strength of the concrete was 3.9 ksi at 28 days.

The precast components were removed from the forms when the concrete compressive strength reached 3 ksi. The grouting operation procedure was carried out as described for FGSS-1. The flow test showed an acceptable grout consistency with a spread diameter of 5.25 in., although it was hard to pump the grout with the Kenrich GP-2HD hand pump, which was used for this purpose. As opposed to the post-grout procedure followed for FGSS-1, in which the grout was pumped into each FGSS connector against gravity, a pre-grout technique was carried out in a similar approach to specimen GGSS-2. This was done to facilitate the installation process. To perform a pre-grout operation, both the inlet and outlet port of all FGSS connectors were sealed during construction of the rebar cages. During installation, all FGSS connectors were filled with grout from the wide end opening, as shown in Figure 2.30. Grout cubes were made to obtain the 28-day and test-day compressive strength of the grout.

Figure 2.29 FGSS-2 precast components inside concrete forms.

Figure 2.30 Grouting operation for FGSS-2.

When all six FGSS connectors were filled, grout was cast at the interface of the precast members. Several ¼-in. spacers were placed at the interface to achieve a desirable bed grout thickness. The column was gently set down into position and braced temporarily to prevent movement until the grout developed sufficient strength.

Compression tests on grout cubes indicated that the 28-day compressive strength of the FGSS-2 grout was 10.3 ksi, the lowest grout strength among all column-to-cap beam and column-to-footing specimens. Figure 2.31 shows this specimen fastened to the test frame in the Structures Laboratory.

Figure 2.31 FGSS-2 in final position.

2.3.3 FGSS-CIP

Specimen FGSS-CIP was the control test in the column-to-cap beam joint category. It represents monolithic construction without any FGSS connectors to splice the reinforcement. The results from the experimental tests on the precast FGSS-1 and FGSS-2 specimens are compared to the test results for FGSS-CIP in upcoming sections. The spiral reinforcement did not have any splice either, confining the core concrete from top to bottom of the column as a single long helical reinforcement around the longitudinal bars. The diameter of the spiral was kept the same as for the spiral around the column bars in the other two test models, thus ensuring an identical moment arm for column longitudinal bars.

Construction of this specimen began with building the column rebar cage by using the same wooden template as for specimens FGSS-1 and FGSS-2. The column longitudinal bars were tied to the spiral at every corner from the bottom toward the column top. Tails of the column hooked bars were 2-ft.-4-in. long and were bent inward to comply with the design code and achieve a sturdy base for the column rebar cage during construction. Once the column was completed, it was placed on the cap beam bottom reinforcement that was already positioned properly. The tails of the column rebar were then tied to the cap beam bottom reinforcement. Subsequently, cap beam double hoops, top reinforcement, and middle bars were added to complete the rebar cage. Figure 2.32 shows the joint area during the construction stage, and Figure 2.33 demonstrates the details of the FGSS-CIP and final rebar cage for this specimen.

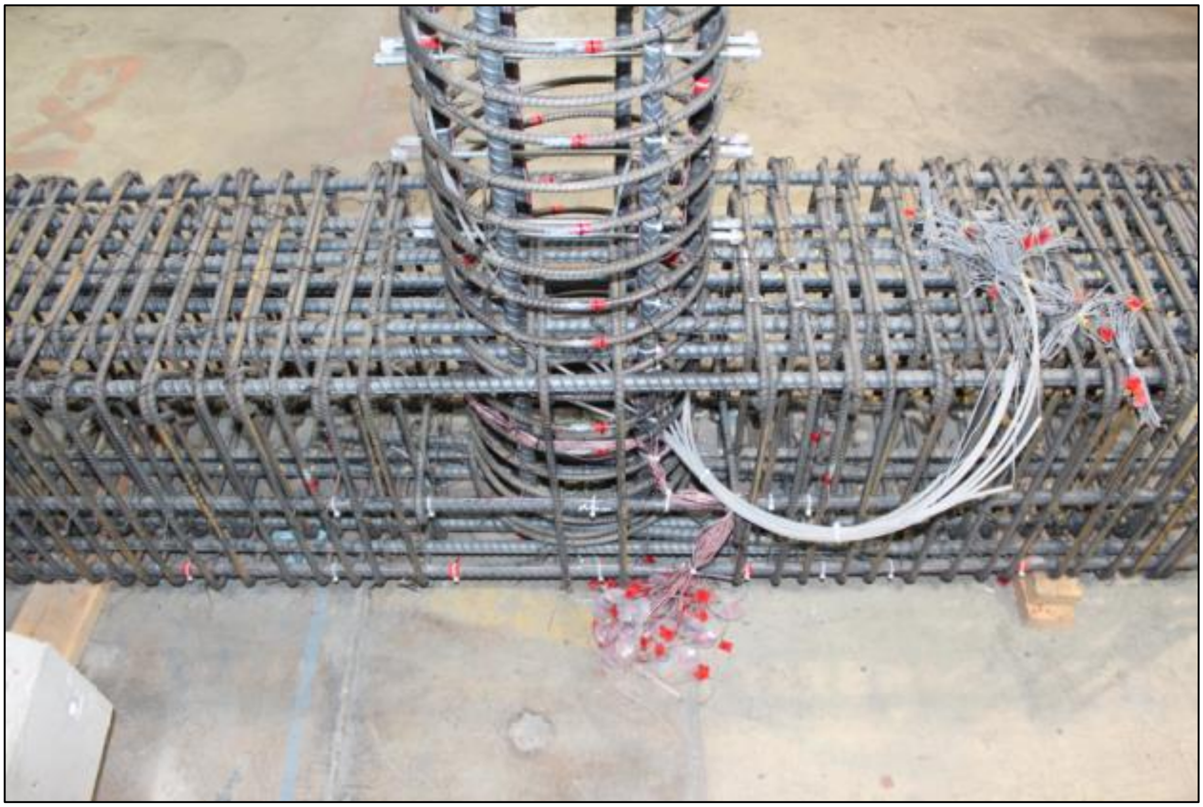

Figure 2.32 FGSS-CIP joint area.

The constructed rebar cage was transported to the precast plant to cast the concrete. Figure 2.34 shows this monolithic component in the formwork prior to casting. Several 4-in. x 8-in. cylinders were made to obtain the concrete compressive strength at different time intervals, including before removal of the specimen from the form, at 28 days, and on test day. PVC tubes, 1½ in. diameter, were embedded inside the cap beam cage in order to fasten the specimen to the test frame. The average concrete compressive strength was 5.2 ksi at 28 days.

Specimen FGSS-CIP was taken out from the form and transported back to the Structures Laboratory once the concrete strength had reached 3 ksi. The specimen was fastened to the test frame while test preparation procedures were implemented. Figure 2.35 displays the test specimen in the final testing position.

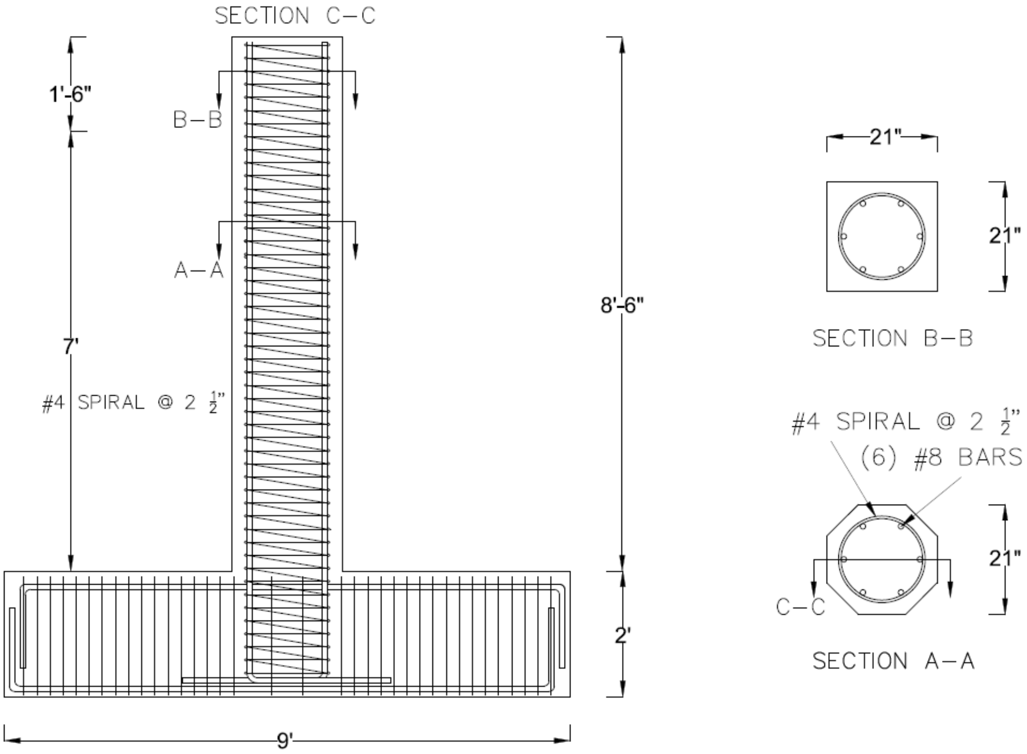

(a) Details of FGSS-CIP.

(b) Rebar cage ready to cast concrete.

Figure 2.33 FGSS-CIP specimen detail and rebar cage.

Figure 2.34 FGSS-CIP rebar cage inside form.

Figure 2.35 FGSS-CIP in final position.

3. TEST PROCEDURE

This section covers the required steps taken to develop the testing program and methods implemented to monitor the response and capture the test results. Details of the instrumentation types and locations are included, along with a description of the test setup and lateral displacement history applied to the specimens.

3.1 Instrumentation

Various types of instrumentation were used to obtain the test results and help understand the overall performance. This section includes discussions on the application of strain gauges, string potentiometers, and linear variable differential transformers (LVDT).

3.1.1 Strain Gauges

Test specimens were instrumented with several strain gauges, especially in the plastic hinge region and the joint area where maximum demand was anticipated to occur. These gauges were installed on longitudinal and transverse reinforcement to capture the strain levels during the test. For the precast concrete test models, strain gauges were placed on the GSS connector in the middle section to obtain the induced strain measurements on the sleeves.

Strain gauges were mostly attached to the two longitudinal bars located farthest from the centerline of the column to characterize the maximum strain conditions. In most of the tests, strain gauges were also applied to such bars for the portion grouted inside the GSS connector at a section located 2 in. from the GSS connector ends. The objective was to determine when these bars would yield.

A sample of a typical strain gauge layout is shown in Figure 3.1. This layout includes the location, designation, and type of strain gauge used at each specific section. Only the two farthest longitudinal reinforcing bars were gauged in each section, and only two strain gauges were placed on the corresponding spiral section for specimen GGSS-1.

A detailed step-by-step procedure was followed for surface preparation, attachment of strain gauges, and protection from debris and other damage that was likely to be caused by the surrounding concrete. Figure 3.2 displays the strain gauges placed on the spiral and longitudinal rebar during the last phase of construction for specimen GGSS-3. Wires were carefully routed towards a point in the middle of the cap beam or footing where significant damage was unlikely to occur. Strain gauge wires were protected inside the hollow flexible plastic tubes.

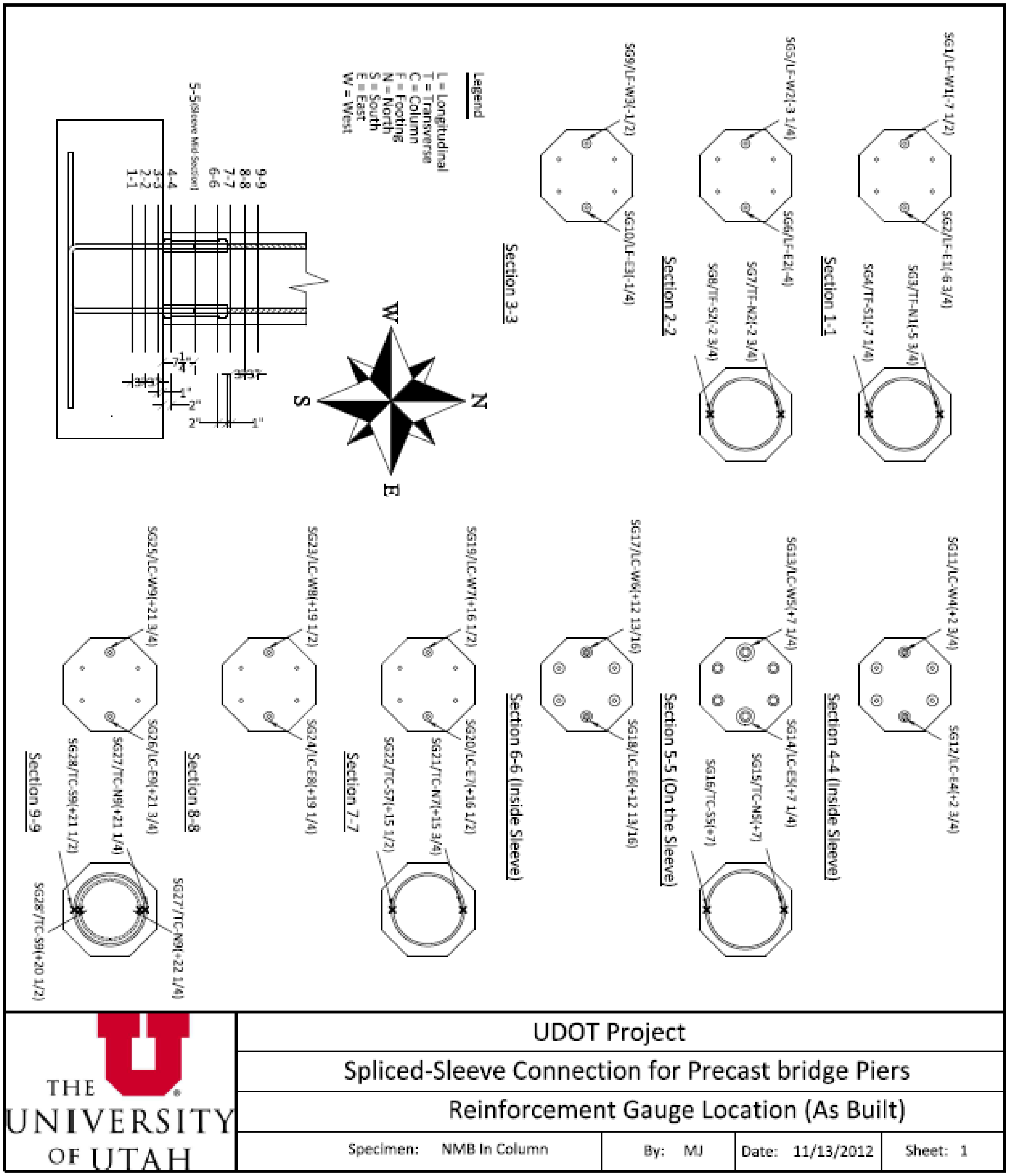

Figure 3.1 Strain gauge layout for GGSS-1.

Figure 3.2 Strain gauges on GGSS-3.

3.1.2 String Potentiometers

Two string potentiometers were used to measure column displacement during the test. They were both attached to the column head at an elevation equal to the height of the center of the actuator. The two string potentiometers were oriented in the opposite direction. Column displacements were obtained by taking the average of the readings collected from these two potentiometers. Force-displacement plots were constructed utilizing the results from this instrumentation. Readings from the string potentiometers provided information for further analysis, such as energy dissipation capacity. Figure 3.3 shows the west string potentiometer installed on specimen GGSS-3.

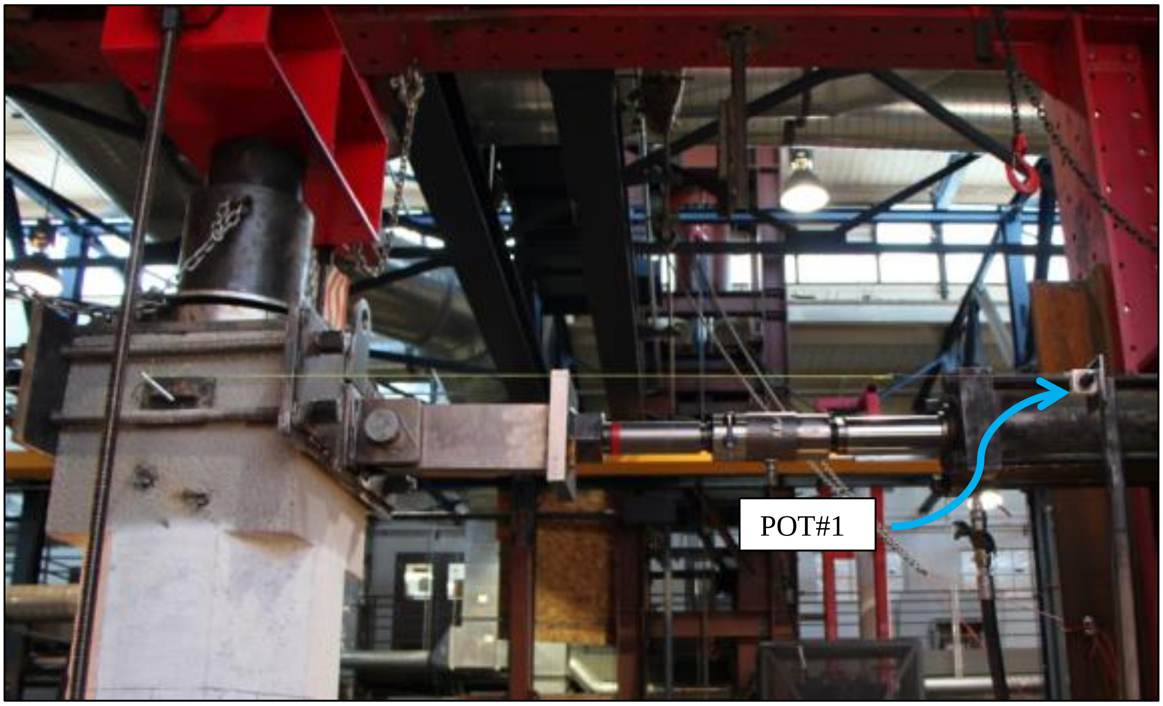

Figure 3.3 String potentiometer on west side of specimen GGSS-3.

3.1.3 Linear Variable Differential Transformers

Linear variable differential transformers (LVDTs) were used to study the curvature distribution along the column end, obtain the base rotation capacity, characterize bond-slip rotation, and verify the global vertical and horizontal movements of the specimens.

Ten LVDTs were mounted to the column end, over a 30-in. region, to measure the relative vertical displacements between the sections and provide data for curvature analysis. Column base rotation and subsequent bond-slip rotation were studied using the lowest pair of LVDTs at the column end, or LVDT 1 and 2 as illustrated in Figure 3.4, for the column-to-footing connections. Other LVDTs were used to compute the curvature capacity along the column end. The LVDT configuration was similar for the column-to-cap beam connections. Using 1½-in. steel angles and spherical rod ends, these LVDTs were fastened to 3/8-in. diameter all-thread rods, which were embedded in the column core. Figure 3.5(a) shows the all-thread rods attached to the column cage, while Figure 3.5(b) displays the LVDTs mounted on the column end before the test. Four sets of LVDTs were used to create four curvature segments over which curvature was assumed to be constant. The segment height was specified to be 6 in. for the bottom two curvature segments and 8 in. for the top two curvature segments. This was determined in accordance with the stroke capacity of the LVDTs along with the predicted curvature demands in the particular segment. A preliminary sectional analysis had been conducted to estimate the ultimate curvature capacity of the critical section for a monolithic connection, as discussed in Section 2.1. The predicted ultimate curvature was then converted into a predicted ultimate strain in the critical column segment. The maximum LVDT stroke along with a proper segment height resulted in the selection of the desired LVDT configuration for all curvature segments. LVDTs 11 and 12 in Figure 3.4 were only used to verify the test setup and ensure that the test specimen would not undergo unexpected global slippage in the vertical or horizontal direction.

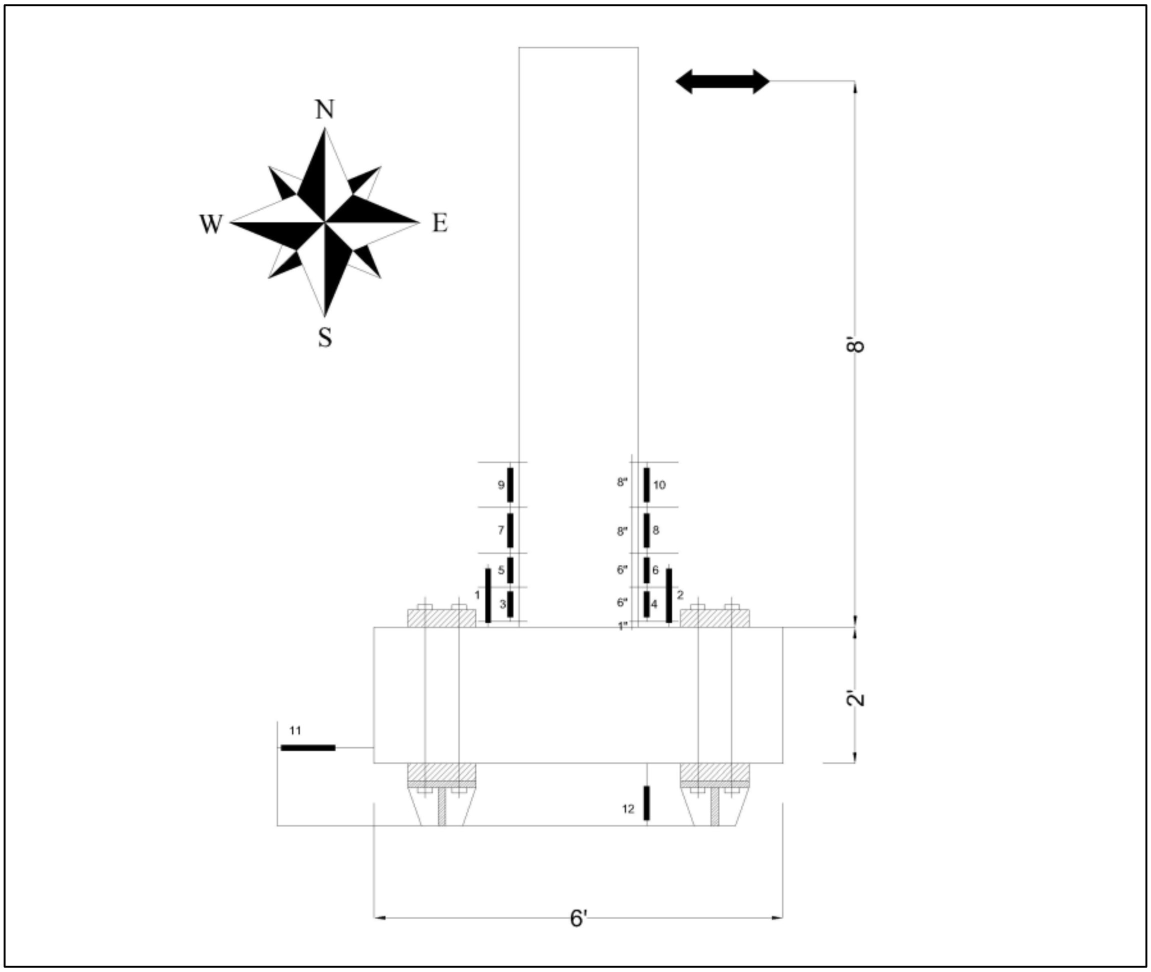

Figure 3.4 LVDT configuration for column-to-footing connections

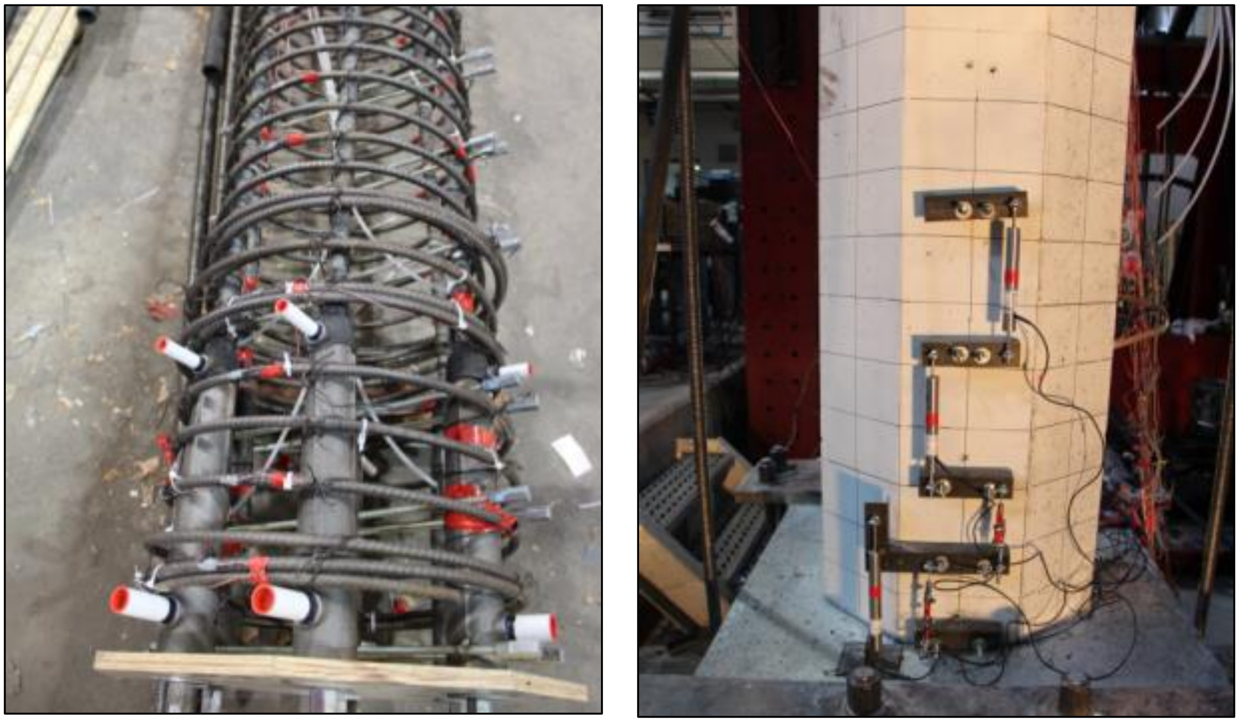

(a) LVDT all-thread rods attached to rebar cage (b) LVDTs attached to fixture.

Figure 3.5 LVDTs for curvature analysis.

3.2 Test Setup

All specimens were tested inside the test frame of the Civil and Environmental Engineering Department Structures Laboratory at the University of Utah. This test frame has a capacity to resist 500 kip in any of three directions. The column-to-cap beam joints were tested in an inverted condition. Each specimen was connected to the floor girders by means of eight high-strength all-thread rods on each side, half of which ran through the PVC pipes embedded in the footing (or cap beam), before casting the concrete. The rods were then bolted to 1½-in. top and bottom plates to prevent the specimen from moving or slipping during the test. This support condition was designed to provide very limited rotational restraint, and hence represents a hinged support condition.

The axial load application system consisted of a cylindrical 500-kip hydraulic actuator, a 4-ft. long stiffened W14x90 spreader beam, a 3-in. thick A36 steel plate, and two 14 ft.-6 in. long, 150 ksi, 1-in. diameter all-thread rods. The 500-kip actuator was attached to the column top and applied a compression force to the steel beam above it, causing the all-thread rods to pull on the steel plate that was underneath the footing (or cap beam). An axial load equivalent to 6% of the column axial capacity was applied to simulate the gravity load typically present in a bridge column. Figures 3.6 and 3.7 include the schematic test setup in addition to the test frame configuration for column-to-footing and column-to-cap beam specimens, respectively.

A 120-kip servo-controlled actuator with an overall stroke of 18 in. applied a cyclic load to the precast test specimens; however, both control specimens were tested using a 250-kip servo-controlled actuator with an overall stroke of 24 in. The hydraulic actuators were powered by an MTS pump with a 3,000-psi work pressure and were used to apply a reversed cyclic quasi-static displacement history to the column as described in the next section.

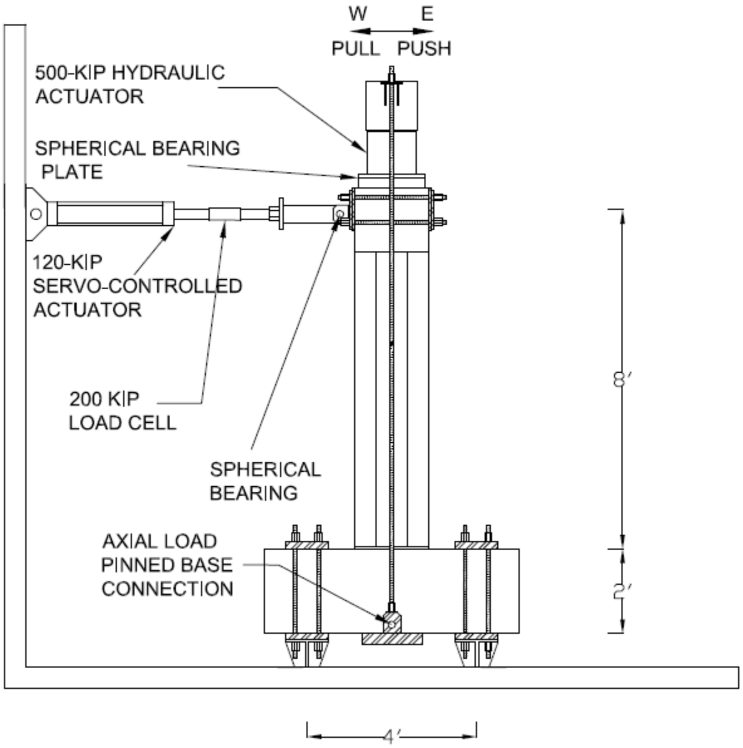

(a) Schematic test setup.

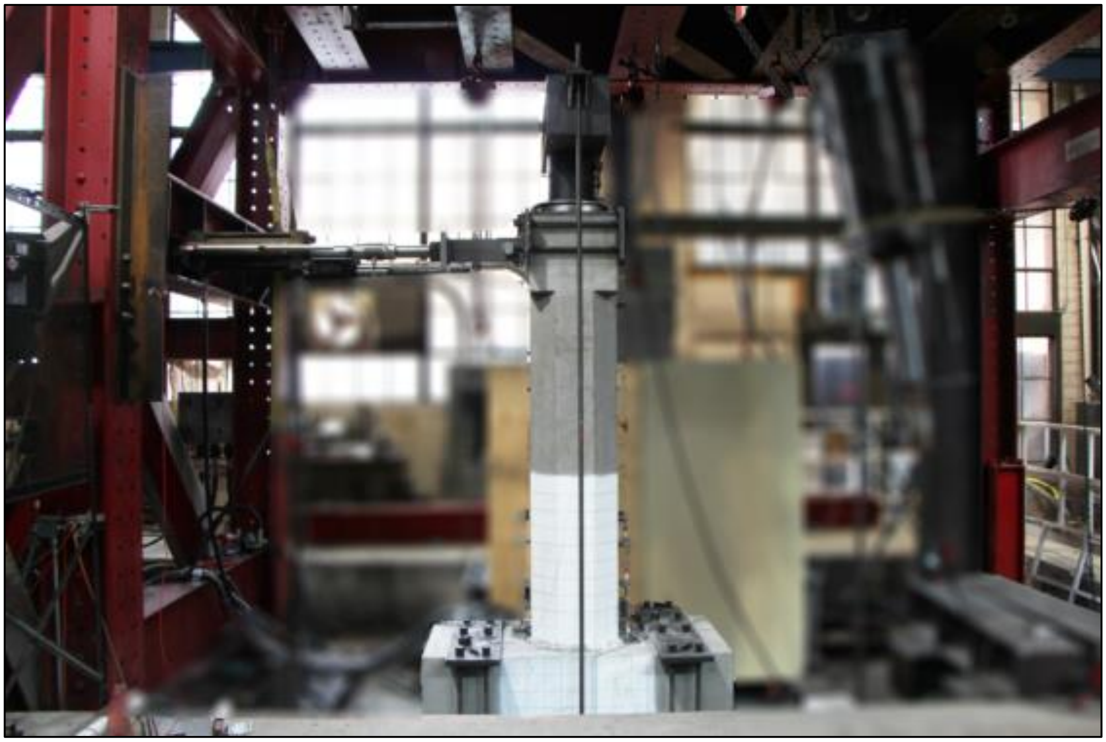

(b) Test setup.

Figure 3.6 Experimental configuration of column-to-footing specimens.

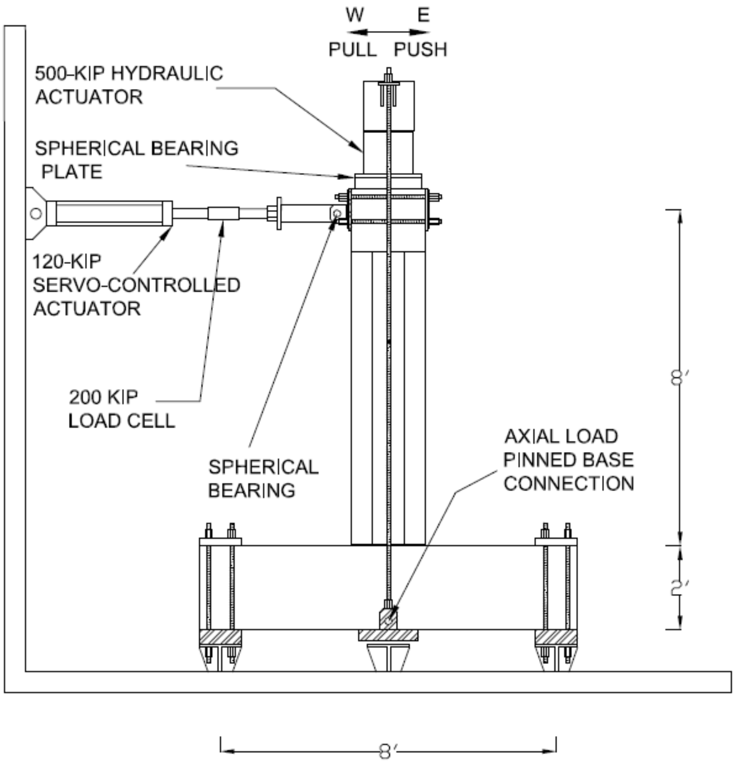

(a) Schematic test setup.

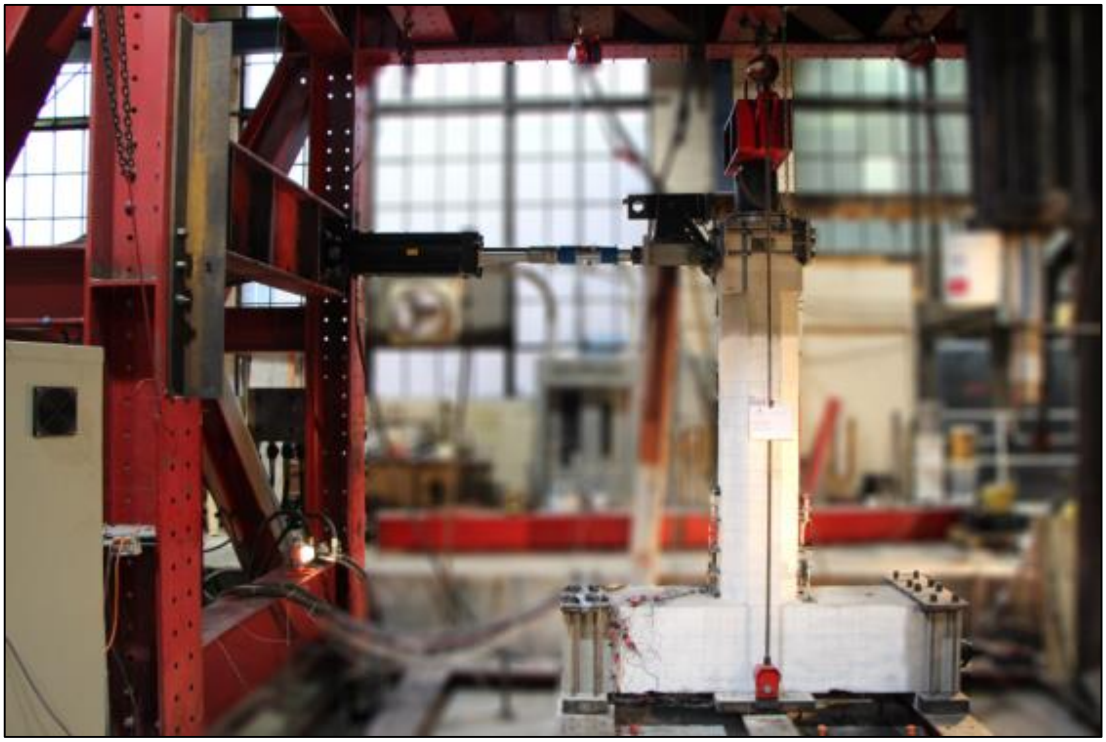

(b) Test setup.

Figure 3.7 Experimental configuration of column-to-cap beam specimens.

3.3 Displacement History

A cyclic quasi-static loading protocol using displacement control was applied to the column at an elevation 8 ft. above the footing or cap beam, as shown in Figure 3.8. This displacement history was composed of increasing amplitudes as multiples of the predicted yield displacement of the column [20]. Two cycles were employed for each drift ratio as depicted in Figure 3.8. A five-minute pause was introduced after the completion of each drift ratio to examine the test specimen and make observations regarding the visible aspects of the response. The displacement rate was set to 1.2 in./min. up to the end of the 3-in. drift ratio, after which it was changed to 4 in./min. and was kept constant until completion of the test.

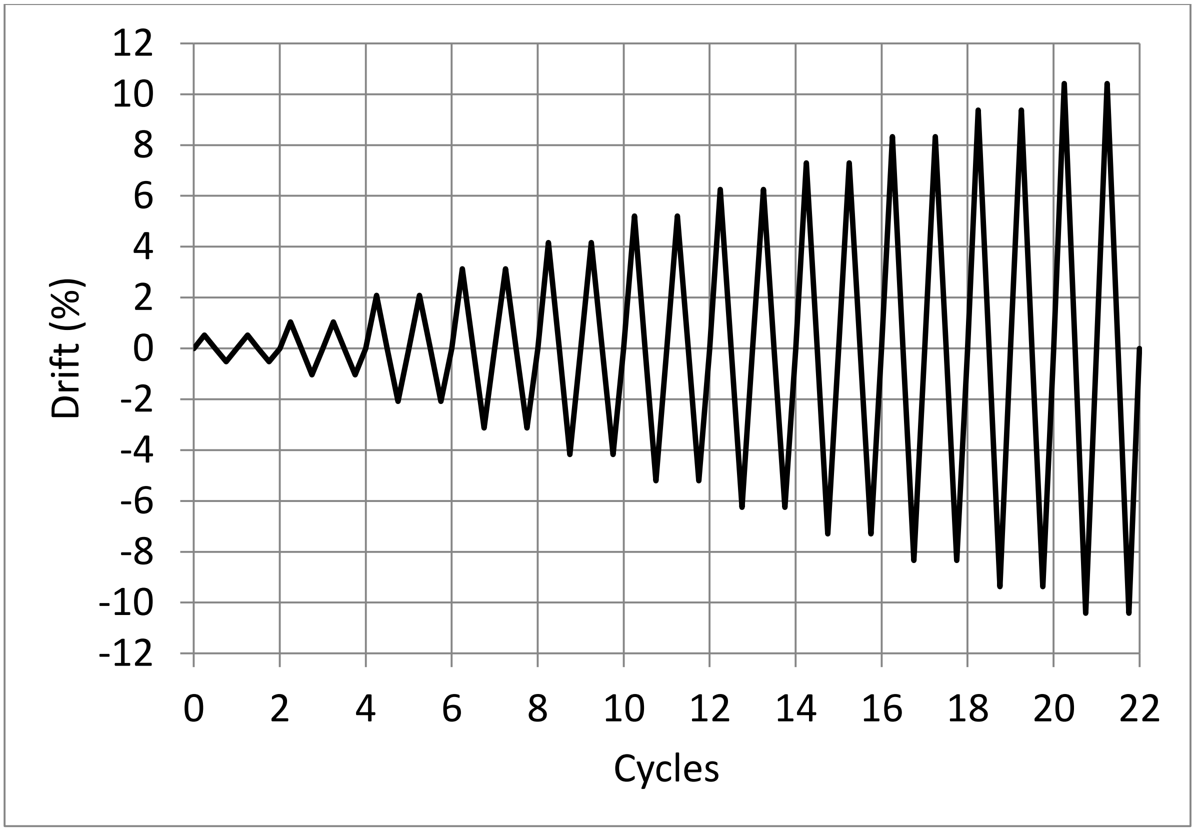

Figure 3.8 Displacement history.

4. TEST RESULTS

The measured response of the specimens under the applied lateral displacement history is discussed in this section. Analysis of the measured response of individual tests includes discussions on the visual aspects of the performance, hysteretic behavior, displacement ductility of each specimen, along with a discussion of plastic rotation capacity, energy dissipation capacity, and, lastly, distribution of curvature along the column. A comparative study is undertaken for each connection category to provide a better assessment of the performance relative to the control specimens. The comparison includes the lateral force-displacement response, energy dissipation capacity in terms of equivalent viscous damping, cyclic degradation of stiffness, and investigation of the curvature distribution for all specimens.

4.1 Analysis of the Response

This section describes the four evaluation methods implemented for each specimen.

4.1.1 Experimental Observations and Damage States

This section summarizes the visual observations made during the tests with respect to damage progression, including formation and development of cracks and spalling of concrete. There is discussion of the overall performance of the specimens recorded during the test and captured in photographs, such as onset of rebar buckling and fracture or excessive slippage of the spliced bar. Termination of the experiment and failure mode of each test specimen is investigated using the hysteresis response for each test. Damage states shown on the hysteresis response graph indicate significant stages of performance. The quality of hysteresis loops along with strength and stiffness degradation are also noted. Select photographs of the specimen are provided to present the state of damage at particular drift ratios. All specimens were painted white, and grid lines divided the concrete surface into 4-in. squares. Different color markers were used to mark concrete cracks with a displacement level index to identify the crack formation sequence.

4.1.2 Displacement Ductility Capacity and Plastic Rotation Capacity

Displacement ductility capacity is considered as the ability of a structural component to perform beyond the yield point without excessive strength deterioration. This parameter was computed for each test specimen based on the concept of equal energy of an idealized elasto-plastic system [21]. The average backbone curve was first constructed using the peak values of the first cycle for each drift ratio. The idealized elasto-plastic curve was then generated in order to calculate the displacement ductility. To obtain the effective yield displacement of the system, it was assumed that the idealized elasto-plastic curve intersects the average backbone curve at a force equal to 70% of the effective yield force. This value was utilized in accordance with the recommendations of the ACI 374 *Guide for Testing Reinforced Concrete Structural Elements under Slowly Applied Simulated Seismic Loads* [20]. The ultimate displacement was taken as the displacement corresponding to a 20% drop in the lateral load capacity [22]. Displacement ductility was then obtained as the ratio of the ultimate displacement to the yield displacement of the system.

The rotation capacity of each test specimen was assessed by dividing the column-top displacement by the overall height of the column. The plastic rotation was obtained and presented in bending moment-rotation plots for each test specimen. This could help identify the rotational characteristics of the test alternatives with respect to the control specimens. Equations (2) and (3) contain the parameters required for such an analysis, as follows:

$$\theta_p = \frac{\Delta_p}{H} \tag{2}$$

$$\Delta_p = \Delta - \Delta_y \tag{3}$$

where, θ_p and Δ_p are the plastic rotation and plastic displacement, respectively, H is the overall column height, Δ is the column-top displacement at the actuator level, and Δ_y is the yield displacement.

4.1.3 Cumulative Energy Dissipation

One of the main features of bridge ductile elements in high seismic regions is their ability to dissipate energy through inelastic deformations. This is an indication of the quality of the hysteretic response. The presence of mild steel in the plastic hinge region capable of undergoing inelastic behavior is significant for achieving the required amount of energy dissipation. The area enclosed by the hysteresis loops is referred to as the hysteretic energy of a system. This was computed cumulatively for each test specimen to obtain the energy dissipation capacity at any desired time step for comparative studies.

4.1.4 Column Curvature Profile

LVDTs installed on both extreme sides of the column base were used to study the curvature distribution and curvature capacity of the specimens. Therefore, four curvature segments were specified by using four LVDTs on each side of the column. The average curvature was computed as shown in Equation (4):

$$\phi = \frac{A - B}{wh} \tag{4}$$

where A and B are LVDT readings, and w and h are the segment width and height, respectively. These parameters are shown in Figure 4.1 for the first curvature segment in the column base. The average curvature profile was constructed over a 30-in. column height above the column base. The average curvature values were normalized by multiplying them by the column dimension of 21 in., and the curvature segment heights were divided by the column overall height of 96 in. Positive curvature values were associated with the push direction and negative values with the pull direction. The calculated curvature value was assumed to be an average over the whole segment height. Curvature values are included up to a 6% drift ratio, which was the last common drift ratio among all specimens. Dashed lines in the plots mark the top of the GSS connectors in the column base for precast specimens with GSS connectors inside the column.

According to the data collected from strain gauges on the column longitudinal bars and footing or cap beam dowels, the yielding pattern for both extreme bars was studied. This provides information for regions within each specimen with extreme bars in the inelastic range.

4.2 Response of Column-to-Footing Joints

The response of the column-to-footing joints is presented in this section. The four evaluation methods described in Section 4.1 are utilized to study the results from each test. A comparative study is also presented at the end of this section, emphasizing the similarities and differences between the cast-in-place GGSS-CIP and the precast GGSS-1 and GGSS-2.

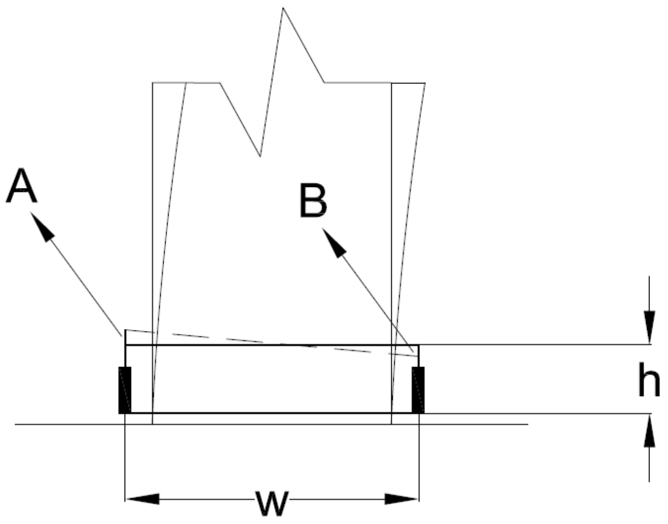

Figure 4.1 Curvature parameters for one curvature segment.

4.2.1 GGSS-1 Results

4.2.1.1 Experimental Observations and Damage States

Figure 4.2 shows the lateral force-displacement curve in addition to the major damage states, including end of crack formation and initiation of spalling, yield penetration, and rebar fracture. Hysteresis loops were wide and stable for this specimen without strength degradation up to a 7% drift ratio. A slight reduction in strength is noted at the 8% drift ratio. The test was terminated at the end of the 9% drift ratio due to a drop larger than 20% in lateral force. The overall hysteresis response was symmetric in terms of strength and residual drift.

A minor hairline crack developed at the bed grout, located at the column-to-footing interface, during the 0.5% drift ratio. This crack became wider and was accompanied by another crack forming right above the GGSS connectors during the first cycle of the 1% drift ratio. By the end of the 3% drift ratio, all major cracks had developed, including a relatively large crack at the bed grout, another one at a section close to the top of the GGSS connectors, and a third crack at the end of the spiral-overlapping zone about 30 in. above the column base, as shown in Figure 4.3(a). Spalling initiated during the first cycle at the 3% drift ratio and progressed near the corners of the octagonal column. The spalled area had a height of 4 in. on both sides of the column and a crack width of 0.009 in. above the GGSS connectors. Cracks widened and spalling progressed at higher drift ratios. The aforementioned select crack had a width of 0.013 in. at a drift ratio of 4%, 0.02 in. at a drift ratio of 5%, and 0.03 in. at the 6% drift ratio. Yield penetration was noted at the end of the 6% drift ratio with a depth of 1.5 in. on the west and 1 in. on the east side of the column, respectively. The height of the spalled region was 8 in. on the west and 14 in. on the east side of the column, respectively. Figure 4.3(b) shows the damage state at the end of the 6% drift ratio. The column spiral became visible during the 7% drift ratio, and a few hairline cracks were spotted on the north and south side of the footing. The bed grout deteriorated around the perimeter of the column end, while the spalled region over the GGSS connectors became deeper and these connectors were visible at the end of the 8% drift ratio.

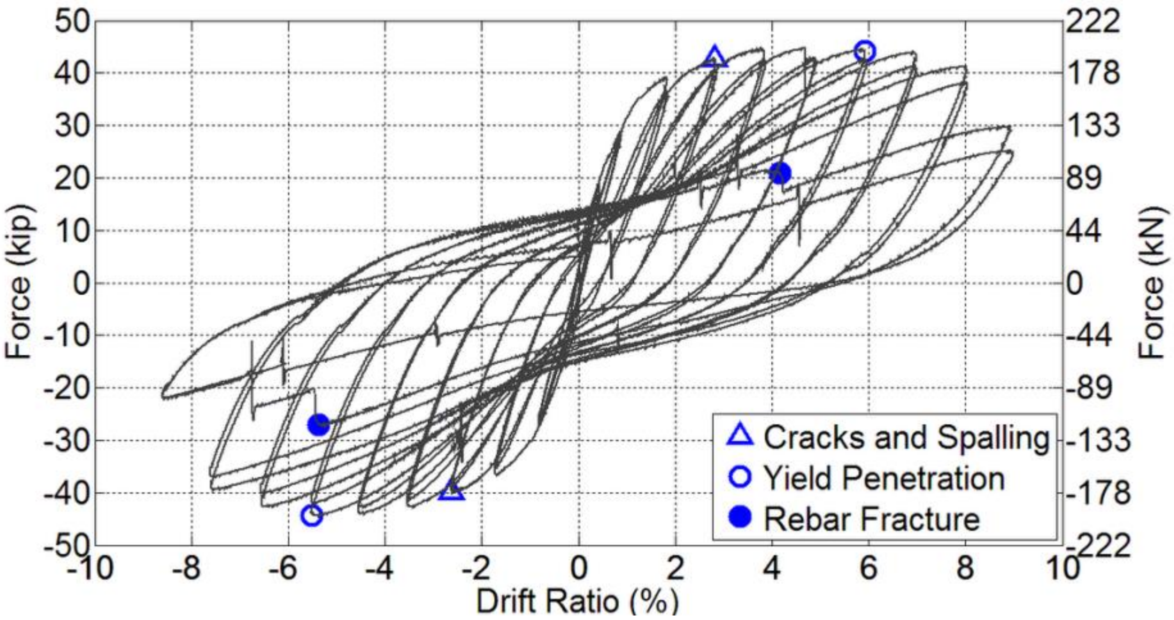

Figure 4.2 Hysteresis response of GGSS-1 with damage states.

During the last drift ratio of 9% for specimen GGSS-1, all six footing dowel bars had buckled. Concrete spalling grew larger in terms of area and depth, and the spiral and GGSS connectors were exposed, as shown in Figure 4.3(c). The two extreme bars fractured in the first cycle of the push and pull direction at the 9% drift ratio, due to low cycle fatigue. Rebar fracture occurred 1 in. to 1.5 in. below the surface of the footing, where there was no confining transverse reinforcement. Post-test investigations ascertained that the confined concrete core remained undamaged and the GGSS connectors themselves did not slip inside the column. The footing remained perfectly elastic as a capacity-protected member with minor hairline cracks in the joint region. Compression test results from concrete cylinders and grout cubes indicated that the concrete and grout compressive strength on the day of the test were 5.9 ksi and 14.4 ksi, respectively.

4.2.1.2 Displacement Ductility Capacity and Plastic Rotation Capacity

The average backbone curve was constructed in accordance with the method described in Section 4.1.2, along with the idealized elasto-plastic curve. Figure 4.4 depicts the two curves in addition to the parameters required to obtain the displacement ductility value. The effective yield displacement and force for specimen GGSS-1 were found to be 1.45 in. and 41.91 kip, respectively. The ultimate displacement, corresponding to a 20% strength drop was 7.79 in., resulting in a displacement ductility of 5.4.

Figure 4.5 displays the moment-plastic rotation relationship up to the test termination point. The plot shows that specimen GGSS-1 had a plastic rotation of 0.0630 rad, which occurred at the 8% drift ratio, before excessive strength reduction.

(a) Damage state at 3% drift ratio: cracks and spalling.

(b) Damage state at 6% drift ratio: cracks, spalling, and yield penetration.

(c) Damage state at 9% drift ratio: spalling, exposed rebar cage, and fractured bar.

Figure 4.3 GGSS-1 visual observations.

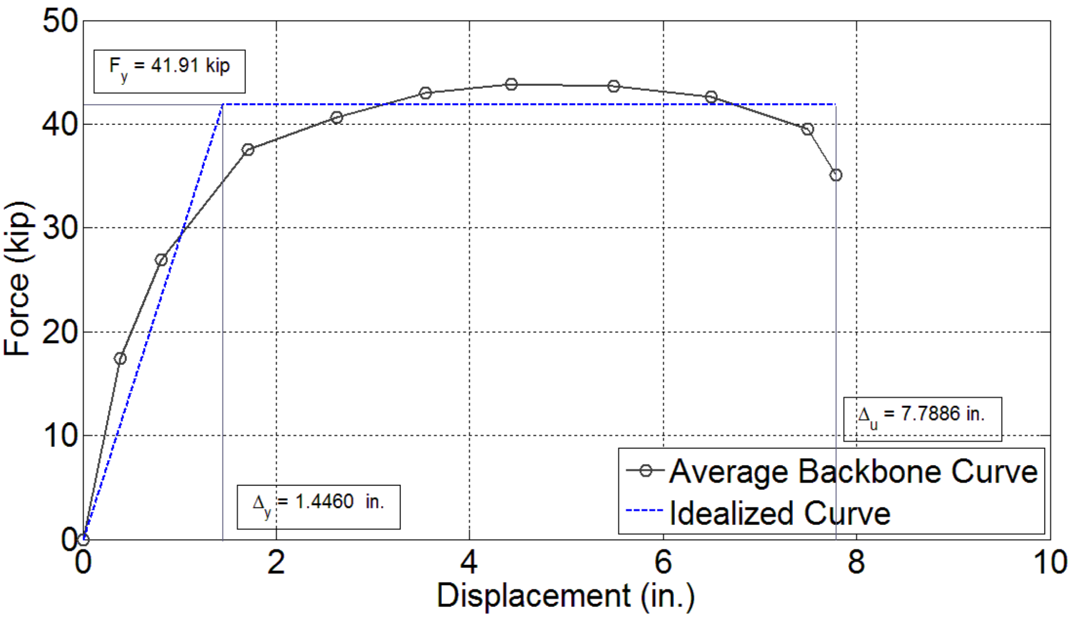

Figure 4.4 Average backbone curve and displacement ductility for GGSS-1.

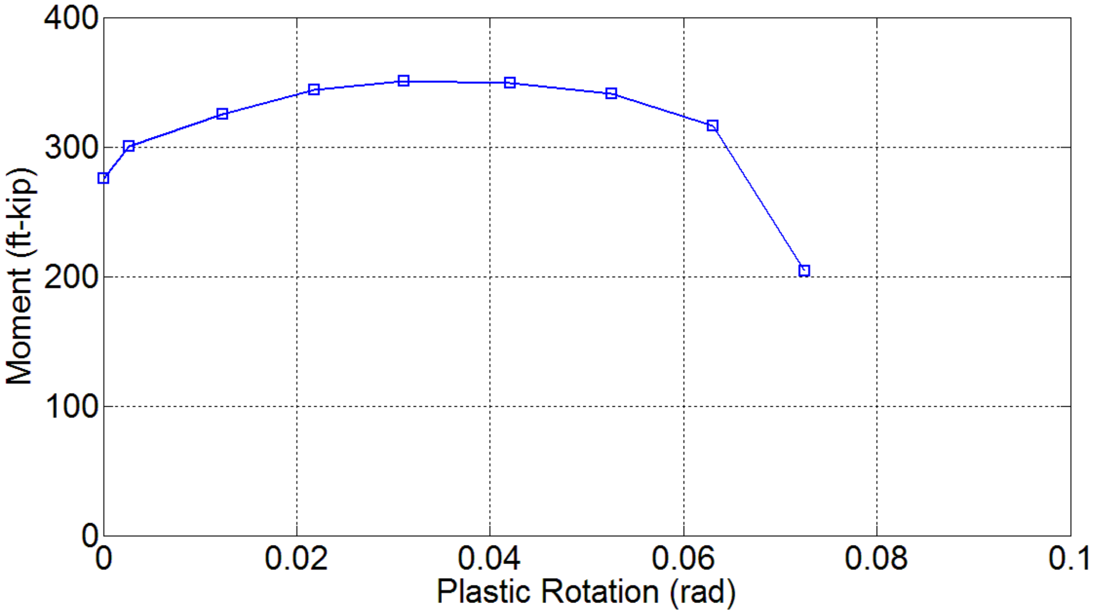

Figure 4.5 Plastic rotation capacity for GGSS-1.

4.2.1.3 Cumulative Energy Dissipation

The cumulative hysteretic energy is plotted against drift levels in Figure 4.6. It is noted that specimen GGSS-1 steadily dissipated energy with an increasing rate as it went through the inelastic portion of the response. During the 9% drift ratio, this rate decreased as a result of fracture of extreme column bars. The cumulative hysteretic energy was found to be 253 in-kip, 1487 in-kip, and 2522 in-kip at the 3%, 6%, and 9% drift ratios, respectively.

4.2.1.3 Column Curvature Profile

The GGSS-1 column curvature profile illustrated in Figure 4.7 indicates that bending action was more pronounced in the two sections below and above the GGSS connectors. This was attributed to the presence of the relatively more rigid GGSS connectors at the column base that resulted in considerably smaller curvature values along the height of the GGSS connectors. Lack of curvature above the GGSS region was because of a lower flexural demand around that elevation in the column.

Strain gauges located on the extreme longitudinal bars, at the column base, and within the joint core covered an area with a depth of 7½ in. into the footing and 21¾ in. up above the column base. These strain gauges showed that both extreme bars yielded over the whole range covered by strain gauges, except for the initial 5-in. portion of both the factory and field dowels, which were embedded and confined inside the GGSS connectors.

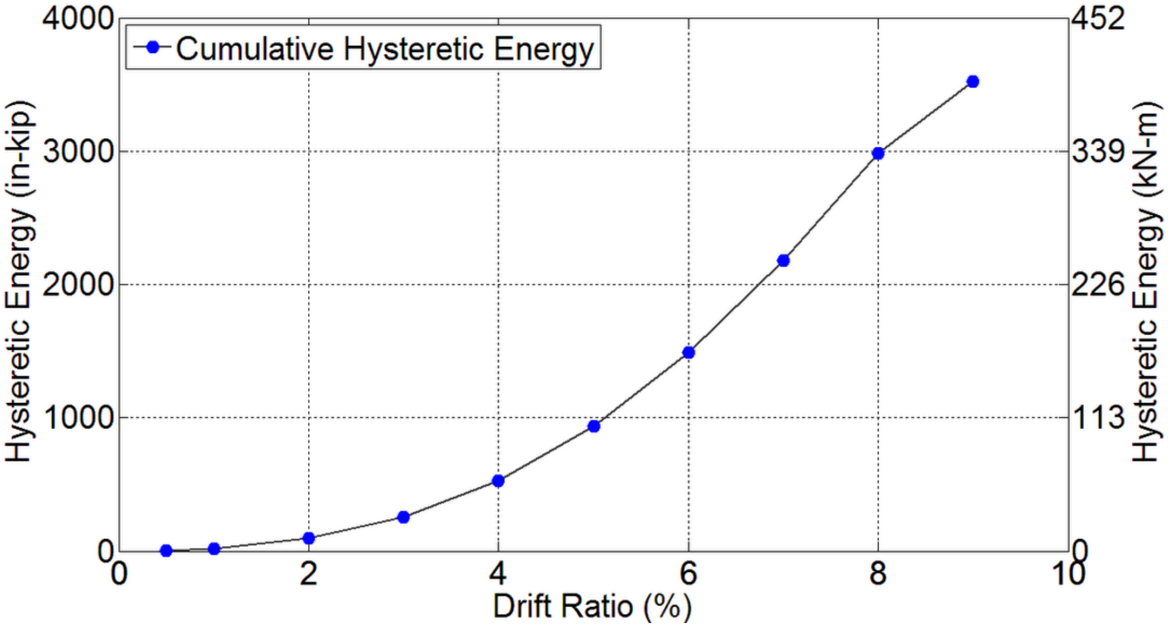

Figure 4.6 Energy dissipation capacity of GGSS-1.

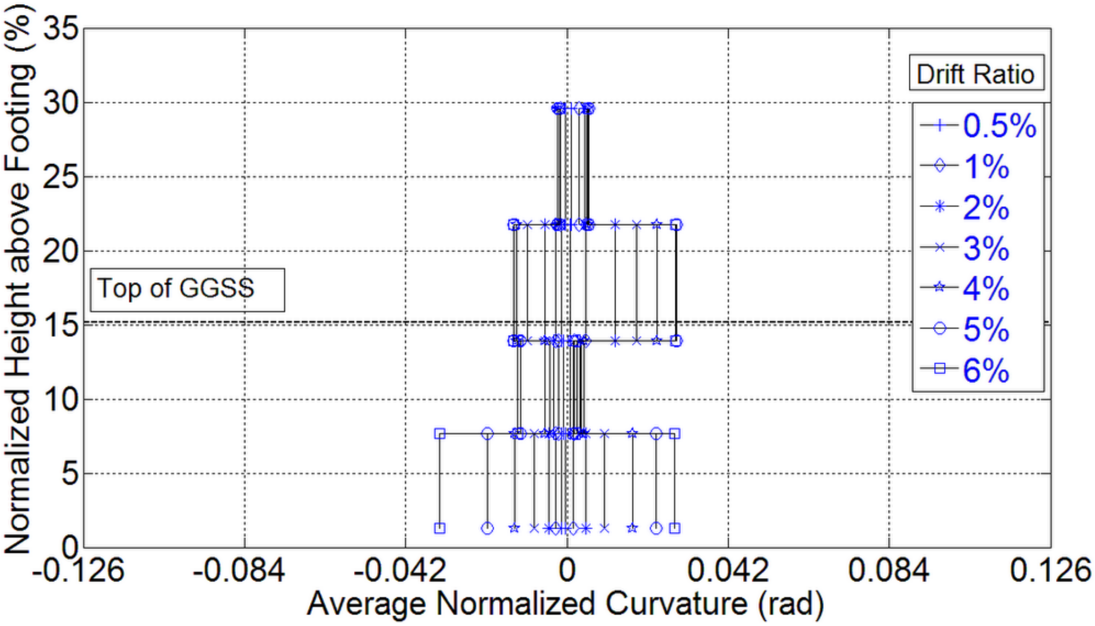

Figure 4.7 Normalized curvature distribution for GGSS-1.

4.2.2 GGSS-2 Results

4.2.2.1 Experimental Observations and Damage States

Figure 4.8 shows the hysteresis response of this specimen in addition to the major damage states, including end of crack formation and initiation of spalling and rebar fracture. Hysteresis loops were wide and stable for this specimen without strength degradation up to the 7% drift ratio, when the extreme east column bar fractured during the first pull cycle. The test was terminated at this point due to a drop larger than 20% of the lateral force. The overall hysteresis response was considered satisfactory, although there was a slight difference between the peak lateral forces in the push and pull directions.

Hairline flexural cracks developed at two elevations of 12 in. and 28 in. above the column end during the 0.5% drift ratio. These cracks widened during the next drift ratio followed by another crack that formed at the column-to-footing interface. By the end of the 3% drift ratio, a total of nine major flexural cracks had developed, including the two largest cracks that occurred at the bed grout and 6 in. above the column end. The width of the latter crack measured 0.03 in. on the east side of the column. The column of specimen GGSS-2 is shown in Figure 4.9 at maximum displacement during the 3% drift ratio along with the two cracks. The initiation of spalling at the southeast corner of the octagonal column is also visible with a vertical dimension of 4 in. The state of damage to the column plastic hinge region is shown in Figure 4.10(a) in addition to the spalled region and major flexural cracks that formed along the column height. It was noted that flexural cracks occurred at approximately 8-in. increments.

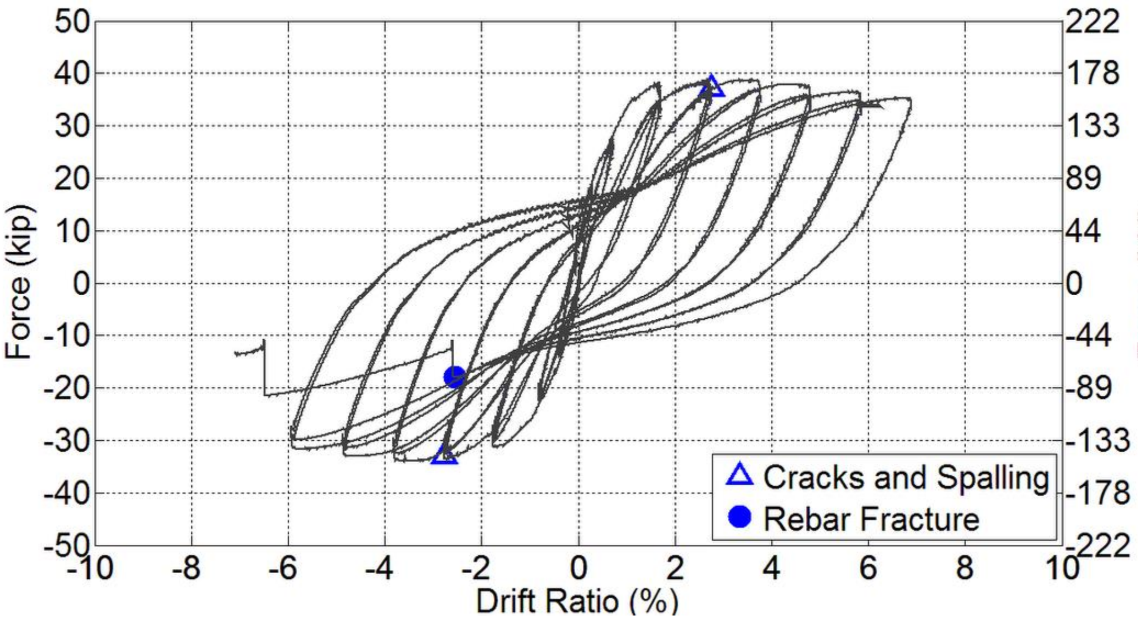

Figure 4.8 Hysteresis response of GGSS-2 with damage states.

The column plastic hinge region deteriorated with the increasing drift ratio. Cracks opened further and spalling intensified during the 4% drift ratio. The select crack located 6 in. above the column base had a width of 0.05 in. at the end of this drift ratio, and another crack at 10 in. from the column base had a width of 0.02 in. A few inclined cracks, known as flexure-shear cracks, developed during the 4% and 5% drift ratios on the north and south sides of the column base due to an increased tensile demand. A 7 in. piece of concrete cover split from the column base during the 5% drift ratio. Smaller concrete cover pieces, measuring 4 in. and 6 in., became separated from the surface of the column base during the 6% drift ratio.

During the first pull of the 7% drift ratio, the extreme column reinforcing bar fractured at a section 2 in. above the interface, and the test was terminated as the column strength dropped below 80% of the maximum reached. Fracture of the rebar was attributed to low cycle fatigue as a result of successive bending and re-straightening of the extreme reinforcing column bar. A post-test investigation revealed that the cover concrete was crushed completely around the column end after removing the loose material. Thus, spiral hoops, together with extreme column bars, were visible at the end of the test.

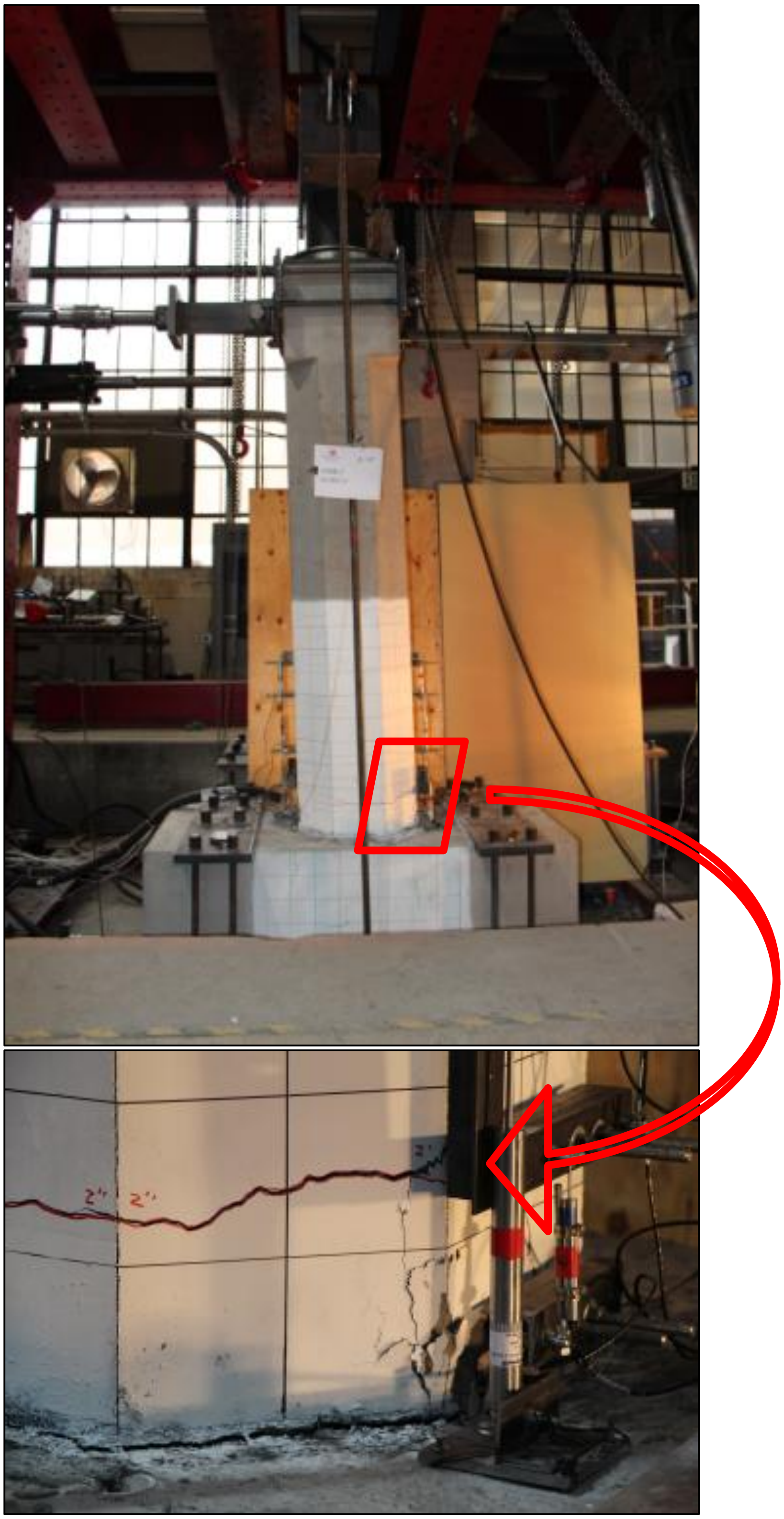

Figure 4.9 GGSS-2 at maximum displacement during the 3% drift ratio—largest crack.

The crack, which had developed at the column-to-footing interface during the previous drift ratios, became a 0.0625-in. permanent gap when the test was terminated. Figure 4.10(b) depicts the damaged area at the column base, including major cracks, spalled region, and the fractured column bar.

The footing remained intact with only a few scattered minor cracks below the interface in the joint region. The test-day compressive strength of the concrete and grout was 5.5 ksi and 13.5 ksi, respectively.

(a) Damage state at 3% drift ratio: cracks and spalling.

(b) Damage state at 7% drift ratio: cracks, spalling, fractured bar, and exposed rebar cage.

Figure 4.10 GGSS-2 visual observations.

4.2.2.2 Displacement Ductility Capacity and Plastic Rotation Capacity

A displacement ductility of 6.1 was obtained for this test specimen using the standard procedure described in Section 0 and as shown in Figure 4.11. The idealized curve was constructed to determine all parameters required to compute the displacement ductility capacity. The ultimate displacement of 6.42 in. was associated with a 20% drop in the lateral force. Effective yield strength and yield displacement were obtained as 32.63 kip and 1.05 in., respectively.

Figure displays the moment-plastic rotation relationship up to the test termination point. The plot shows that GGSS-2 had a plastic rotation of 0.0478 rad, which occurred at the 6% drift ratio, without a considerable reduction in the bending moment capacity.

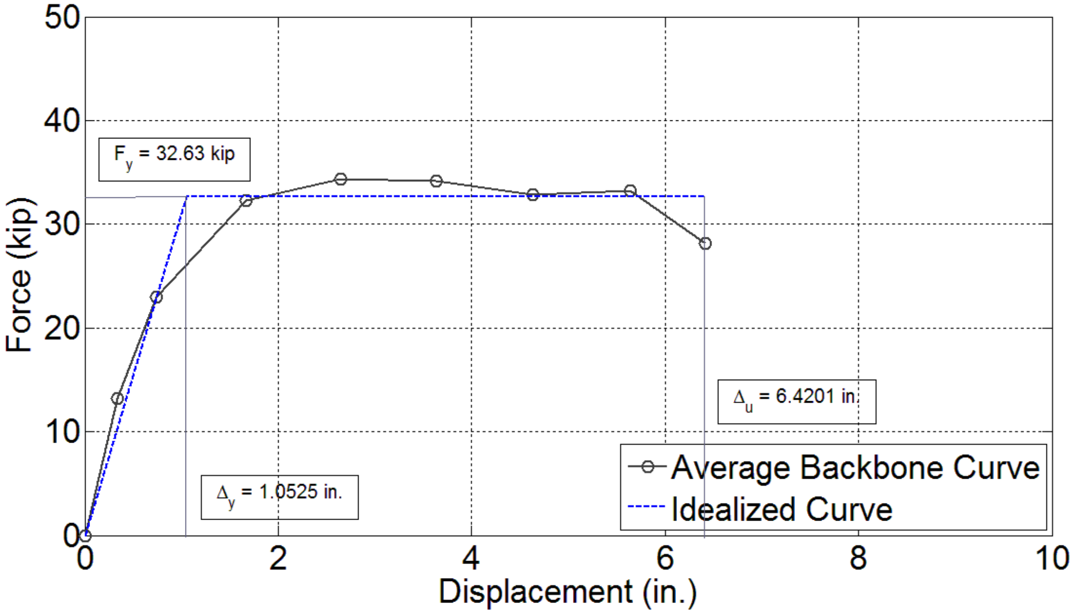

Figure 4.11 Average backbone curve and displacement ductility of GGSS-2.

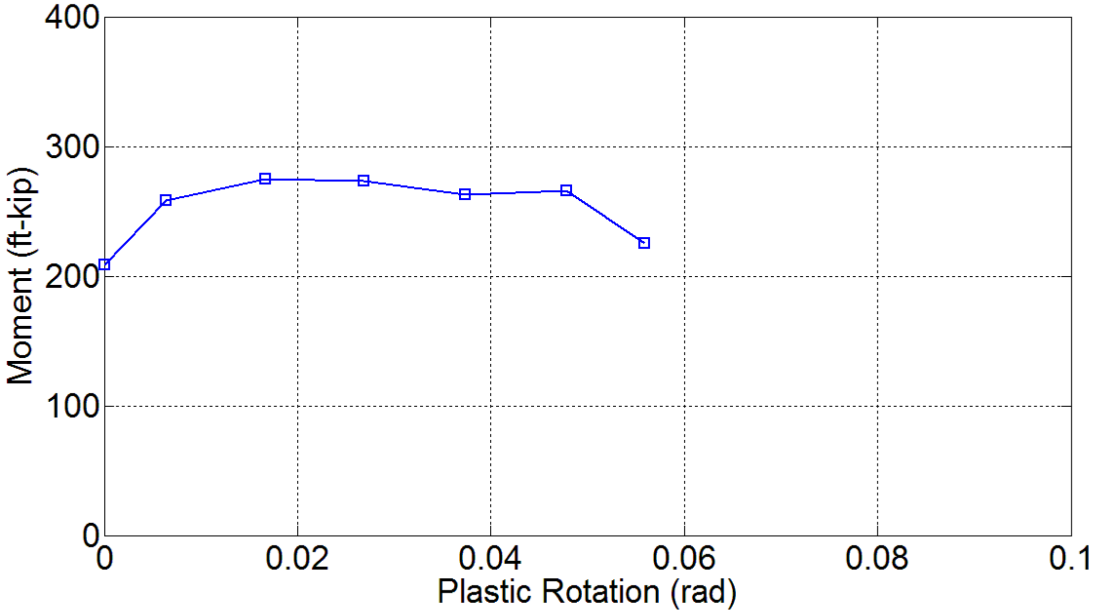

Figure 4.12 Plastic rotation capacity for GGSS-2.

4.2.2.3 Cumulative Energy Dissipation

Figure 4.13 shows the cumulative hysteretic energy per drift ratio. It was observed that specimen GGSS-2 steadily dissipated energy with an increasing rate, except for the last drift ratio in which the east column rebar fractured in the first pull cycle. This property of specimen GGSS-2, along with other pertinent response characteristics, will be utilized to ascertain a comparative evaluation of the overall performance with respect to other specimens in this category. The cumulative hysteretic energy was 270 in-kip at a 3% drift ratio, and 1563 in-kip at a 6% drift ratio.

4.2.2.4 Column Curvature Profile

The GGSS-2 column curvature profile is shown in Figure 4.14. A well-distributed curvature profile was achieved for this specimen as there were no GGSS connectors in the column base to introduce disruption to the regular flow of stresses from column to footing. Curvature values were highest along the first curvature segment located closest to the column-to-footing interface, and lowest along the last curvature segment located at the uppermost region of the column base. Curvature demand gradually decreased with an increase in distance from the interface. This was a desirable distribution of inelasticity along the plastic hinge region of the column.

Strain gauges located on the extreme longitudinal bars, in the column base and within the joint core, covered an area with a depth of 16 in. into the footing and 20 in. up above the column base. These strain gauges showed that the extreme column dowels yielded starting at 5 in. from the tip of the column dowel bars, which were confined within the GGSS connectors, or in other words, 2 in. into the footing from the column-to-footing interface. On the contrary, the footing dowel bars did not perform inelastically and strain values remained below the rebar yield strain.

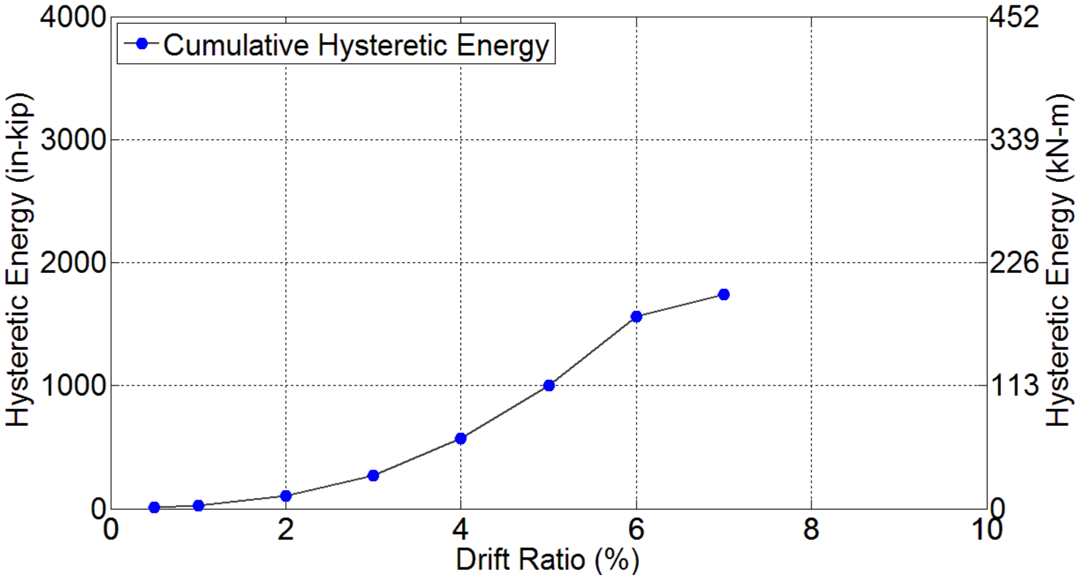

Figure 4.13 Energy dissipation capacity of GGSS-2.

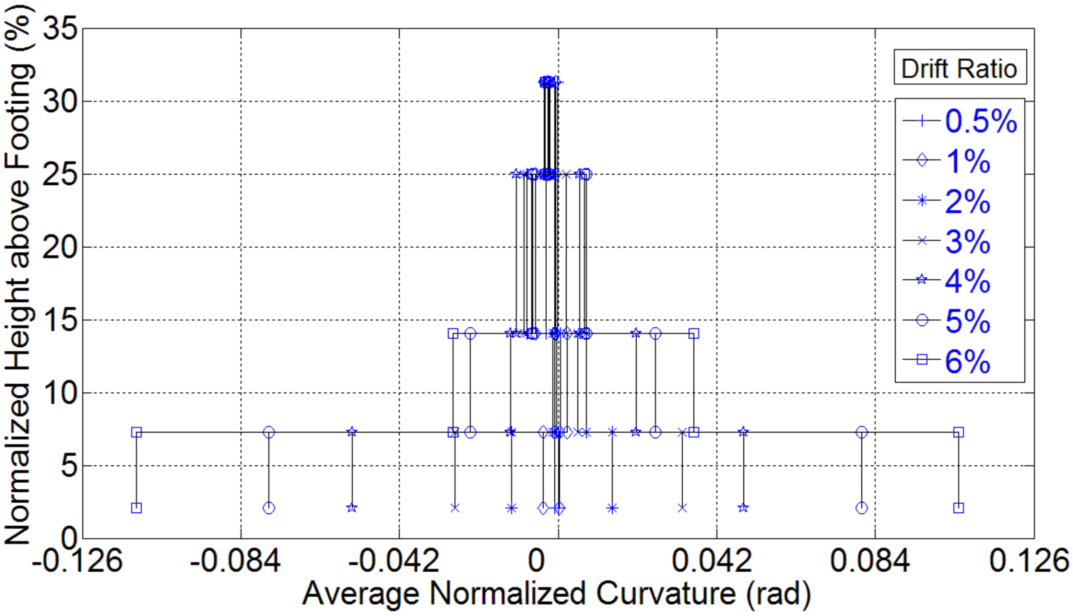

Figure 4.14 Normalized curvature distribution for GGSS-2.

4.2.3 GGSS-CIP Results

4.2.3.1 Experimental Observations and Damage States

The hysteretic response of this test specimen is presented in Figure 4.15, with the damage states corresponding to: (1) end of major crack formation and beginning of spalling, (2) yield penetration, and (3) rebar fracture. The overall response was very good as a result of the wide and stable hysteresis loops that imply high energy dissipation capacity. The lateral load peaked at 35.95 kip during the 2% drift ratio and at 37.07 kip during the 4% drift ratio for the push and pull direction, respectively. A slight strength softening was evident, especially for the push direction. This was attributed to deterioration of the concrete cover, which was relatively larger than the corresponding precast test specimens. The thicker concrete cover was provided to keep the column effective depth identical for all test specimens.

The column west rebar fractured at the end of the second push during the 8% drift ratio, and the east bar fractured during the first pull of the 9% drift ratio, by the end of which the test was terminated. This test specimen had a remaining 60% strength capacity, in both directions, at the end of the test.

By the end of the 0.5% drift ratio, two hairline flexural cracks formed at two sections located 12 in. and 32 in. above the column-to-footing interface. More flexural cracks developed during the 1% and and 2% drift ratios. The largest crack, which had developed 4 in. above the column base, had a width of 0.02 in. on the east side of the column during the 2% drift ratio. Concrete delamination initiated around the west and east sides of the column during the 1% drift ratio. This condition became more pronounced with increasing drift ratios. Spalling initiated at the column corners and a total of nine flexural cracks developed by the end of the 3% drift ratio. The select crack developed 4 in. above the column base had a width of 0.06 in. at the end of the 3% drift ratio. Another major crack that had formed 12 in. above the column base during the previous drift ratio widened and measured 0.007 in. Figure 4.16(a) displays the damage state at the end of the 3% drift ratio.

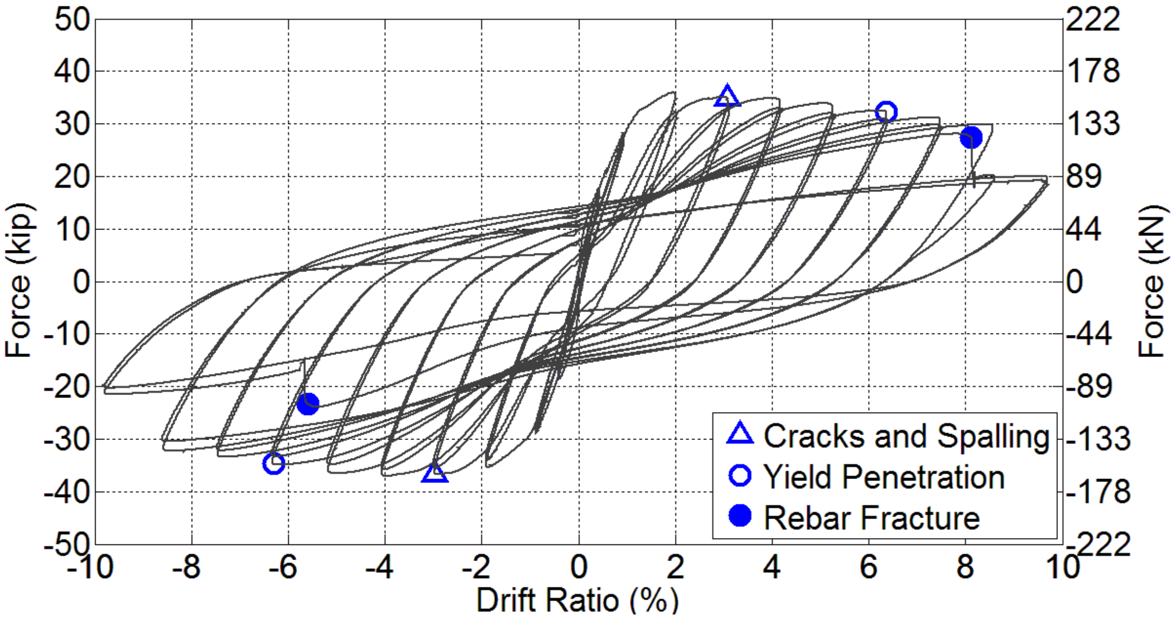

Figure 4.15 Hysteresis response of GGSS-CIP with damage states.

At the 4% drift ratio, spalling grew larger, especially at the column corners. A 12-in. high spalled area was evident on both sides of the column. The largest crack—formed at an elevation 4 in. above footing—closed back up and measured 0.025 in. The width of other representative cracks remained unchanged. During the 5% drift ratio, inclined or flexure-shear type cracks developed on the north and south sides of the column because of an increased tensile demand in the concrete.

At the 6% drift ratio, spalling became wider and spread to much of the column plastic hinge region; all major cracks were hidden within the spalled region, which made it difficult to make crack-width measurements. Yield penetration was also noted around the extreme two bars. Figure 4.16(b) shows the extent of damage to the column base, including major flexural and inclined cracks, and the spalled region.

During the 7% drift ratio, the spalled region became deeper in such a way that the spiral became partially visible. The extreme west column rebar fractured, as a result of low cycle fatigue, slightly before the peak displacement during the second push of the 8% drift ratio while the extreme east column bar was still undamaged but visible. This rebar broke during the first cycle of the 9% drift ratio due to low cycle fatigue caused by consecutive high-strain bending and re-straightening of the rebar.

Post-test investigations revealed that the west and east column bar fractured 1.5 in. and 2 in. above the footing. The footing concrete delamination had a depth of 1 in. on the west side. The spalled region in the plastic hinge region had a maximum width and effective height of 21 in. and 8 in., respectively. At the end of the test, column longitudinal rebar and spiral were visible at the column base, as shown in Figure 4.16(c).

The footing remained intact with only two minor cracks developing in the joint region during the 2% drift ratio. The test-day compressive strength of the concrete was 6.7 ksi.

(a) Damage state at 3% drift ratio: cracks and spalling.

(b) Damage state at 6% drift ratio: spalling and inclined cracks.

(c) Damage state at end of test: cracks, spalling, concrete delamination, and fractured rebar.

Figure 4.16 GGSS-CIP visual observations.

4.2.3.2 Displacement Ductility Capacity and Plastic Rotation Capacity

Following the procedure described earlier in this section, the average backbone curve and idealized curve were constructed to compute the displacement ductility capacity of specimen GGSS-CIP. The effective yield strength and yield displacement were obtained as 33.62 kip and 0.95 in., respectively. The ultimate displacement corresponding to a 20% reduction in the lateral force capacity was equal to 8.45 in. Consequently, the displacement ductility capacity of specimen GGSS-CIP was found to be 8.9. Figure 4.17 shows both the average backbone curve and idealized curve along with the relevant parameters.

Figure 4.18displays the moment-plastic rotation relationship up to test termination. The plot shows that GGSS-CIP had a plastic rotation of 0.0759 rad at the 8% drift ratio, prior to a considerable reduction in moment capacity.

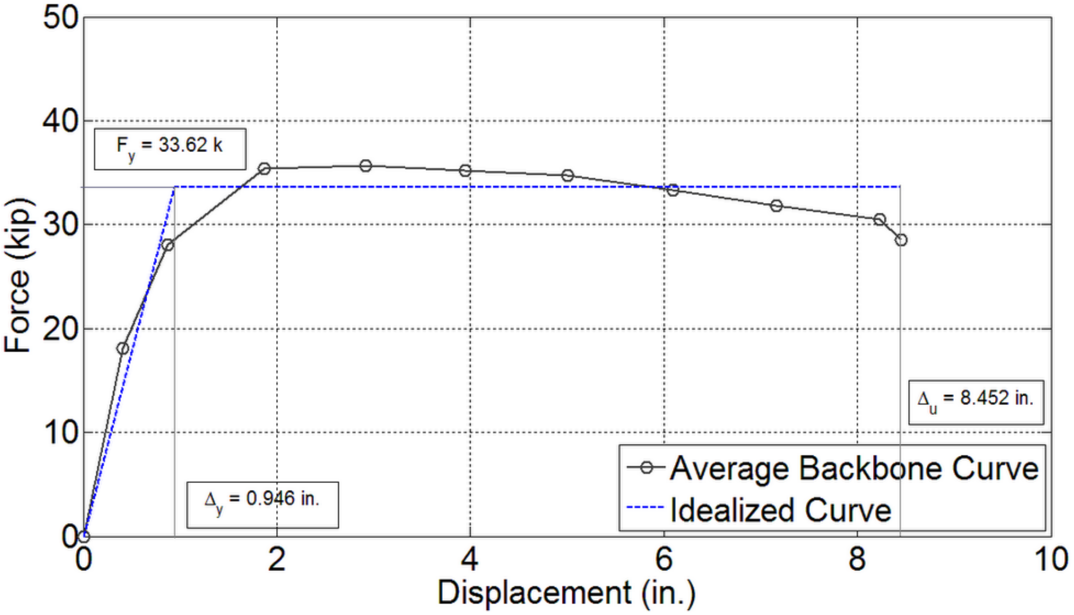

Figure 4.17 Average backbone curve and displacement ductility of GGSS-CIP.

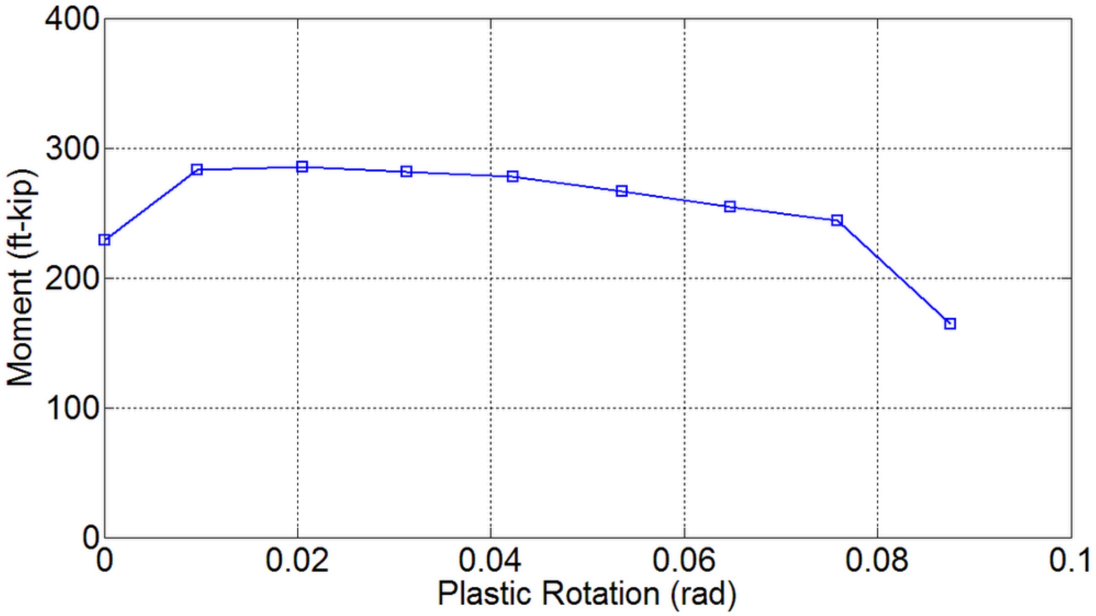

Figure 4.18 Plastic rotation capacity for GGSS-CIP.

4.2.3.3 Cumulative Energy Dissipation

The cumulative hysteretic energy is plotted against drift ratio in Figure 4.19. It was observed that the specimen dissipated energy at an increasing rate as it went through the inelastic portion of the response. The rate did not decrease during the 8% drift ratio even though a column rebar fractured. This was because the rebar fracture occurred when the column-top displacement was close to the peak, hence did not drastically affect the dissipated energy during the 8% drift ratio. However, this affected the hysteretic energy capacity of the 9% drift ratio as the lateral force capacity was reduced. Also, the fracture of the column east rebar during this drift ratio resulted in a decrease in energy dissipation. The cumulative hysteretic energy was 299 in-kip, 1657 in-kip, and 3906 in-kip at 3%, 6%, and 9% drift ratio, respectively.

4.2.3.4 Column Curvature Profile

The curvature profile for GGSS-CIP is shown in Figure 4.20. A well-distributed curvature profile was achieved for this specimen as expected for a reinforced concrete column with conventional cast-in-place details. Curvature values were highest along the first curvature segment located closest to the column-to-footing interface, and lowest along the last curvature segment located at the uppermost region of the column base. This was a desirable curvature distribution along the plastic hinge region of the column.

Strain gauges located on the extreme longitudinal bars, in the column base and within the joint core, covered an area with a depth of 9½ in. into the footing and 34 in. up above the column base. These strain gauges showed that both extreme column bars yielded within this instrumented region.

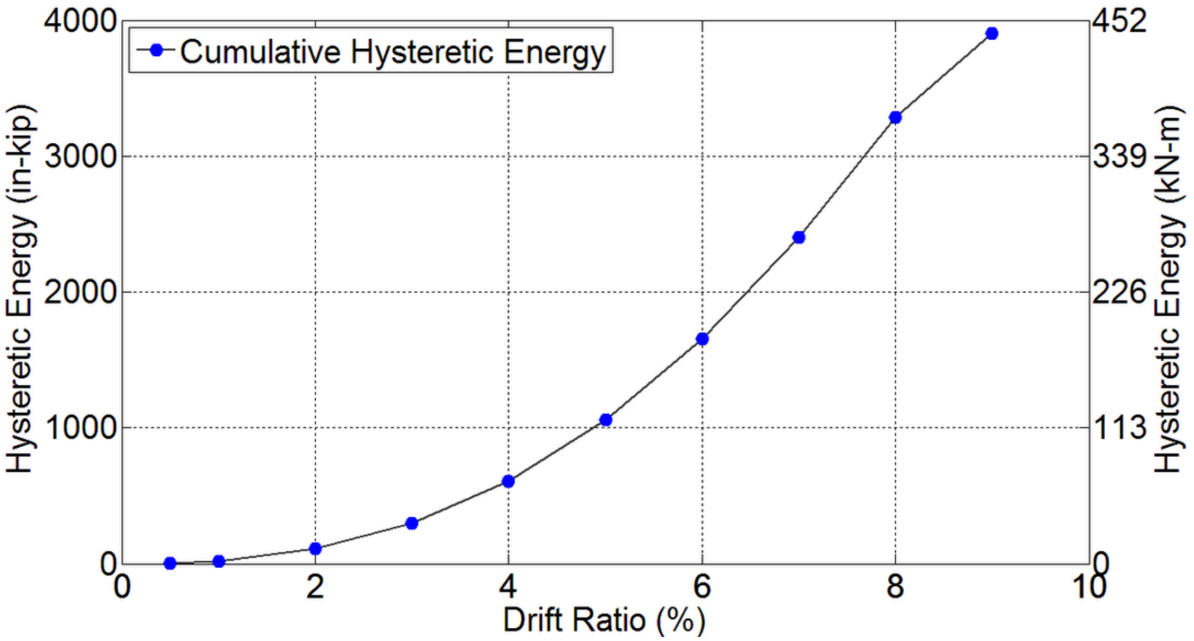

Figure 4.19 Energy dissipation capacity for GGSS-CIP.

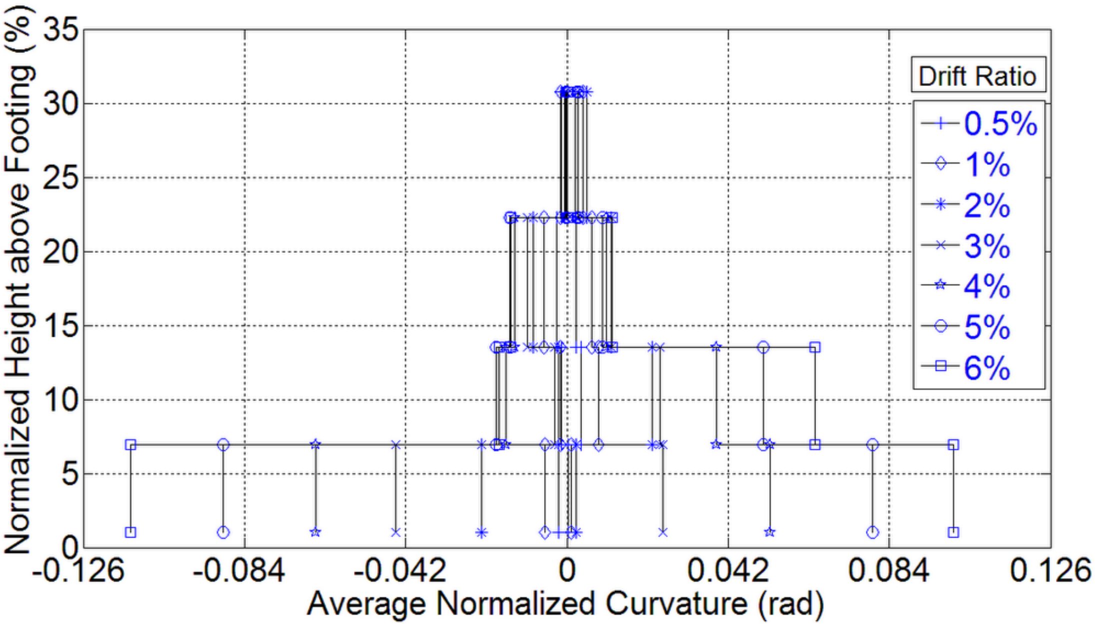

Figure 4.20 Normalized curvature distribution for GGSS-CIP.

4.2.4 Comparative Study of Column-to-Footing Joints

To compare the results from the experiments in this category of test specimens, it is essential to know the material properties for the rebar, concrete, and grout. Tension tests on reinforcing bars along with compression tests on concrete cylinders and grout cubes were performed for each test specimen. The results of tension tests on reinforcing bars for the column-to-footing specimens are presented in Table 4.1. It is observed that the same rebar was incorporated in both test alternatives. Table 4.2 contains the compression test results for the concrete and the grout utilized in the construction of the column-to-footing test specimens.

4.2.4.1 Force-Displacement Response

In the previous sections, the displacement ductility capacity of each test specimen was obtained based upon the hysteretic response to cyclic loads. The displacement ductility capacity of all specimens in this category is shown in Table 4.3, in addition to the parameters used to perform the calculations. It is noted that the displacement ductility capacity of specimens GGSS-1 and GGSS-2 was 5.4 and 6.1, respectively, which was lower than the displacement ductility of 8.9 that was achieved for the cast-in-place specimen GGSS-CIP. However, the displacement ductility capacities obtained for both precast test specimens exceeded the minimum displacement ductility capacity of 3.0 for ductile components as specified in Caltrans Seismic Design Criteria (SDC) [23]. According to the AASHTO-Seismic provisions, the local ductility demand for ductile members in high-seismic zones is limited to 5.0 and 6.0 for single-column bents and multiple-column bents, respectively [16].

Table 4.1 Rebar properties for column-to-footing specimens.

Specimen	Column Rebar			
	Longitudinal (NO. 8)		Transverse (NO. 4)	
	Yield	Ultimate	Yield	Ultimate
GGSS-1	68	93	63	103
GGSS-2	68	93	63	103
GGSS-CIP	68	93	63	103

Table 4.2 Concrete and grout properties for column-to-footing specimens.

Specimen	Concrete		Grout	
	28-day	Test day	28-day	Test day
GGSS-1	5.3	5.9	14.4	14.4
GGSS-2	3.9	5.5	11.1	13.5
GGSS-CIP	5.2	6.7	NA	NA

Table 4.3 Effective yield properties and displacement ductility for column-to-footing specimens.

Specimen	Last Drift Ratio (%)	F_y (kip)	Δ_y (in.)	Δ_u (in.)	K_{eff} (kip/in)	μ_Δ
GGSS-1	9	41.91	1.45	7.79	28.98	5.4
GGSS-2	7	32.63	1.05	6.42	31.00	6.1
GGSS-CIP	9	33.62	0.95	8.45	35.55	8.9

The force-displacement response of the column-to-footing test specimens revealed a noticeable distinction between the precast specimens and the GGSS-CIP. The GGSS-CIP failed due to rebar fracture of the column longitudinal bars as a result of the low cycle fatigue. A premature rebar fracture was observed for the case of specimens GGSS-1and GGSS-2 because of higher strain levels concentrated right at the end of the GGSS connectors located at the interface of the column to footing.

The backbone curve, or the so-called cyclic envelope, was constructed by joining the peak values of the first cycle for each drift ratio. Figure 4.21 shows the cyclic envelopes for the three column-to-footing test specimens. It is observed that the overall force-displacement performance of all test specimens is similar up a 1% drift ratio. Specimen GGSS-1 had a greater strength capacity than the control specimen GGSS-CIP. This was mainly attributed to the presence of the GGSS connectors in the column base, which led to a partial transition of the flexural action to the section right above the GGSS connectors. In addition, a higher axial load was applied to specimen GGSS-1 unintentionally, which resulted in a larger lateral force capacity for this test specimen. This axial load was 60% larger than the axial load applied to specimen GGSS-CIP, including the different concrete compressive strengths used for the two specimens.

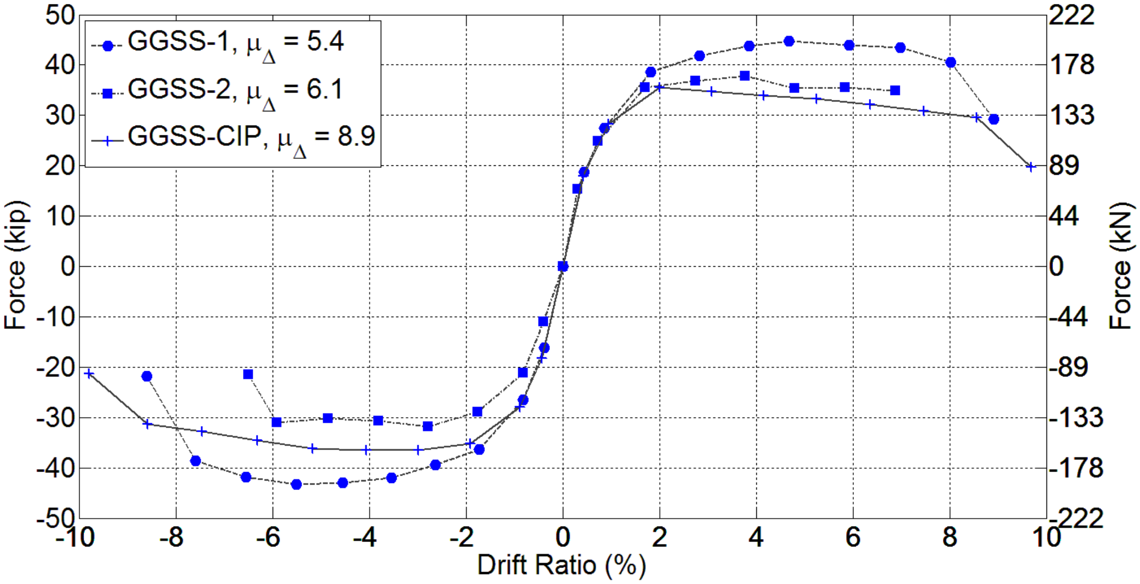

Figure 4.21 Force-displacement response of column-to-footing test specimens.

4.2.4.2 Stiffness Degradation

The effective stiffness was calculated in each cycle using the peak displacement values and the corresponding forces. The average of the stiffness values was then obtained for both cycles of every drift ratio. Figure 4.22 displays the average effective stiffness at each drift ratio for the three specimens. A similar trend was noted in the stiffness reduction per drift ratio for all specimens in this category. The degradation rate was much higher during the first few cycles mainly because of column rebar yielding.

For example, there was a 50% reduction in GGSS-1 stiffness by the end of the 2% drift ratio. The stiffness degradation graph indicates that precast specimens GGSS-1 and GGSS-2 had similar average component stiffness characteristics, and suggests that the GGSS connectors in the column base did not change the overall stiffness degradation rate. Specimen GGSS-1 had a slightly greater average stiffness at every drift ratio, mainly because of the higher lateral force capacity of the precast test model.

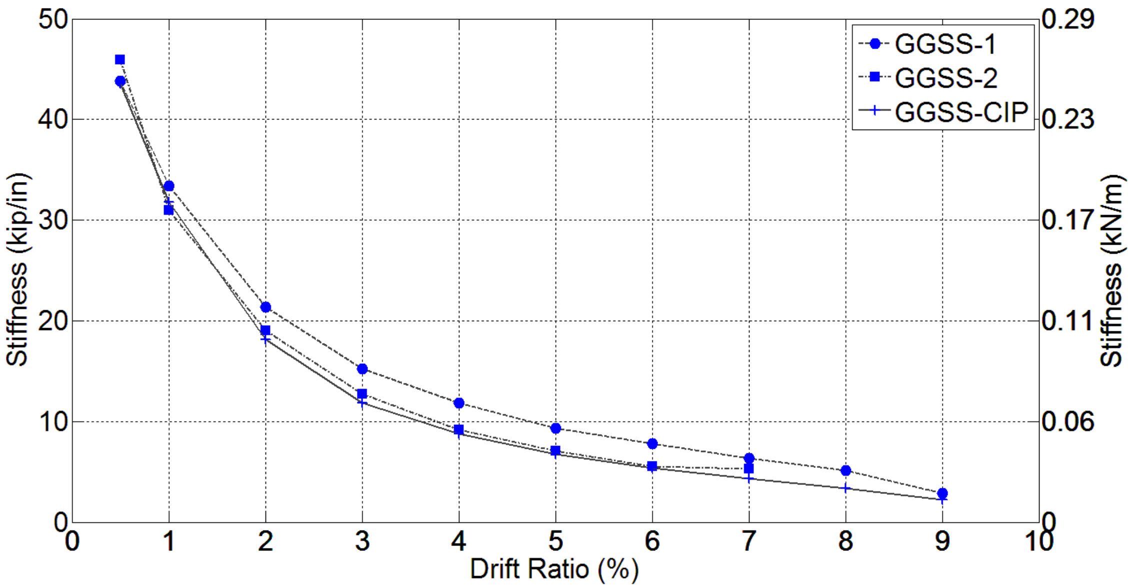

Figure 4.22 Stiffness degradation for column-to-footing specimens.

4.2.4.3 Energy Dissipation Capacity

The cumulative hysteretic energy capacity for the three column-to-footing test specimens is shown in Figure 4.23. As observed, the rate of this quantity, which is directly associated with the area under the hysteretic loops, increases with an increase in the drift ratio for both specimens. Figure 4.23 shows that all specimens had a very similar hysteretic energy dissipation capacity up to the 3% drift ratio, after which GGSS-CIP and GGSS-2 had a slightly better performance. This implies that the cast-in-place GGSS-CIP and GGSS-2 with mild steel in the plastic hinge region of the column dissipated more energy than he precast GGSS-1 at all drift ratios.

Equivalent viscous damping is another quantity used to evaluate the relative energy dissipation capacity of systems under cyclic loads. The equivalent viscous damping offers more information about the hysteretic response of the system since both the hysteretic and strain energy are included. The equivalent viscous damping ratio (ξ_{eq}) is obtained as the ratio of the hysteretic energy to the energy of the equivalent viscous system as defined in Equation (5) [24].

$$\xi_{eq} = \frac{E_D}{4\pi E_{S0}} \tag{5}$$

where E_D and E_{S0} are the area inside the hysteresis loop and the strain energy, respectively. Figure 4.24 presents the average ξ_{eq} of both cycles for each drift ratio. In the inelastic region of the response, which begins after completion of the 1% drift ratio, ξ_{eq} for all specimens increases with an increase in the drift ratio. At the 8% drift ratio, GGSS-CIP had a ξ_{eq} of 31%, which indicates a reasonable value for a reinforced concrete component with excellent seismic detailing. It is evident that specimens GGSS-CIP and GGSS-2 had greater ξ_{eq} during all drift ratios. For instance, ξ_{eq} at 6% drift ratio was 17%, 26%, and 24% for GGSS-1, GGSS-2, and GGSS-CIP, respectively. This implies that a relatively superior energy dissipation capability is achieved when there were no GGSS connectors in the plastic hinge region of the column, i.e., specimens GGSS-2 and GGSS-CIP.

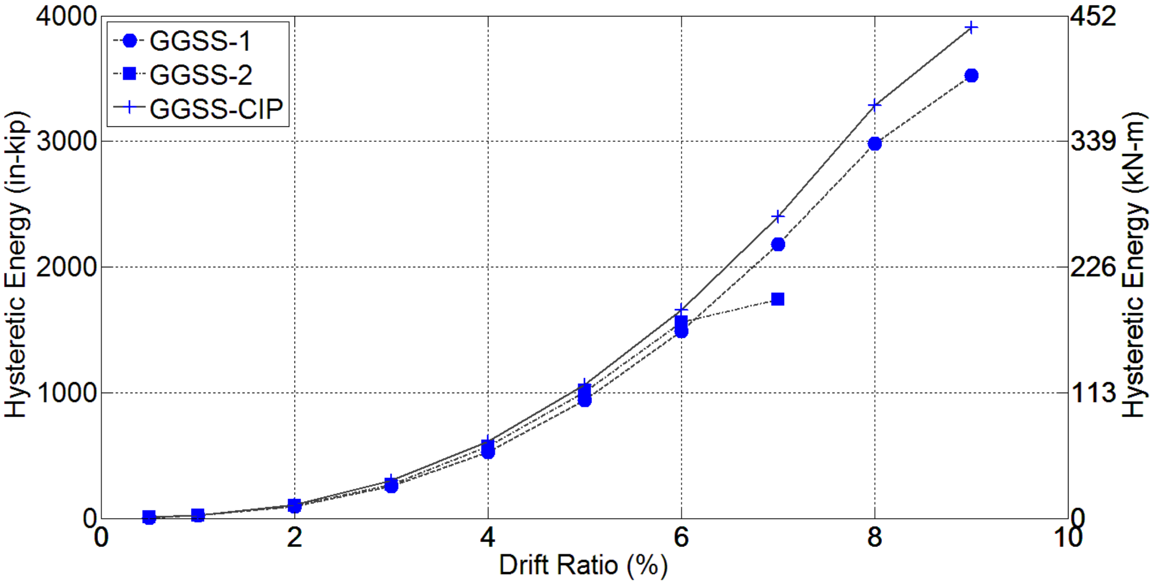

Figure4.23 Cumulative hysteretic energy for column-to-footing specimens.

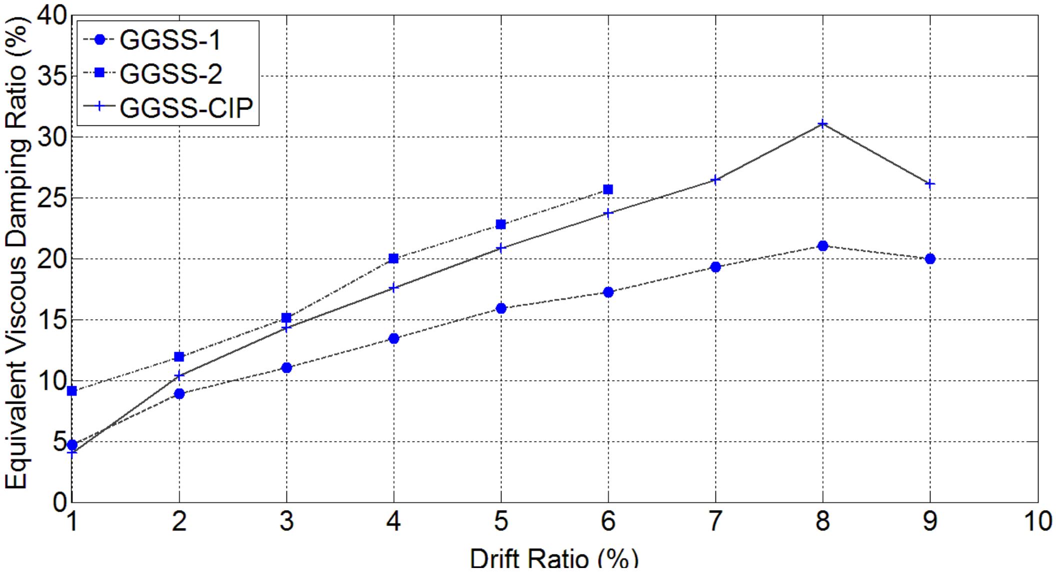

Figure 4.24 Equivalent viscous damping for column-to-footing specimens.

4.3 Response of Column-to-Cap Beam Joints

The measured response of the column-to-cap beam joints is presented in this section. The four evaluation methods described in Section 4.1 will be utilized to study the results obtained from the three tests. A comparative study will also be presented at the end of this section, emphasizing the similarities and differences that exist between the specimens.

4.3.1 FGSS-1 Results

4.3.1.1 Experimental Observations and Damage States

The hysteresis response of specimen FGSS-1 is shown in Figure 4.25, and it includes two major damage states, i.e., cracking and spalling of concrete, and rebar pull-out failure. The pinched hysteresis loops achieved for this specimen indicate that the overall force-displacement performance of FGSS-1 is controlled by the bond-slip characteristics of the FGSS connectors. In addition to pinching that occurred due to excessive slippage of the cap beam dowel bars in the FGSS connectors, rebar slippage introduced another type of disruption in the unloading branch of the response in the push direction. This condition was attributed to closure of the gap originally formed as a result of bond deterioration and the consequent bar slip. This gap closure phenomenon is readily visible on the unloading branch of the hysteresis loops for the 4%, 5%, and 6% drift ratios in the push direction.

The lateral force peaked at the 5% and 3% drift ratio in the push and pull direction, respectively. A gradual strength reduction or cyclic strength degradation was noted as a result of bond deterioration between the dowel bars and the grout inside the FGSS connectors. The test was terminated at the end of the 6% drift ratio due to a load reduction of 20% and 30% for the push and pull direction, respectively. Failure of FGSS-1 was caused by excessive bar slippage and the consequent pull-out of rebar from the FGSS connectors.

The first crack formed at the bed grout section, accompanied by another crack just above the FGSS connectors, during the first cycle of the 1% drift ratio. Both cracks were hairline and not measurable when the column returned to the stationary condition. All major cracks developed by the end of the 3% drift ratio. Spalling initiated at the corners of the octagonal column during the first cycle of the 3% drift ratio. The largest crack, which had been formed at the bed grout section during the previous drift, turned into a gap at the interface of the column to the cap beam during the 3% drift ratio. This is evident in Figure 4.26(a) that shows the gap opening while the column was at the peak displacement of the 3% drift ratio.

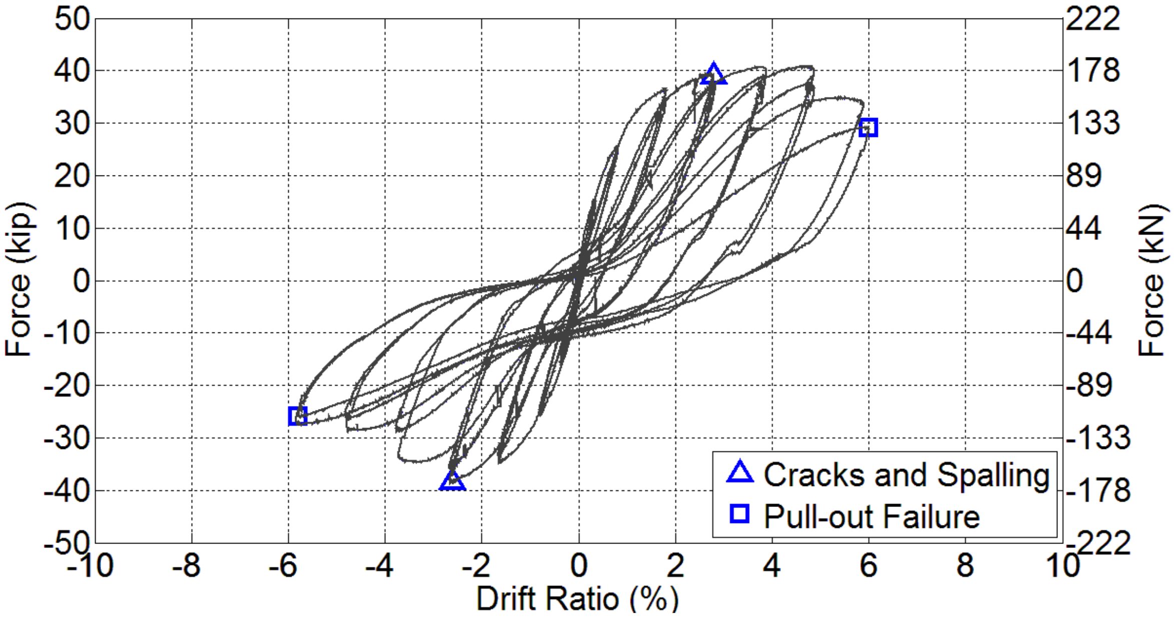

Figure 4.25 Hysteresis response of FGSS-1 with damage states.

Figure 4.26(b) displays the damage state at the end of this drift ratio. Cracks widened and concrete spalling progressed at higher drift ratios. During the 6% drift ratio, the cone shape of the expelled grout became visible when the test specimen was at maximum displacement in the pull direction. This condition is presented in Figure 4.26(c). The test was terminated after completion of the 6% drift ratio due to bond deterioration, and subsequent rebar pull-out. The height of the spalled concrete region was 8 in. on the west and 12 in. on the east side of the column, respectively. The spiral was partially exposed within the column end and the bed grout was crushed at the column peripheral. The permanent opening at the bed grout had a residual gap equal to 0.1 in. as shown in Figure 4.26(d).

The cap beam remained intact with only a few scattered minor cracks in the joint region. The test-day compressive strength of the concrete and grout was 6.2 ksi and 13.3 ksi, respectively.

(a) Bed grout opening at 3% drift ratio (peak).

(b) Damage state at 3% drift ratio.

(c) Bar pull-out during 6% drift ratio.

(d) Damage state at end of test.

Figure 4.26 FGSS-1 visual observations.

4.3.1.2 Displacement Ductility Capacity and Plastic Rotation Capacity

The average backbone curve was constructed in accordance with the method described in Section 4.1.2, along with the idealized elasto-plastic curve. Figure 4.27 depicts the two plots in addition to the parameters required to obtain the displacement ductility. The effective yield displacement and force for specimen FGSS-1 were 1.08 in. and 35.35 kip, respectively. The ultimate displacement, corresponding to a 20% strength drop, was 5.32 in., resulting in a displacement ductility of 4.9.

Figure 4.28 displays the moment-plastic rotation relationship up to test termination. The plot shows that specimen FGSS-1 had a plastic rotation of 0.0371 rad at the 5% drift ratio before excessive strength reduction.

4.3.1.3 Cumulative Energy Dissipation

The cumulative hysteretic energy versus drift ratio is plotted in Figure 4.29. There was an increase in energy dissipation with an increase in the drift ratio as the specimen underwent inelastic performance. The cumulative hysteretic energy was found to be 218 in-kip and 1,021 in-kip at 3% and 6% drift ratio, respectively.

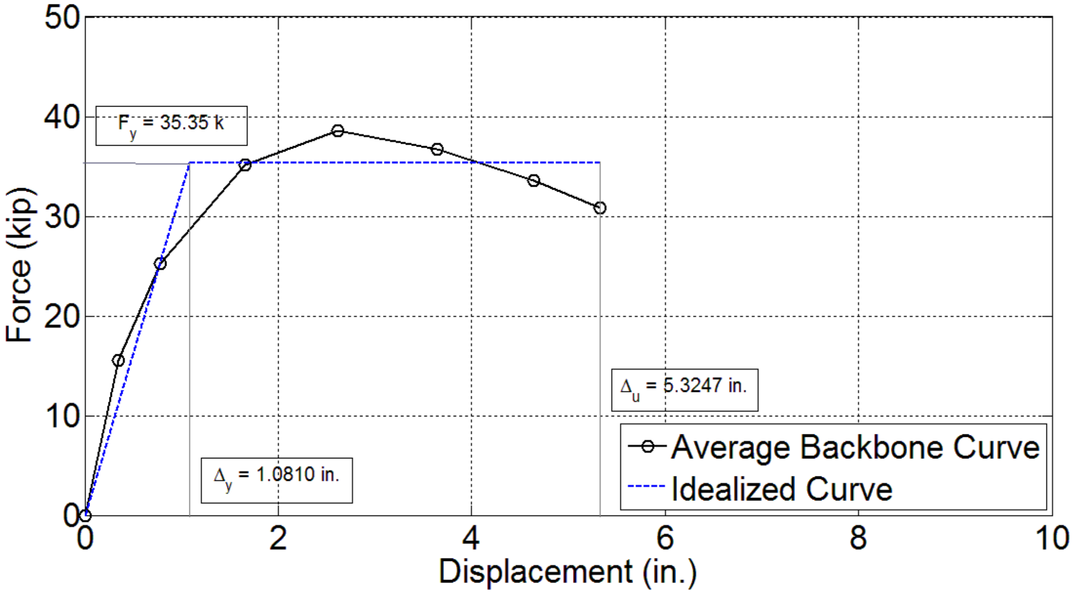

Figure 4.27 Average backbone curve and displacement ductility for FGSS-1.

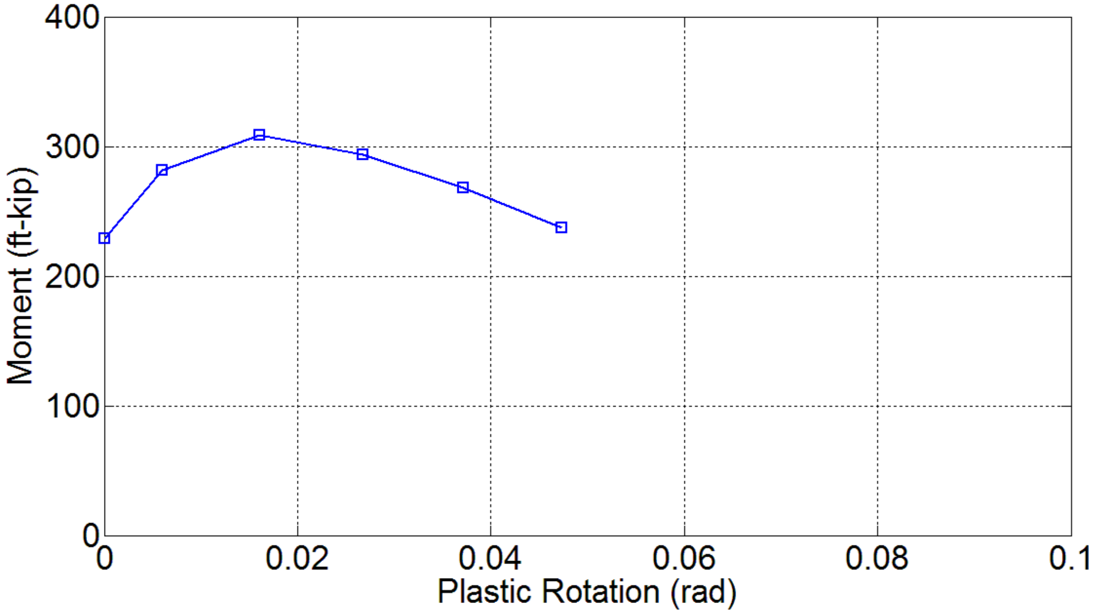

Figure 4.28 Plastic rotation capacity for FGSS-1.

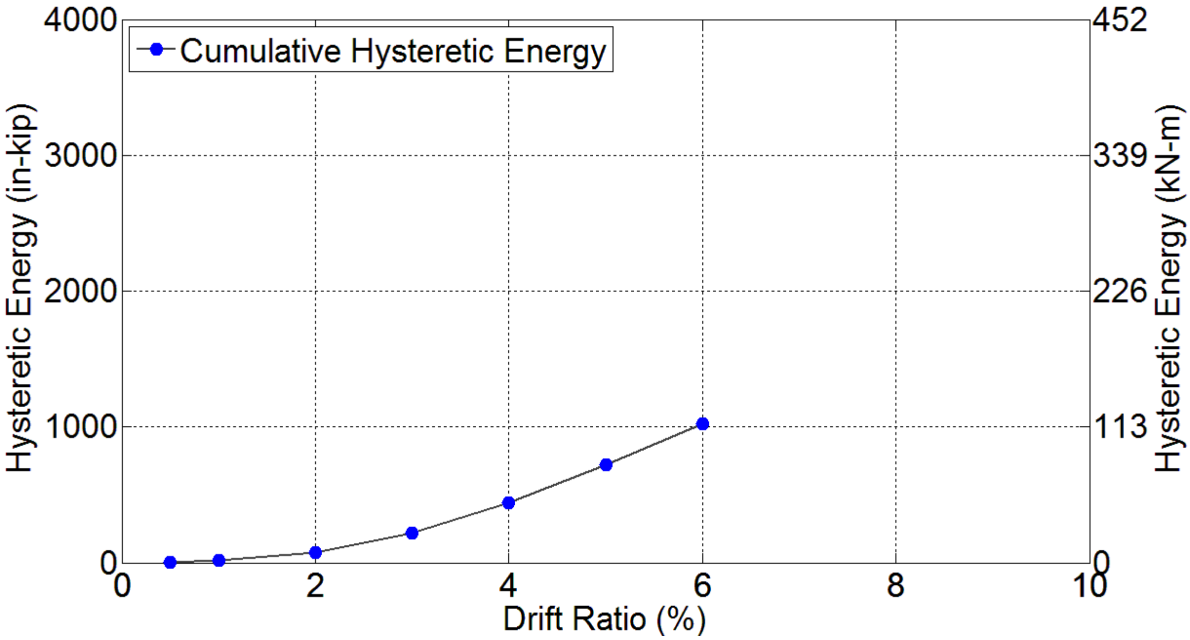

Figure 4.29 Energy dissipation capacity of FGSS-1.

4.3.1.4 Column Curvature Profile

The normalized curvature distribution along the column base is shown in Figure 4.30. The curvature profile indicates that the curvature capacity is a minimum over the FGSS region, and flexural action is concentrated at sections above and below the FGSS connectors. An examination of this curvature profile revealed that the column rebars did not develop considerable stresses for the portion that was embedded in the FGSS connectors.

Strain gauges located on the extreme longitudinal bars, in the column base, and within the joint core covered an area with a depth of 7 in. into the cap beam and 16¼ in. above the column base. These strain gauges showed that both extreme bars yielded over the whole range covered by strain gauges, except for the initial 5-in. portion of the field dowels, which were embedded and confined inside the FGSS connectors.

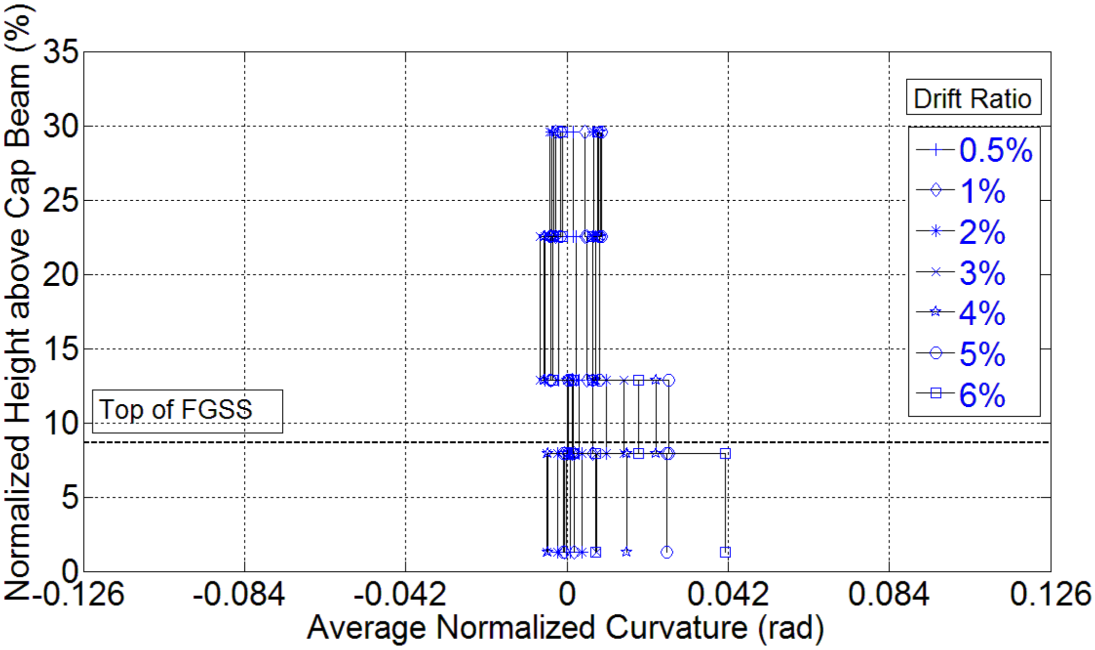

Figure 4.30 Normalized curvature distribution for FGSS-1.

4.3.2 FGSS-2 Results

4.3.2.1 Experimental Observations and Damage States

Figure 4.31 depicts the lateral force-displacement performance of specimen FGSS-2 including three damage states, which were: (1) crack formation and initiation of concrete spalling, (2) fracture of rebar, and (3) rebar pull-out as a result of bond-slip. Hysteresis loops were relatively wide and stable compared with specimen FGSS-1, without any considerable strength degradation before the rebar fracture or pull-out events during the last drift ratio. The peak lateral forces of 34.7 kip and 36.3 kip occurred at the 4% and 5% drift ratio, in the push and pull direction, respectively. The west column rebar fractured in the first cycle of the 7% drift ratio, while the east column bar underwent excessive slippage that resulted in considerable strength reduction. Ultimately, test termination was enforced after completion of the 7% drift ratio, because of a drop in strength of 42% and 45% occurred in the lateral force capacity, as a result of east rebar fracture and west rebar pull-out. This was a unique failure mode because it contained both a ductile failure and a bond-slip failure. The gap closure phenomenon described for specimen FGSS-1 was observed for this specimen as well, an indication of excessive rebar slip at the 4% drift ratio.

A hairline flexural crack formed at a section 12 in. above the column base during the 0.5% drift ratio. During the next drift ratio of 1%, this crack had a width of 0.002 in. Two more flexural cracks developed at 20 in. and 28 in. above the column end during the same drift ratio.

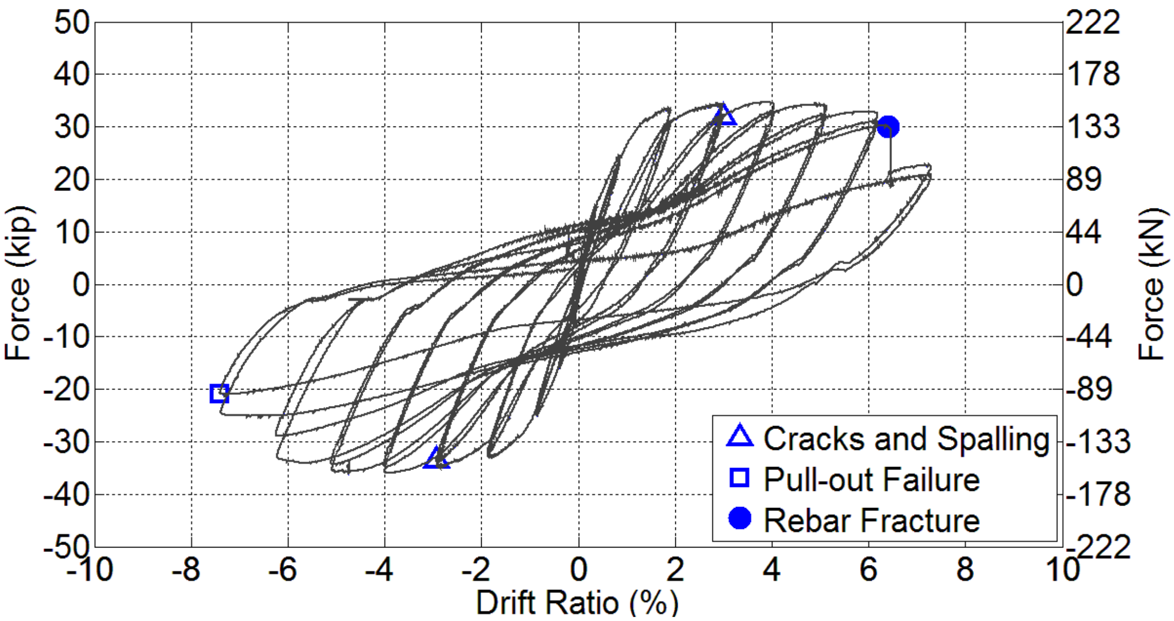

Figure 4.31 Hysteresis response of FGSS-2 with damage states.

More cracks developed during the 2% and 3% drift ratio, including one at the bed grout. Overall, there were seven major flexural cracks that formed along the column by the end of the 3% drift ratio. The width of the crack that was formed during the 2% drift ratio at a section 8 in. from the column base measured 0.03 in. at the end of the 3% drift ratio. Concrete cover spalling initiated during this drift ratio with a height of 8 in. on the column's east side. Cracks opened further and concrete spalling intensified after the 3% drift ratio until test termination. Flexure-shear cracks formed on the north and south side of the column during the 5% drift ratio, while the representative crack at 8 in. above the column base had a width of 0.04 in. Spalling became deeper and wider during the 6% drift ratio and a considerable strength reduction was noted at the end of the second cycle in the push direction. This was attributed to the bond deterioration between the grout and the embedded column dowel.

The column extreme west bar broke at the end of the first cycle of the 7% drift ratio, whereas the east bar did not fracture; however, the drop in the lateral force capacity for the pull direction implied that a bond-related phenomenon had caused a sudden reduction in strength. Post-test observations showed that the spiral became exposed near the column end, and the largest flexural crack, which was found 4 in. above the column base, measured 0.06 in. The location of the rebar fracture was spotted 1 in. above the column base, right below the spiral. Similar to the previous test specimens, low cycle fatigue was the cause of rebar fracture as a result of successive bending and re-straightening of the column extreme bars. A permanent gap with a depth of 0.125 in. and 0.0625 in. remained at the bed grout section on the east and west side of the column, respectively. Figure 4.32 shows the damage state at the 3% and 7% drift ratio.

4.3.2.2 Displacement Ductility Capacity and Plastic Rotation Capacity

A displacement ductility of 5.8 was obtained for this test specimen using the standard procedure described in Section 4.1.2 as shown in Figure 4.33. The idealized curve was constructed to achieve all parameters required to compute the displacement ductility capacity. The ultimate displacement of 6.50 in. was associated with a 20% drop in the lateral force capacity of this test specimen. Effective yield strength and yield displacement were obtained as 33.29 kip and 1.11 in., respectively.

Figure 4.34 displays the moment-plastic rotation relationship up to test termination. The plot shows that specimen FGSS-2 had a plastic rotation of 0.0505 rad that occurred at the 6% drift ratio. This was associated with a condition of negligible strength degradation.

(a) Damage state at 3% drift ratio: cracks and spalling.

(b) Damage state at 7% drift ratio: cracks, spalling, and exposed spiral.

Figure 4.32 FGSS-2 visual observations.

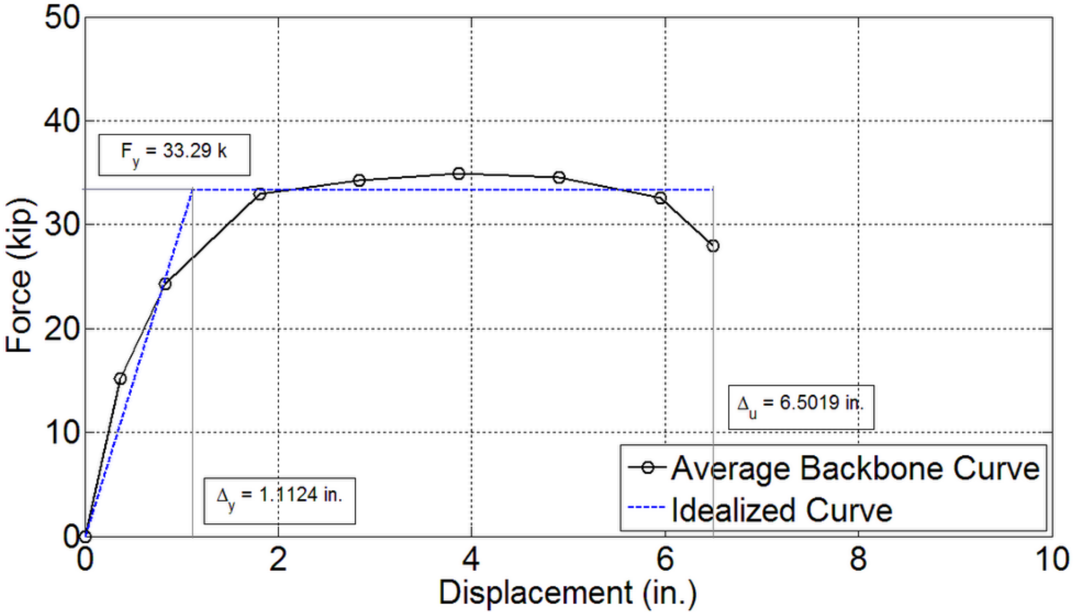

Figure 4.33 Average backbone curve and displacement ductility of FGSS-2.

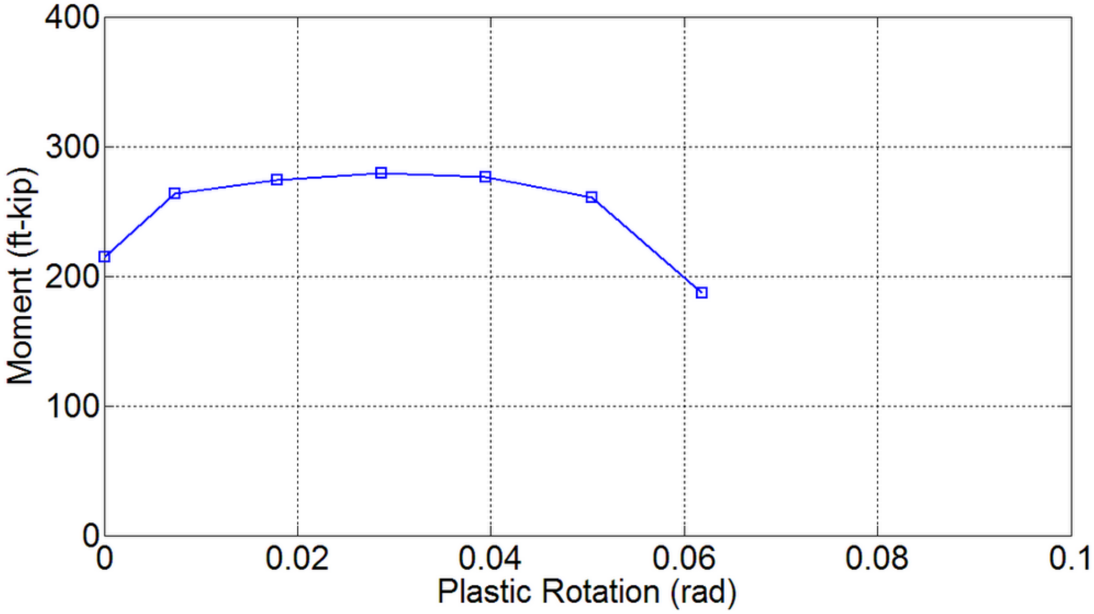

Figure 4.34 Plastic rotation capacity for FGSS-2.

4.3.2.3 Cumulative Energy Dissipation

Figure 4.35 shows the cumulative hysteretic energy per drift ratio. Specimen FGSS-2 dissipated energy continuously up to the end of the 6% drift ratio. In the 7% drift ratio, a slightly lower dissipation rate was achieved because of the west rebar fracture and east rebar pull-out. The cumulative hysteretic energy was found to be 241 in-kip and 1,859 in-kip for the 3% and 7% drift ratios, respectively.

4.3.2.4 Column Curvature Profile

Without the presence of the FGSS connectors in the column base, a very good curvature distribution was achieved for this test specimen, as presented in Figure 4.36. This is similar to the curvature distribution which commonly exists in cast-in-place construction with either standard lapped splices with good details or monolithic construction, in which no disruption is introduced to the natural stress transfer between the adjoining components. Neglecting the asymmetric curvature distribution for the push and pull direction, this curvature profile resembles an acceptable distribution of curvature demand along the column plastic hinge region, with the highest curvature values at the column base where moment is also a maximum and a gradual decrease in curvature away from the joint.

Strain gauges located on the extreme longitudinal bars, in the column base and within the joint core, covered an area with a depth of 13 in. into the cap beam and 18 in. above the column end. These strain gauges showed that the extreme column dowels yielded starting at 5 in. from the tip of the column dowel bars, which were confined within the FGSS connectors; in other words, 2 in. into the cap beam from the column-to-cap beam interface. On the contrary, the cap beam dowel bars did not perform inelastically and strain values remained below the rebar yield strength.

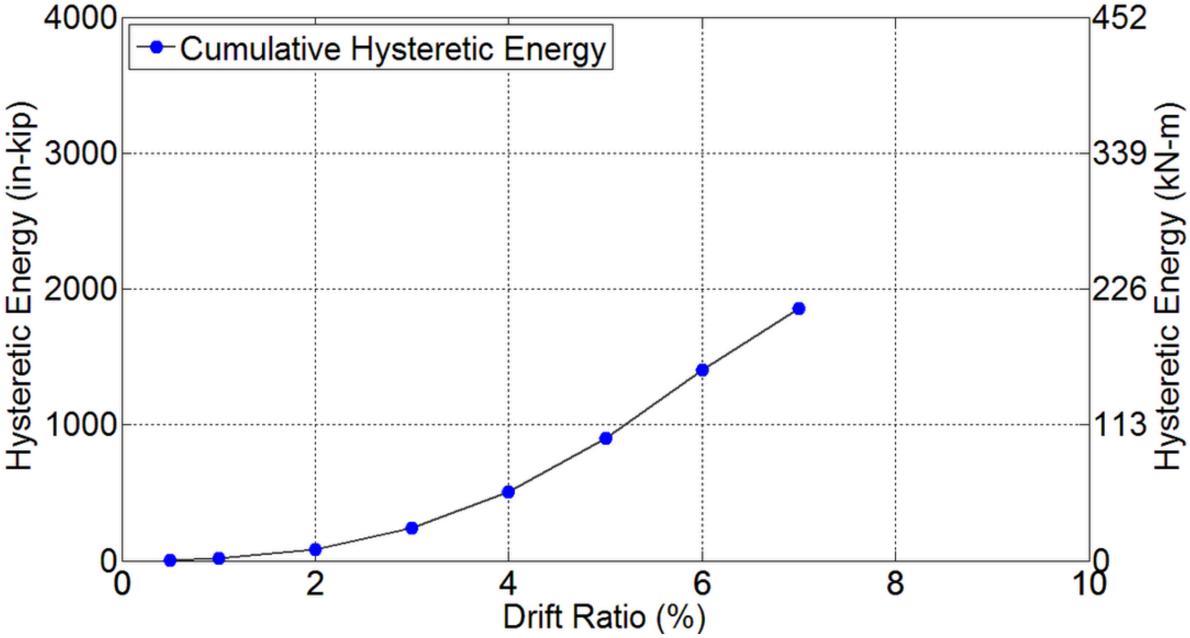

Figure 4.35 Energy dissipation capacity of FGSS-2.

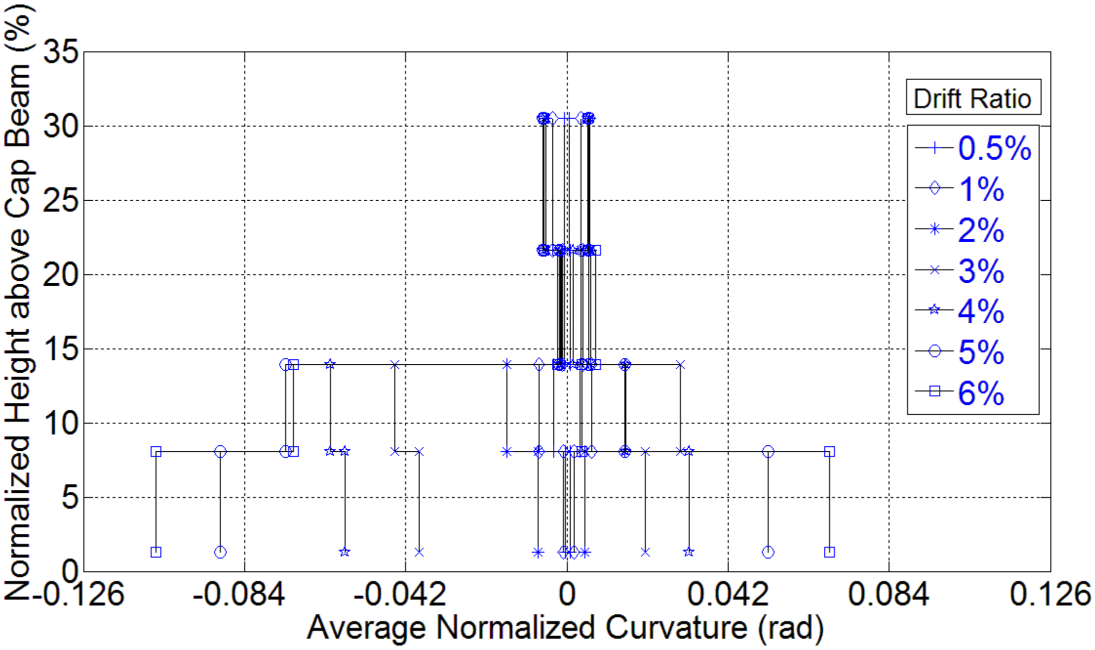

Figure 4.36 Normalized curvature distribution for FGSS-2.

4.3.3 FGSS-CIP Results

4.3.3.1 Experimental Observations and Damage States

The hysteretic response of this test specimen is presented in Figure 4.36, in addition to damage states corresponding to (1) end of major crack formation and beginning of spalling, (2) observation of yield penetration, and (3) rebar fracture. The overall response was satisfactory as a result of the wide and stable hysteresis loops that implied a relatively high energy dissipation capacity. This desirable performance represented a ductile response of a well-detailed reinforced concrete flexural component, under both axial and lateral loading. The lateral load peaked at 37.75 kip during the 2% drift ratio and 33.93 kip during the 3% drift ratio for the push and pull direction, respectively. A slight strength softening was evident especially for the push direction. This was attributed to deterioration of the concrete cover, which was relatively larger than the corresponding precast test specimens. The thicker concrete cover was provided to keep the column effective depth identical for all test specimens.

This test was terminated at the end of the 10% drift ratio due to fracture of both extreme east and west column longitudinal column bars. The west rebar fractured when the column top was close to the peak displacement during the first cycle. Subsequently, the bar on the opposite side of the column fractured during the first pull.

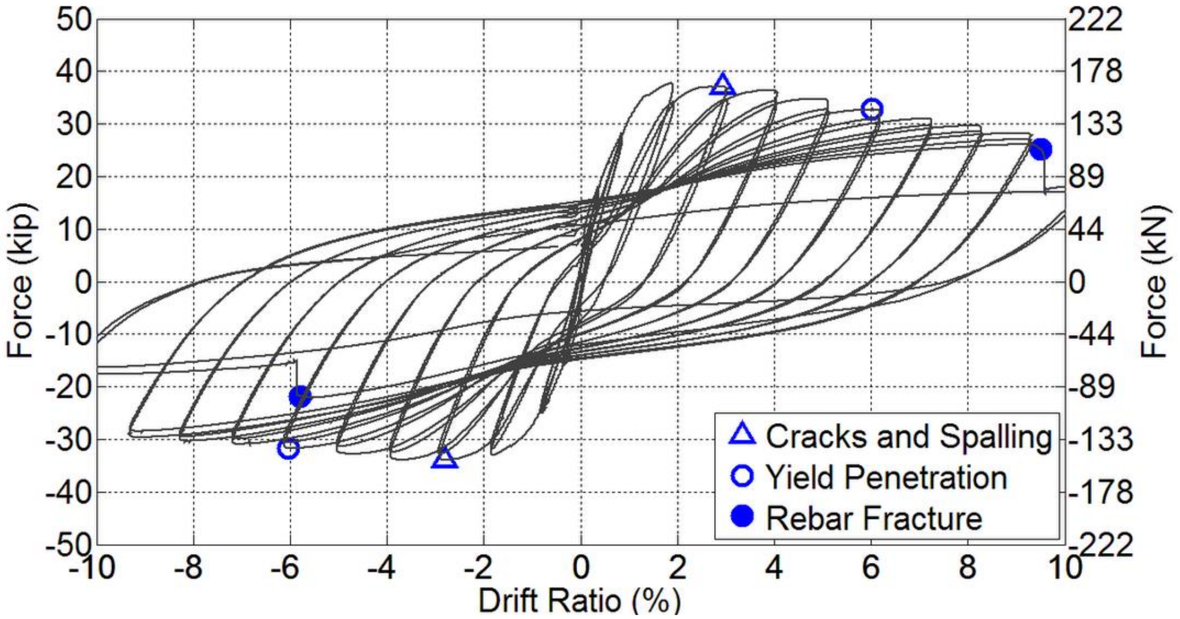

Figure 4.37 Hysteresis response of FGSS-CIP with damage states.

A few hairline flexural cracks appeared as early as the end of the 0.5% drift ratio over a 40-in. long region from the column base. More hairline flexural cracks developed during the 1% drift ratio, up to 60 in. above the column base. Those cracks, which had formed within the lowermost 12-in. portion of the column, grew larger in width during the 2% drift ratio. Also, a relatively large crack, with a width of 0.03 in., formed at the interface of the column-to-cap beam connection. The crack at 12 in. up from the column base had a width of 0.005 in. at the end of this drift ratio. Similar to the precast test specimens, all major flexural cracks developed by the end of the 3% drift ratio and concrete cover spalling began at the corners of the octagonal column. The crack at the interface remained unchanged while the crack at 12 in. up from the column base was 0.01 in. Figure 4.38 displays the damage state at the end of the 3% drift ratio.

Figure 4.38 Damage state for FGSS-CIP at 3% drift ratio.

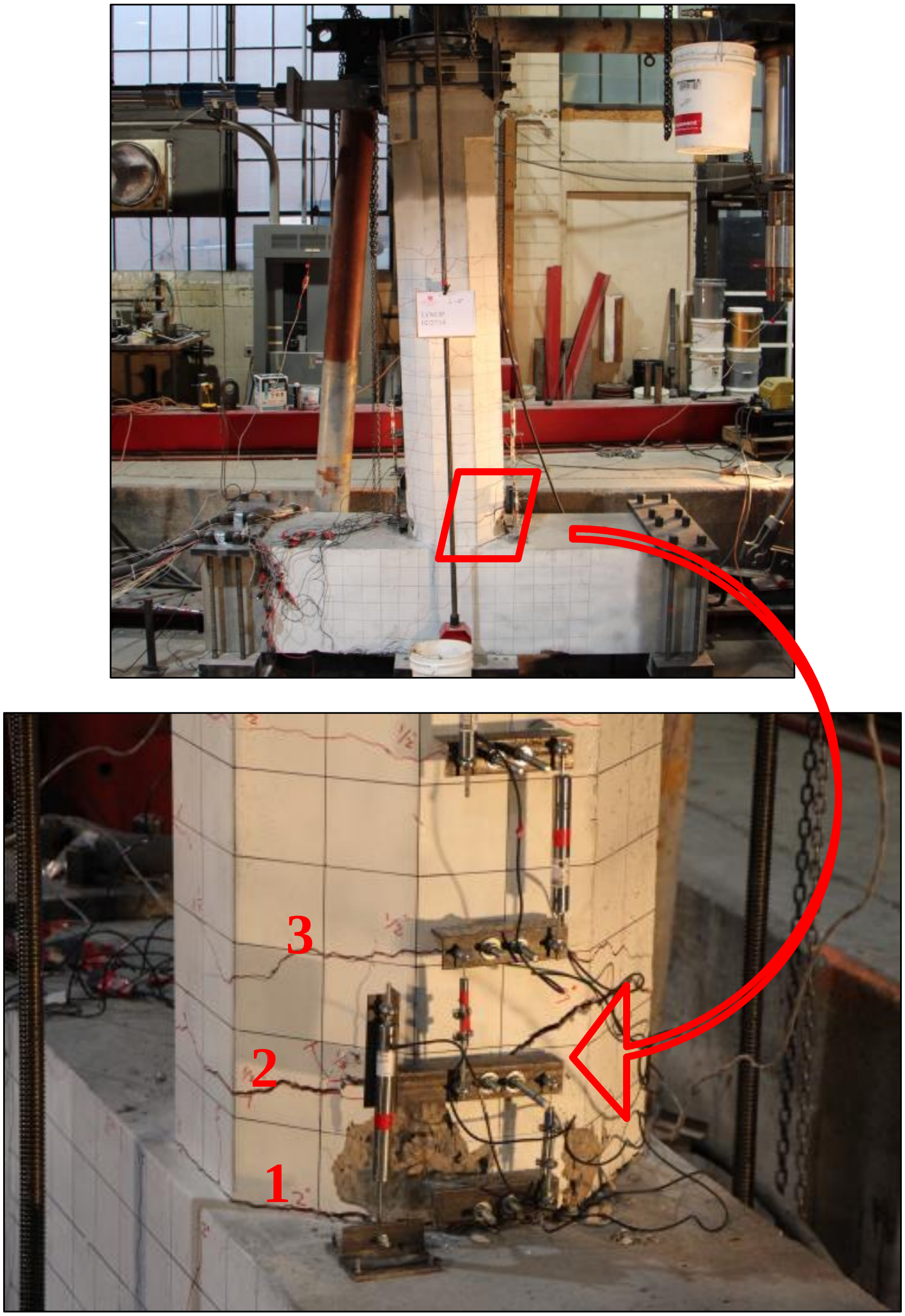

Figure 4.39 FGSS-CIP at peak displacement during 4% drift ratio; largest three cracks.

Inclined cracks formed on the north and south side of the column base during the 4% drift ratio. Figure 4.39 shows the three existing largest cracks within the column plastic hinge region at the peak displacement condition of the 4% drift ratio. These cracks measured 0.04 in., 0.06 in., and 0.013 in. for the crack at the interface, 6 in. from the column base, and 12 in. from the column base, respectively, when the column returned to the stationary condition.

Yield penetration was noted around the two column extreme bars at the end of the 6% drift ratio. Spalling became wider and deeper, covering the cracks developed during the previous cycles. Figure 4.40 shows the state of damage to the column at the end of the 6% drift ratio. In the 7% drift ratio, the column spiral became visible and the depth of yield penetration increased to 1.125 in. The column extreme longitudinal rebar was visible during the 8% drift ratio, implying that the concrete cover was completely crushed, which led to buckling of the rebar during the next drift ratio.

Low cycle fatigue caused fracture of the column extreme bars on both sides in the first cycle of the 10% drift ratio. The west column bar fractured in the push direction first, and then the east column bar fractured in the pull direction. Post-test investigation indicated that fracture of the rebar occurred at 1 in. and 1.50 in. above the cap beam, for the west and east column bars, respectively. The spalled region had an effective width of 21 in. and height of 8 in., although the maximum height of the spalled area was 16 in. and 20 in. for the east and west column sides, respectively. The cap beam horizontal rebar was revealed as a result of continuous yield penetration of the column rebar. Figure 4.41 shows the damage state for this test specimen at the end of the test.

The cap beam remained intact with only two minor cracks developed in the joint region during the 2% drift ratio. The test-day compressive strength of the concrete was found to be 6.7 ksi.

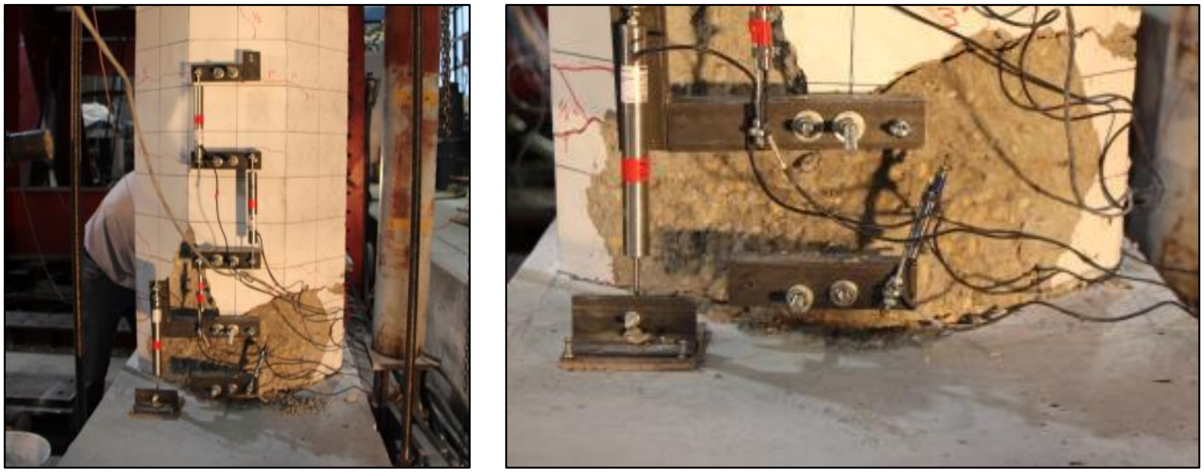

Figure 4.40 Damage state for FGSS-CIP at 6% drift ratio: cracks and spalling, yield penetration.

Figure 4.41 Damage state for FGSS-CIP: cracks and spalling, rebar buckling and fracture.

4.3.3.2 Displacement Ductility Capacity and Plastic Rotation Capacity

The average backbone curve superimposed with the idealized elasto-plastic curve is presented in Figure 4.42. The effective yield strength and yield displacement of specimen FGSS-CIP was 32.33 kip and 0.90 in., respectively, and the ultimate displacement, associated with strength equal to 80% of the peak lateral force, was 8.96 in. Therefore, the displacement ductility of this specimen was obtained as 9.9—the most ductile performance among all specimens.

A plastic rotation of 0.0837 rad was achieved for specimen FGSS-CIP at 9% drift ratio prior to the sudden strength reduction, which occurred due to rebar fracture. Figure 4.43 shows the moment-plastic rotation plot for this test specimen.

4.3.3.3 Cumulative Energy Dissipation

The cumulative energy dissipation per drift ratio is presented in Figure 4.44, which implies an acceptable performance in terms of energy dissipation capacity. This specimen dissipated more energy with an increase in drift ratios up to a 9% drift ratio after which there was a sudden reduction when the column longitudinal bars fractured. The cumulative hysteretic energy was 276 in-kip, 1,549 in-kip, and 4,788 in-kip at the end of the 3%, 6%, and 10% drift ratio.

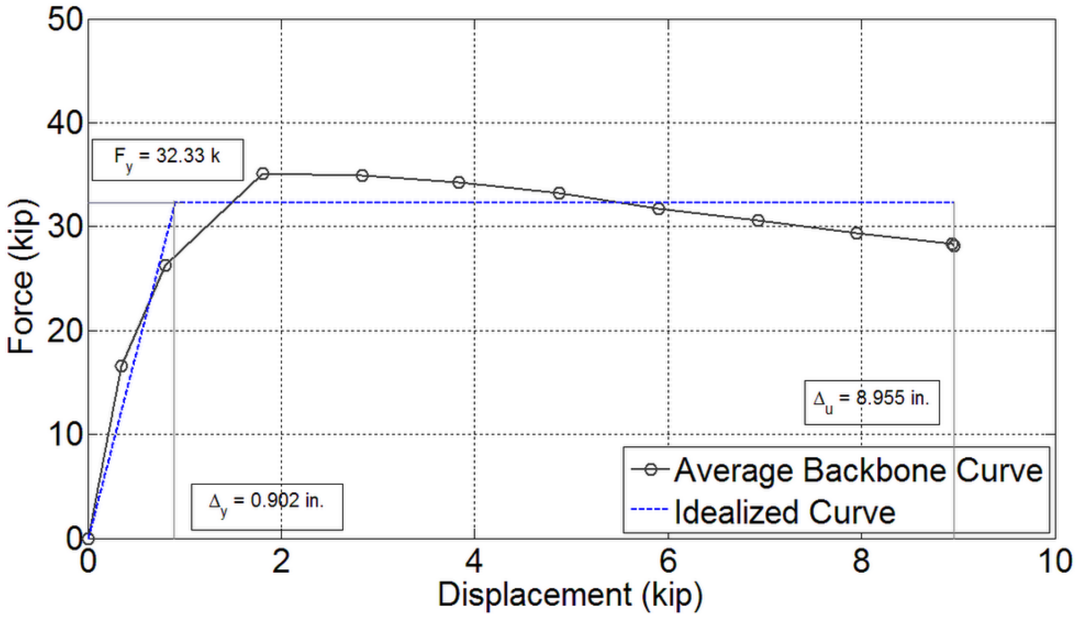

Figure 4.42 Average backbone curve and displacement ductility of FGSS-CIP.

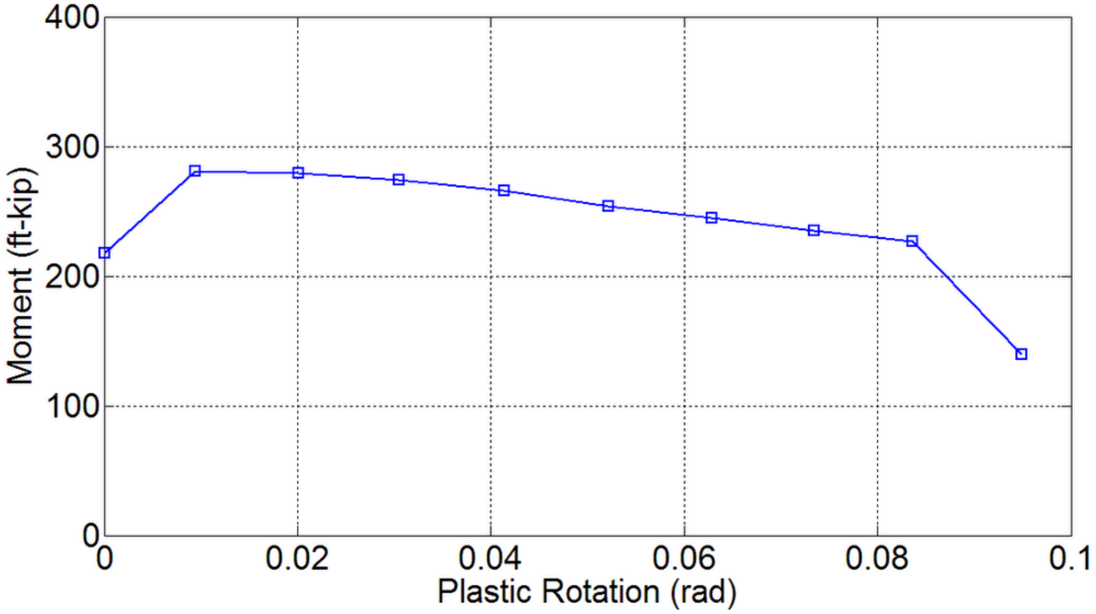

Figure 4.43 Plastic rotation capacity for FGSS-CIP.

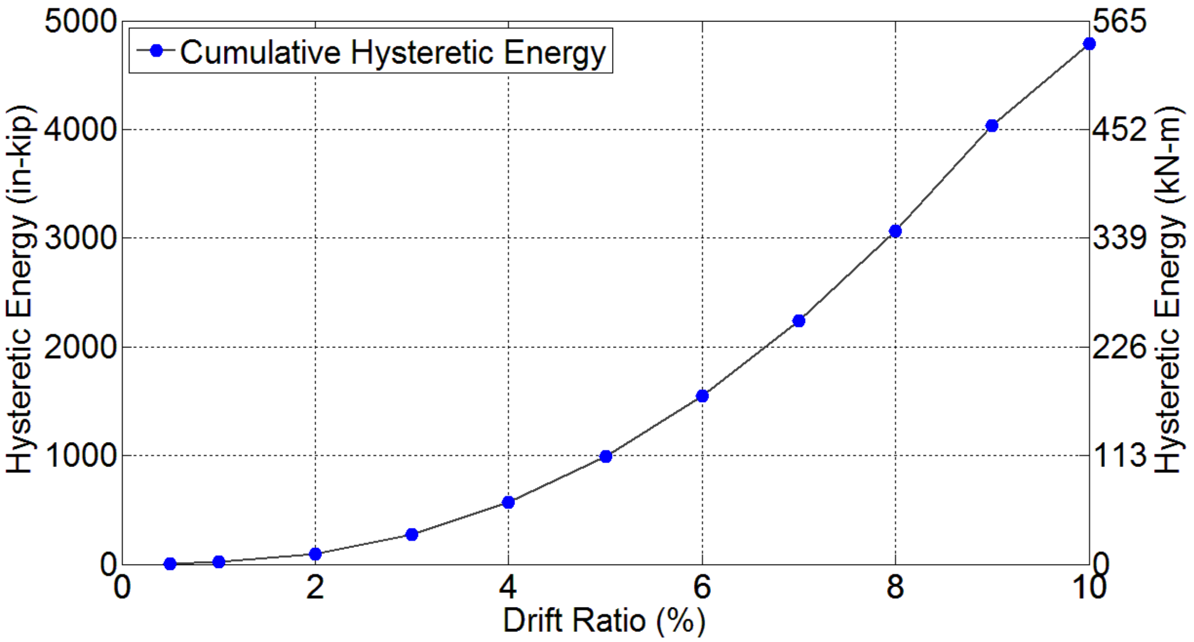

Figure 4.44 Energy dissipation capacity for FGSS-CIP.

4.3.3.4 Column Curvature Profile

Specimen FGSS-CIP had a desirable curvature distribution along the column base. This was attributed to the well-detailed column plastic hinge region without the presence of the FGSS connectors for splicing the dowel bars. The curvature demand increased toward the column end with an increase in the moment for a cantilever condition, as shown in Figure 4.45. This curvature profile was similar to the curvature profile for specimen FGSS-2 since the FGSS connectors were inside the cap beam and, similar to specimen FGSS-CIP, there were no splice sleeve connectors inside the column.

Strain gauges located on the extreme longitudinal bars, in the column end and within the joint core, covered an area with a depth of 9½ in. into the cap beam and 38 in. above the column end. These strain gauges showed that both extreme column bars yielded within this instrumented region.

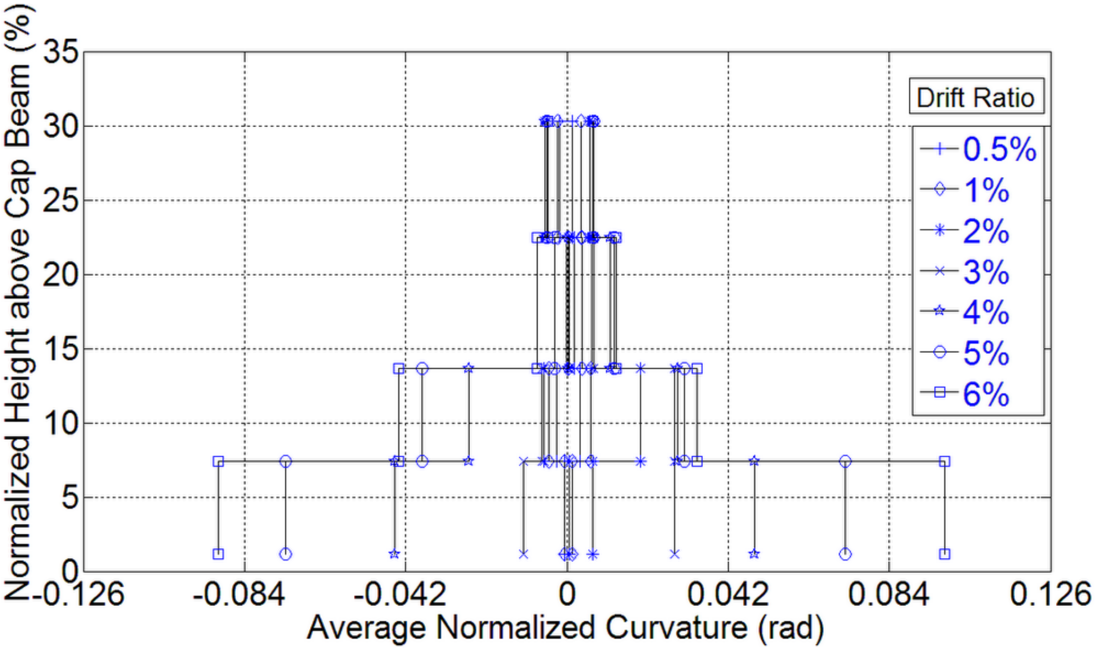

Figure 4.45 Normalized curvature distribution for FGSS-CIP.

4.3.4 Comparative Study of Column-to-Cap Beam Joints

To compare the results from the experiments in this category of test specimens, it is essential to know the material properties for the rebar, concrete, and grout. Tension tests on reinforcing bars, along with compression tests on concrete cylinders and grout cubes, were performed for each test specimen. The results of tension tests on reinforcing bars for the column-to-cap beam specimens are presented in Table 4.4. It is observed that the cap beam dowel bars had different material properties than the column dowel bars for the precast test alternatives. Table 4.5contains the compression test results for the concrete and the grout utilized in the construction of the column-to-cap beam test specimens.

4.3.4.1 Force-Displacement Response

In the previous sections, the ductility capacity of each test specimen was obtained based on the hysteretic response to the simulated seismic loads. The displacement ductility capacity of the specimens in this category is shown in Table 4.6, in addition to the parameters used to perform the calculations. It is noted that specimen FGSS-1 had a displacement ductility capacity of 4.9, whereas specimen FGSS-CIP had a displacement ductility of 9.9, which indicated a highly ductile response under the quasi-static loading protocol. Specimen FGSS-2 had a displacement ductility capacity of 5.8, which was larger than that for specimen FGSS-1. The displacement ductility capacities obtained for all precast test specimens exceeded the minimum displacement ductility capacity of 3.0 for ductile components as specified in

Table 4.4 Rebar properties for column-to-cap beam specimens.

Specimen	Column Rebar				Cap Beam Rebar			
	Longitudinal (NO. 8)		Transverse (NO. 4)		Dowel Bar (NO. 8)		Transverse (NO. 4)	
	Yield	Ultimate	Yield	Ultimate	Yield	Ultimate	Yield	Ultimate
FGSS-1	77	102	63	103	68	93	63	103
FGSS-2	68	93	63	103	77	102	63	103
FGSS-CIP	68	93	63	103	68	93	63	103

Table 4.5 Concrete and grout properties for column-to-cap beam specimens.

Specimen	Concrete		Grout	
	28-day	Test day	28-day	Test day
FGSS-1	5.3	6.2	12.5	13.3
FGSS-2	3.9	5.2	10.3	10.3
FGSS-CIP	5.2	6.7	NA	NA

Table 4.6 Effective yield properties and displacement ductility for column-to-cap beam specimens.

Specimen	Last Drift Ratio (%)	F_y (kip)	Δ_y (in.)	Δ_u (in.)	K_{eff} (kip/in)	μ_Δ
FGSS-1	6	35.35	1.08	5.32	32.70	4.9
FGSS-2	7	33.29	1.11	6.50	29.92	5.8
FGSS-CIP	10	32.33	0.90	8.95	35.84	9.9

Caltrans Seismic Design Criteria (SDC) [23]. According to the AASHTO-Seismic provisions, the local ductility demand for ductile members in high-seismic zones is limited to 5.0 and 6.0 for single-column bents and multiple-column bents, respectively [16].

The force-displacement response of the column-to-cap beam test specimens revealed a noticeable distinction between the precast specimens and the FGSS-CIP. The FGSS-CIP failed due to rebar fracture of the column longitudinal bars as a result of low cycle fatigue; however, FGSS-1 failed because of the excessive bond-slip and consequent pull out of rebar. FGSS-2 had a combined failure mode of premature rebar fracture and rebar pull-out failure that occurred for the two opposite extreme column bars.

The backbone curve, or cyclic envelope, was constructed by joining the peak values of the first cycle for each drift ratio. Figure 4.46 shows the cyclic envelopes for all column-to-cap beam specimens. It is observed that the overall force-displacement performance of the test specimens is similar up to the 1% drift ratio. Specimen FGSS-1 had a greater strength capacity than FGSS-2 and the cast-in-place FGSS-CIP. This was mainly attributed to the presence of the FGSS connectors in the column base, which led to a partial transition of the flexural action to the section right above the FGSS region. However, a higher axial load was applied to specimen FGSS-1 unintentionally, which resulted in a larger lateral force capacity for this test specimen. This axial load was 40% larger than the axial load applied to specimen FGSS-CIP, including the different concrete compressive strength used for the two specimens. The lateral force capacity of FGSS-1 was 11% greater than that of specimen FGSS-CIP, including the effect of both a higher axial load along with the presence of the FGSS connectors in the column base.

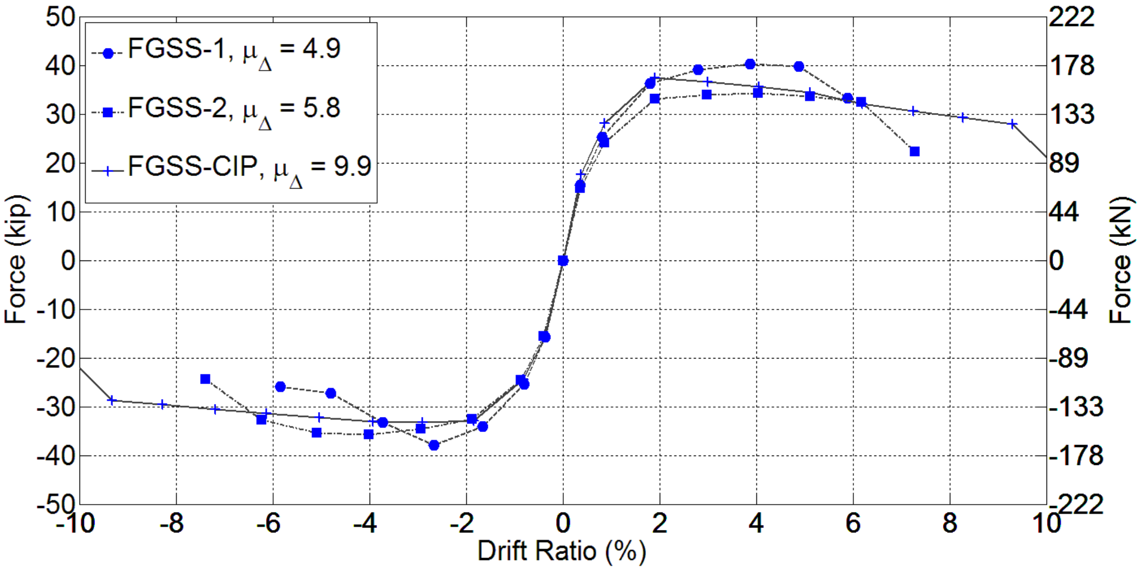

Figure 4.46 Force-displacement response of column-to-cap beam specimens.

4.3.4.2 Stiffness Degradation

The effective stiffness was calculated in each cycle using the peak displacement values and corresponding forces. The average of the stiffness values was then obtained for both cycles at each drift ratio. Figure 4.47 displays the average effective stiffness at each drift ratio for the three specimens. A similar trend was noted in the stiffness reduction per drift ratio for all specimens. This implies that the precast specimens had similar average component stiffness characteristics, and suggests that using the FGSS connectors in the column base or cap beam did not change the overall stiffness degradation rate considerably.

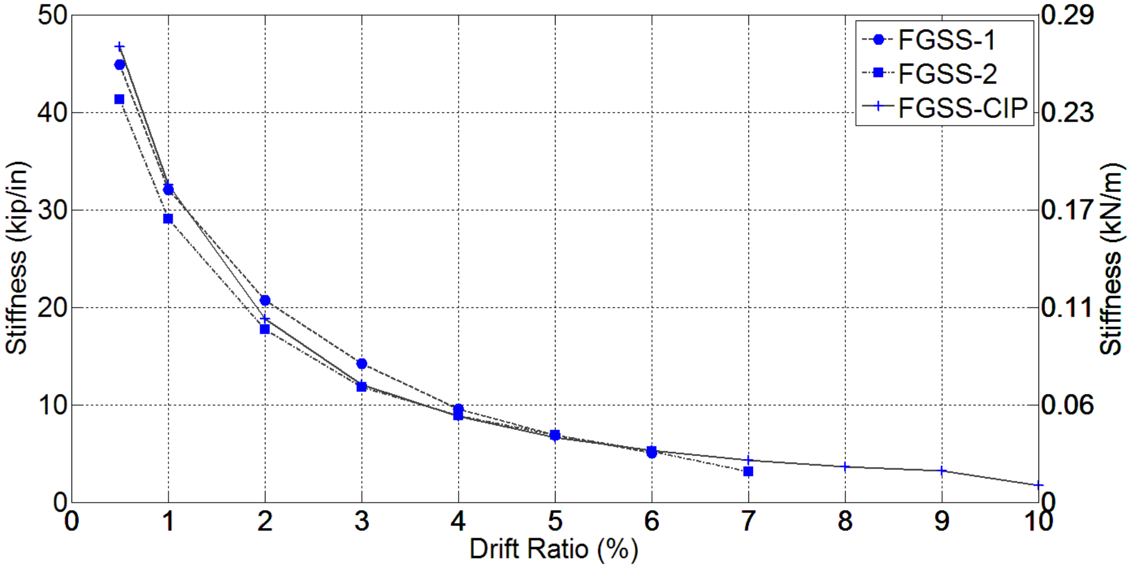

Figure 4.47 Stiffness degradation for column-to-cap beam test specimens.

4.3.4.3 Energy Dissipation Capacity

The cumulative hysteretic energy capacity for the column-to-cap beam specimens is shown in Figure 4.48. As observed, the rate of this quantity, which is directly associated with the area under the hysteretic loops, increases with an increase in the drift ratio up to failure for both test specimens. The specimens had a very similar hysteretic energy dissipation capacity up to a 3% drift ratio, after which specimen FGSS-CIP had a better performance. This implies that FGSS-2, which had the FGSS connectors inside the footing, had wider and more stable hysteresis loops that compared well with the cast-in-place specimen FGSS-CIP. Specimen FGSS-CIP had a superior hysteretic energy capacity and performed very well up to the 10% drift ratio. At a 6% drift ratio, the cumulative hysteretic energy was 1,021 in-kip, 1,405 in-kip, and 1,549 in-kip for specimens FGSS-1, FGSS-2, and FGSS-CIP, respectively; this is a 34% reduction in the overall hysteretic energy capacity when FGSS connectors are incorporated in the column base to connect the precast components.

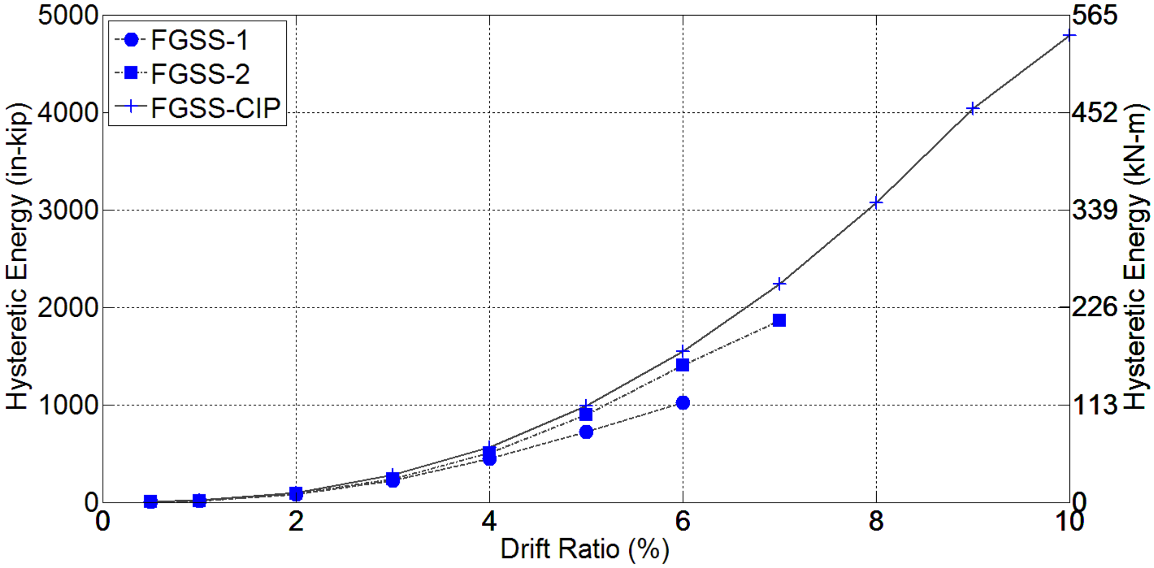

Figure 4.48 Cumulative hysteretic energy for column-to-cap beam specimens.

The equivalent viscous damping (ξ_{eq}) at each drift ratio was computed for each specimen in this category as described in Section 4.2.4.3. Figure 4.49 shows the ξ_{eq} variation for all test specimens. The increasing trend of ξ_{eq} is evident for the test alternatives, which implies a better hysteretic performance with an increase in drift ratio. Specimen FGSS-CIP had a ξ_{eq} of 35% at the 10% drift ratio, which is a desirable value for a ductile component. The equivalent viscous damping ratio at a 6% drift ratio was 14%, 22%, and 24 % for specimens FGSS-1, FGSS-2, and FGSS-CIP, respectively. This implies that a superior hysteretic response was achieved for specimens FGSS-2 and FGSS-CIP. Figure 4.49 shows that the hysteretic performance of the precast column-to-cap beam connection was affected adversely by incorporating the FGSS connectors inside the column base.

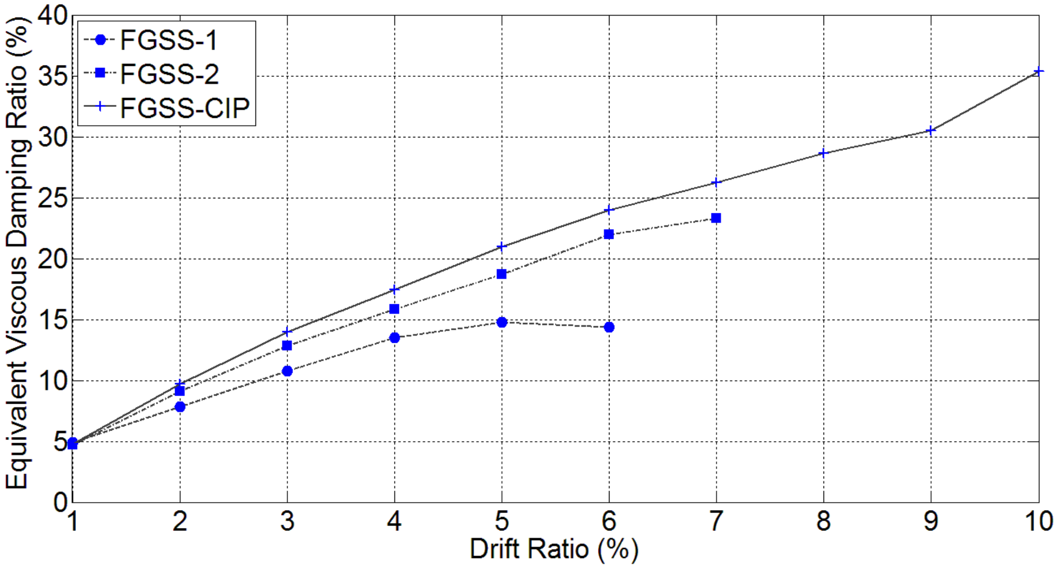

Figure 4.49 Equivalent viscous damping for column-to-cap beam specimens.

5. CONCLUSIONS

5.1 Summary

The grouted splice sleeve connector was studied for Accelerated Bridge Construction in high-seismic regions. There is limited information on the true performance of bridge joints using such connectors under simulated seismic loads, even though there have been some experimental research studies evaluating grouted splice sleeve connections in terms of strength properties or hysteretic performance. The research program described in this report was geared to ascertain the overall performance of two proprietary grouted splice sleeve connectors available to be implemented in actual bridge construction. This report has presented the design, construction, test procedure, and experimental results of two categories of splice sleeve connectors. Category-I specimens were half-scale models corresponding to column-to-footing joints, in which a grouted splice sleeve called GGSS was incorporated to splice the vertical reinforcing bars. Both dowel bars were grouted inside the GGSS connector when joining the precast column to the precast footing. Category-II specimens were half-scale models of column-to-cap beam joints, in which a grouted splice sleeve called FGSS was utilized to complete the joint. One rebar was fastened to the threaded end of this type of grouted splice sleeve, whereas the other rebar was grouted inside the opposite side of the sleeve.

Two precast specimens in addition to one conventional cast-in-place test model were constructed for each category of joints (column-to-footing and column-to-cap beam). The grouted splice sleeves were placed in the column base or column top in the first precast test alternative, with dowel bars protruding out from the footing or the cap beam. The connectors were placed in the footing or cap beam for the second test alternatives in both categories. The cast-in-place specimens were the control test models in which neither grouted splice sleeves nor even lap splices of the dowel bars were used; continuous bars protruding out from the footing and cap beam were used to build the columns.

The performance of all specimens was evaluated by analyzing the experimental results obtained from the instrumentation used to monitor the response under the quasi-static cyclic displacement history implemented in the tests.

Test results indicated that precast specimens had a similar performance to the control specimens in terms of strength properties; however, the hysteretic performance, ductility capacity, and failure modes were found to be different.

5.2 Findings

The experiments provided qualitative and quantitative measures for the performance of each individual specimen under quasi-static lateral cyclic loads. A summary of findings from the experimental data is presented separately for column-to-footing and column-to-cap beam joints.

5.2.1 Column-to-Footing Joints

1) Cast-in-place specimen GGSS-CIP had a desirable ductile performance, including a very good hysteretic response and ductile failure, i.e., rebar fracture on opposite sides of the column. This specimen had a displacement ductility of 8.9 and the hysteresis loops were wide and stable, implying a very good energy dissipation capacity.

2) Well-distributed flexural cracks formed along the column height of specimen GGSS-CIP, and the concrete cover spalled completely at the column base. The overall performance of specimen GGSS-CIP was dominated by flexural action and formation of a plastic hinge at the column base.
3) More localized damage was observed for the precast specimen with the GGSS connectors in the column base, i.e., GGSS-1. This involves fewer flexural cracks along the column height compared with the case of specimen GGSS-CIP. The spalled region was also smaller than that of specimen GGSS-CIP as a result of the presence of the GGSS connectors at the column base.
4) Specimen GGSS-2 had a damage state similar to that of specimen GGSS-CIP because there were no sleeves in the column base. Flexural cracks formed along the column, and the spalled regions in both specimens had a similar height, width, and depth.
5) Specimen GGSS-1 had a greater lateral force capacity than specimen GGSS-CIP. This was attributed to the GGSS connectors in the column base, which led to a transition of the flexural action to the section right above the GGSS region. In addition, the cast-iron sleeves located in the column base of specimen GGSS-1 provided a compression reaction component at the interface, which was believed to contribute to a higher lateral force capacity.
6) Rebar fracture occurred in the column-to-footing test specimens, which indicated that the tensile strength of the bars was developed when GGSS connectors were utilized. Fracture of reinforcing bars in specimen GGSS-CIP was due to low cycle fatigue. For precast specimens GGSS-1 and GGSS-2, rebar fracture occurred earlier than for specimen GGSS-CIP. This implies that premature rebar fracture was present for all precast test specimens, which was due to higher strains concentrated in the rebar at the interface of the column and footing.
7) A displacement ductility of 6.1 was achieved for specimen GGSS-2 in which the GGSS connectors were inside the footing. Compared with specimen GGSS-1 with a displacement ductility of 5.4, a more ductile response was obtained by placing the GGSS connectors in the footing. Compared with the case of control specimen GGSS-CIP with a displacement ductility of 8.9, a less ductile performance was obtained when GGSS connectors were used to connect the precast components.
8) The distribution of inelasticity in the column base of specimen GGSS-2 was very similar to specimen GGSS-CIP, as there was no disruption of the natural stress transfer in the column base of GGSS-2. For the case of specimen GGSS-1, however, a different distribution of inelasticity was observed. This was attributed to the presence of the GGSS connectors in the column base in which the inelastic actions were shifted to locations at the bottom and top of the GGSS connectors.
9) Strain gauge data revealed that both factory and field dowel bars developed the yield strength of the rebar for specimen GGSS-1; however, the bottom dowel bar (factory dowel) did not yield for the case of specimen GGSS-2.
10) The displacement ductility obtained for all test alternatives exceeded the minimum component displacement ductility of 3.0 specified in the Caltrans SDC. In addition, the displacement ductility values were greater than the maximum displacement ductility of 5.0, which was specified in the AASHTO Seismic Guide for single-column bridge bents.

5.2.2 Column-to-Cap Beam Joints

1) Cast-in-place specimen FGSS-CIP had a desirable ductile performance, including a very good hysteretic response and a ductile failure, i.e., rebar fracture on opposite sides of the column; a displacement ductility of 9.9 was achieved and the hysteresis loops were wide and stable, implying a good energy dissipation capacity.
2) Well-distributed flexural cracks formed along the column height of specimen FGSS-CIP, and the concrete cover spalled completely at the column base. The overall performance of specimen FGSS-CIP was dominated by flexural action and formation of a plastic hinge at the column base.
3) More localized damage was observed for precast specimen FGSS-1 with the FGSS connectors in the column base. This involved fewer flexural cracks along the column height compared with the case of specimen FGSS-CIP. The spalled region was also smaller than that of specimen FGSS-CIP as a result of the FGSS connectors being in the column.
4) Specimen FGSS-2 had a damage state similar to the cast-in-place specimen FGSS-CIP because there were no sleeves in the column. Hence, more flexural cracks formed along the column, and the spalled regions in both specimens had a similar height, width, and depth.
5) Specimen FGSS-1 had a greater lateral force capacity than specimen FGSS-CIP. This was attributed to the presence of FGSS connectors in the column, which led to a transition of the flexural action to the section right above the FGSS region. In addition, the cast-iron sleeves located in the column of specimen FGSS-1 provided a compression reaction component at the interface, which was believed to contribute to a higher lateral force capacity.
6) Rebar fracture occurred in the cast-in-place specimen FGSS-CIP at a 10% drift ratio due to low cycle fatigue. For specimen FGSS-2, the west column rebar fractured prematurely at a 7% drift ratio, while the east column bar underwent excessive slippage and pullout. Specimen FGSS-1 failed prematurely because of rebar pullout due to an excessive bond-slip.
7) A displacement ductility of 5.8 was achieved for specimen FGSS-2, in which the FGSS connectors were inside the cap beam. Compared with the case of specimen FGSS-1 with a displacement ductility of 4.9, a more ductile response was obtained by placing the FGSS connectors in the cap beam, along with a better hysteretic performance.
8) The distribution of inelasticity at the column end for specimen FGSS-2 was very similar to specimen FGSS-CIP, as there was no disruption of the natural stress transfer in the column end of FGSS-2. For specimen FGSS-1, however, a different distribution of inelasticity was observed. This was attributed to the presence of the FGSS connectors in the column end, in which the inelastic action was shifted to locations at the bottom and top of the FGSS connectors.
9) Strain gauge data revealed that both factory and field dowel bars developed the yield strength of the rebar for specimen FGSS-1; however, the bottom dowel bar (factory dowel) did not yield for the case of specimen FGSS-2.
10) The displacement ductility obtained for all specimens exceeded the minimum component displacement ductility of 3.0 specified in the Caltrans SDC. In addition, the displacement ductility obtained for specimen FGSS-2 was greater than the maximum displacement ductility of 5.0, which was specified in the AASHTO Seismic Guide for single-column bridge bents.

6. REFERENCES

[1] M. Tazarv and M. Saiidi, "Emulative Moment-Resistant RC Bridge Column-Footing Connection for Accelerated Bridge Construction in High Seismic Zone," in Seventh National Seismic Conference on Bridges & Highways, Oakland, 2013.

[2] J. I. Restrepo, M. J. Tobolsky, and E. E. Matsumoto, "Development of a Precast Bent Cap System for Seismic Regions," NCHRP Report 681, Washington, D.C., 2011.

[3] M. L. Marsh, M. Wernly, B. E. Garett, J. F. Stanton, M. O. Eberhard, and M. D. Weinert, "Application of Accelerated Bridge Construction Connections in Moderate-to-High Seismic Regions," NCHRP Report 698, Washington, D.C., 2011.

[4] B. Khaleghi, E. Schultz, S. Seguirant, L. Marsh, O. Haraldsson, M. Eberhard, and J. Stanton, "Accelerated bridge construction in Washington State: From research to practice," *PCI Journal*, vol. 57, no. 4, 2012.

[5] O. Haraldsson, M. J. Schoettler, G. Finnsson, P. M. Davis, J. Stanton, and M. Eberhard, "Seismic Resistance of Precast Concrete Bridge Columns Made with Unbonded Pre-Tensioning and Hybrid Fiber Reinforced Concrete," Seventh National Seismic Conference on Bridges & Highways, Oakland, CA, 2013.

[6] M. Tazarv and M. S. Saiidi, "UNR-Caltrans Research Projects," UNR-Caltrans, 2014. [Online]. Available: http://wolfweb.unr.edu/homepage/saiidi/caltrans/NextGen/PDFs/HCSPreliminaryResults2-14.pdf.

[7] Z. B. Haber, M. S. Saiidi, and D. H. Sanders, "Seismic Performance of Precast Columns with Mechanically Spliced Column-Footing Connections," *ACI Structural Journal*, vol. 111, no. 3, 2014.

[8] Z. B. Haber, M. S. Saiidi, and D. H. Sanders, "PRECAST COLUMN-FOOTING CONNECTIONS FOR ACCELERATED BRIDGE CONSTRUCTION IN SEISMIC ZONES," Center for Civil Engineering Earthquake Research, Department of Civil and Environmental Engineering, University of Nevada, Reno, Reno, 2013.

[9] P. O. Jansson, "Evaluation of Grout-Filled Mechanical Splices for Precast Concrete Construction," Michigan Department of Transportation, Lansing, MI, 2008.

[10] American Association of State Highway and Transportation Officials (AASHTO), "AASHTO LRFD Bridge Design Specifications," Washington, D.C., 2012.

[11] ACI-ASCE Committee 550, Guide to Emulating Cast-in-Place Detailing for Seismic Design of Precast Concrete Structures, Farmington Hills, MI: American Concrete Institute, 2009, p. 17.

[12] H. Aida, Y. Tanimura, T. Tadokoro, and K. Takimoto, "Cyclic Loading Experiment of Precast Columns of Railway Rigid-Frame Viaduct Installed with NMB Splice Sleeves," in Proceedings of the Japan Concrete Institute, 2005.

[13] T. Yoshino, K. Kobayashi, and M. Ase, "Intensive Shear Reinforcing Method for PCA Members with Splice Sleeve Joint," Eleventh World Conference on Earthquake Engineering, Acapulco, Mexico, 1996.

[14] Splice Sleeve Japan, LTD, "Tests on Re-Bar Splices in Reinforced Concrete Columns Using NMB Splice Sleeves," NPD-024.

[15] Y. Matsuzaki and et al., "Effects of Sleeves on Member Properties, Study on the Behavior of Reinforced Concrete Beams with Grout-Filled Steel Splice Sleeves," Architectural Institute of Japan, 1987.

[16] American Association of State Highway and Transportation Officials (AASHTO), AASHTO Guide Specifications for LRFD Seismic Bridge Design, Washington D.C.: AASHTO, 2011.

[17] California Department of Transportation, Seismic Design Criteria, CA: Division of Engineering Services, 2010.

[18] ASTM Standard C39, Standard Test Method for Compressive Strength of Cylindrical Concrete Specimens, West Conshohocken, PA: ASTM International, 2012.

[19] ASTM Standard C109, Standard Test Method for Compressive Strength of Hydraulic Cement Mortars (Using 2-in. or [50-mm] Cube Specimens), West Conshohocken, PA: ASTM International, 2012.

[20] ACI Committee 374, Guide for Testing Reinforced Concrete Structural Elements Under Slowly Applied Simulated Seismic Loads, Farmington Hills, MI: American Concrete Institute, 2013.

[21] R. Park, "Evaluation of Ductility of Structures and Structural Assemblages from Laboratory Testing," *Bulletin of the New Zealand National Society for Earthquake Engineering*, vol. 22, no. 3, pp. 155-166, 1989.

[22] M. Priestley and R. Park, "Strength and Ductility of Concrete Bridge Columns Under Seismic Loading," *ACI Structural Journal*, vol. 84, no. 1, pp. 61-76, 1987.

[23] California Department of Transportation, Seismic Design Criteria, CA: Division of Engineering Services, 2010.

[24] A. K. Chopra, Dynamics of Structures, Theory and Applications to Earthquake Engineering, NJ: Pearson Prentice Hall, 2007.